AN ABSTRACT OF THE DISSERTATION OF

Kevin L. Rogers for the degree of Doctor of Philosophy in Medical Physics presented on May 16, 2017.

Title: Accounting for Heterogeneity Corrections in Breast Brachytherapy

Abstract approved:

Camille J Palmer   Kathryn A Higley

Purpose: Model-based dose calculation algorithms (MBDCAs) have become clinically available within the past several years in commercially available brachytherapy planning systems. This work investigates the application of a 510(k) approved MBDCA Acuros™ BV and establishes a reproducible method of validation. The research is broken into three primary research goals. The first objective was to focus on helping medical physicists reproducibly validate the implementation of MBDCA in the clinic by using direct measurements and comparison to Monte Carlo (MC). The second objective was to commission a very low energy spectrum using Attila™, the parent software to Acuros™ BV, by comparison to MC. The third area retrospectively examines the application of Acuros™ BV to a large group of previously treated patients by accelerated partial breast irradiation brachytherapy.

Methods: A Quality Assurance phantom (QAP) was fabricated by taking a solid ($30x30x5\ cm^3$) piece of water and drilling a 3 cm diameter hole to accommodate a variety of pre-manufactured density plugs. The phantom was used to validate the clinical implementation of the commercially available MBDC algorithm Acuros™

BV. Once the QAP was imported into BrachyVision, the Acuros^{TM} BV ^{192}Ir dose distributions were calculated. The QAP was modeled using Monte Carlo N-Particle version 5 (MCNP5) and dose predictions were compared to Acuros^{TM} BV at 0.2 cm increments out to 4.5 cm. Additionally, physical measurements taken using Diode and a MOSFET were also compared to Acuros^{TM} BV. The second part of the investigation used a similar QAP simulated three dimensionally in Attila™. This investigation replaced the ^{192}Ir source with a 50 kVp source spectrum provided by Xoft, Inc. Attila™ and MCNP5 were used to simulate this low energy spectrum as the source in the QAP at multiple points for comparison. The final investigation examined two hundred accelerated partial breast irradiated (APBI) brachytherapy patients that had been treated from 2008 to 2012 by the original TG43 formalism and recalculated using Acuros^{TM} BV. Clinically relevant endpoints such as V100, V90, erythema and moist desquamation were compared between TG43 and Acuros™ BV. Results: Over twenty points extending through different heterogeneities were compared using an ^{192}Ir source and calculated for both Acuros^{TM} BV and MCNP. Physical measurements taken on the QAP using solid-state detectors compared within 1% of Acuros™ BV calculations. The absolute dose of Acuros^{TM} BV compared with MC results varied from -3.0% up to 7.2%. When investigating the impact of heterogeneities from a low kV spectrum, the absolute difference from Attila™ and MC ranged from -15.1% to 9.0%. The final retrospective study showed noticeable changes in recalculated dosimetry, with the most significant changes observed with balloon devices. The difference in dose when Acuros^{TM} BV was subtracted from TG43 calculations showed balloons have reduced skin doses that ranged from 0.4%

to 10.2%. The differences for SAVI™ showed skin dose changes from -9.5% to 7.8%. For balloon devices, the average dose differences for V100, V95, V90 were 5.6%, 4.9% and 3.8%, respectively. The SAVI™ dose differences for V100, V95, V90 were 2.2%, 2.1%, and 1.8%, respectively.

Conclusions: A phantom was fabricated to serve as a tool for clinical medical physicists to efficiently and reproducibly validate the commissioning of MBDCAs. This QAP aids in a fully inclusive system check from CT acquisition, to Acuros™ BV calculations and finally diode or MOSFET measurements. Commissioning for very low energy spectrum, such as eBx, was accomplished by importing this phantom into Attila™ and comparing to MCNP calculations when encountering heterogeneities. The final retrospective study suggest further investigation is needed to assign uniform densities to heterogeneities encountered in the patient's CT images. The recalculated patient dose using Acuros™ BV did predict a reduction in dose at key points, such as tissue-air interface, V100 and V90 coverage, however, acute and chronic skin dose thresholds showed no trending in data and were not predictable.

Accounting for Heterogeneity Corrections in Breast Brachytherapy

by
Kevin L. Rogers

A DISSERTATION

submitted to

Oregon State University

in partial fulfillment of
the requirements for the
degree of

Doctor of Philosophy

Presented May 16, 2017
Commencement June 2017

Doctor of Philosophy dissertation of Kevin L. Rogers presented on May 16, 2017

APPROVED:

Major Professor, representing Medical Physics

Head of the School of Nuclear Science and Engineering

Dean of the Graduate School

I understand that my dissertation will become part of the permanent collection of Oregon State University libraries. My signature below authorizes release of my dissertation to any reader upon request.

Kevin L. Rogers, Author

ACKNOWLEDGEMENTS

I would like to express my sincere appreciation to Dr. Camille J. Palmer, whose help, guidance, and support over great distances was invaluable.

I want to thank Dr. Kathryn A. Higley for giving me a chance many years ago to pursue this degree and her encouragement along the way.

Thank you to my committee for taking time out of your busy schedule.

Dr. Todd Palmer

Dr. Wolfram Laub

Dr. Haori Yang

Dr. Henri Jansen

Thank you to the team at Transpire, Inc.

Dr. Todd Wareing for his time and insight.

Mr. Ian Davis

Mr. Gregory Failla

Thank you to Varian Medical Systems, Inc. for allowing me the chance to investigate part of your software.

A special thanks to my wife Laura Rogers, for her support, encouragement, patience, friendship and keeping the boys occupied while I studied.

TABLE OF CONTENTS

Page

1. Introduction 1
  - 1.1. Research Objectives 4

2. Background and Literature Review 7
  - 2.1. APBI Brachytherapy Device Heterogeneity 7
    - 2.1.1. ^{192}Ir 7
    - 2.1.2. eBx 16
  - 2.2. TG-43 Overview 20
  - 2.3. MCNP5 23
  - 2.4. Attila™ 24
  - 2.5. Acuros™ BV 25
  - 2.6. MOSFETS and Diodes 26
  - 2.7. Reasons to Adopt MBDCAs 27

3. Materials and Methods 30
  - 3.1. Acuros^{TM} BV Validation for ^{192}Ir 30
    - 3.1.1. CT Electron Density Phantom and HU Calibration 30
    - 3.1.2. Design of the QA Phantom (QAP) and Importing 35
    - 3.1.3. Application of Acuros^{TM} BV 41
    - 3.1.4. In-Vitro Validation Measurements of ^{192}Ir 43
    - 3.1.5. MC ^{192}Ir Scenario 48
  - 3.2. Attila® Validation using a Low kV Spectrum 52
    - 3.2.1. Attila 52
    - 3.2.2. MC Modeling of Xoft® Spectrum 57
  - 3.3. Patient Review with Acuros^{TM} BV 58
    - 3.3.1. Patient Parameters 58
    - 3.3.2. Patient Data Preparation 61
    - 3.3.3. Patient Data Collection 62

4. Results and Discussions 63
  - 4.1. Measurements using ^{192}Ir 63
    - 4.1.1. Diode and Mosfet measurements 63
    - 4.1.2. Acuros^{TM} BV and MC comparison using ^{192}Ir 64

TABLE OF CONTENTS (Continued)

4.2. Low kV Analysis with Attila and MC 82
4.3. Patients with Acuros™ BV 97

5. Conclusions 105

5.1. Physical Measurements 105
5.2. Acuros^{TM} BV vs. MC 105
5.3. Attila® vs. MC 106
5.4. Application of Acuros on Actual Patients 107

6. Bibliography 110

Appendix A: 192Ir MCNP Input Deck 114

Appendix B: MCNP Xoft Spectrum Input Deck File 119

Appendix C: Two Hundred Patient Data 122

LIST OF FIGURES

Figure Page

Figure 1. Original MammoSite® device showing a single lumen. Courtesy of HOLOGIC, Inc and affiliates. 9

Figure 2. Bard SenoRx Contura showing 5 lumens. Courtesy of HOLOGIC, Inc and affiliates. 10

Figure 3. SAVI designs showing 7 to 11 lumens. Courtesy of Cianna Medical, Inc. 12

Figure 4. CT axial scan showing contrast inserted inside balloon for visualization. Courtesy of HOLOGIC, Inc. and affiliates. 14

Figure 5. Axial scan of a SAVI in-vitro showing half-filled cavity of seroma fluid. Permission from Arizona Center for Cancer Care, LLC. 15

Figure 6. The Xoft Axxent Balloon applicator used exclusively with Xoft Axxent X-ray source. Courtesy of XOFT, a subsidiary of iCAD, Inc. 17

Figure 7. Xoft Axxent Xray source. Courtesy of XOFT, a subsidiary of iCAD, Inc. 17

Figure 8. CT Electron Density Phantom 32

Figure 9. CT Electron Density Phantom scan for Hounsfield Unit confirmation. 33

Figure 10. Solid water phantom 30x30x5 cm^3 37

Figure 11. Examples of air, lung and cortical bone plugs. 38

Figure 12. BrachyVision display of the 192Ir source wire. 39

Figure 13. BrachyVision display of Calculation Point 40

Figure 14. GammaMedplus™ iX Remote Afterloader 44

Figure 15. Best CNMC Equidose II Diode Detectors 45

Figure 16 MOSFET model TN-502RD (Best Medical Ontario, Canada) 46

Figure 17. Picture of the QAP physical measurements showing the position of the MOSFET. 47

Figure 18. MCNP Visual Editor's GammaMedplus source modeled. 49

Figure 19. MCNP QAP design with calculation points. 50

LIST OF FIGURES (Continued)

Figure 20. Solidworks Study Phantom 53

Figure 21. Attila Mesh applied to study phantom... 54

Figure 22. 50kV, Xoft Spectrum Courtesy of XOFT, a subsidiary of iCAD, Inc. 56

Figure 23. 50 kV reduced Xoft Spectrum for MCNP and Attila 56

Figure 24. Acuros™ BV and MCNP5 water plug comparison with ^{192}Ir on QAP. ... 72

Figure 25. Acuros™ BV and MCNP5 cortical bone plug comparison with ^{192}Ir....... 73

Figure 26. Mass-Absorption Coefficients Normalized to Water 75

Figure 27. Acuros™ BV and MCNP5 air plug comparison with 192Ir. 76

Figure 28. Acuros™ BV and MCNP5 Lung plug comparison with 192Ir 78

Figure 29. Acuros™ BV and MCNP5 absolute differences with 192Ir. 79

Figure 30. Attila and MCNP5 water plug comparison with low kV spectrum........... 86

Figure 31. Attila and MCNP5 bone plug comparison with low kV spectrum............ 88

Figure 32. Soft X-ray buildup at tissue-bone interface calculated by MC Visual Editor.. 89

Figure 33. Attila and MCNP5 air plug comparison with low kV spectrum. 91

Figure 34. Attila and MCN5 lung plug comparison with low kV spectrum............... 93

Figure 35. Attila and MC Percent Differences with low kV spectrum....................... 96

LIST OF TABLES

Table | Page

Table 1. Hounsfield Unit comparison CT to Varian BrachyVision........................... 34

Table 2. Material Mass Densities from Varian BrachyVision Recreated.................. 42

Table 3. Toxicity Criteria of the Radiation Therapy Oncology Group (RTOG) and the European Organization for Research and Treatment of Cancer (EORTC) 60

Table 4. Diode and Mosfet Measurements. 63

Table 5. Comparison of F6, *F8, Acuros and TG43 for ^{192}Ir On Semi-Infinite Phantom 66

Table 6. MC Comparison of Finite and Infinite Phantom for ^{192}Ir............................ 69

Table 7. Material Compositions.. 70

Table 8. Comparison of Finite and Semi-Infinite Phantom for Low kV Energy 84

Table 9. Contura and MammoSite Patients Acuros vs. TG43................................. 100

Table 10. SAVI Patients Acuros vs. TG43 100

Table 11. Two hundred patient results overview.. 103

Table 12. Acute Skin Reactions are tabulated with TG43 and Acuros™ BV maximum skin dose.. 103

Table 13. Chronic Skin Reactions are tabulated with TG43 and Acuros™ BV maximum skin dose. 104

Accounting for Heterogeneity Corrections in Breast Brachytherapy

1. Introduction

Whole breast irradiation (WBI) with negative margin lumpectomy surgery, also called breast conserving therapy (BCT), has become an accepted alternative to radical mastectomy for some early stage cancers for the last thirty years (Veronesi, et al., 2002). A drawback to the BCT is the number of treatment days which can range from five to seven weeks. This lengthy treatment schedule can cause a hardship for patients that travel extended distances or have difficulty with acquiring transportation. Over the last twenty-five years, physicians have pursued reduced treatment prescriptions for certain qualified staged breast cancers. These reduced fraction, or hypo-fractionated treatments, are referred to as accelerated partial breast irradiation (APBI) and have been gaining favor over the lengthy WBI. Recent research of long term clinical survival shows APBI to be equivalent to WBI for certain stage breast cancers (Shah, et al., 2013). (Skowronek, et al., 2012)

The most recent randomized study, that opened in March 2005 by the National Surgical Adjuvant Breast and Bowel Project (NSABP) was NSABP B-39, A Randomized Phase III Study of Conventional Whole Breast Irradiation Versus Partial Breast Irradiation (PBI) for Women with Stage 0, I or II Breast Cancer. B-39 was designed to evaluate whether APBI gave overall equivalent success in local tumor control rate compared to WBI. By 2017, long term analysis demonstrated that APBI did indeed offer outcomes similar to WBI for long term local tumor control as shown by (Correa, et al., 2017).

The B-39 APBI brachytherapy techniques described in 2005 consisted of either the multi-catheter insertions or the use of a single-entry intra-cavitary brachytherapy devices called, MammoSite®. Many companies created and began marketing single-entry brachytherapy devices soon after the B-39 began accruing patients, which was appealing to patients preferring to have this hypo-fractionated radiation treatment that APBI offered. The new devices were called MammoSite® ML, Contura™ MLB, and SAVI®. Each of these devices added to the complexity of the brachytherapy planning process by introducing more variations in the placement of the HDR source as well as introducing their own heterogeneities.

Accurate dose representation is vital for physicians when deciding the appropriate patient treatment plan, whether using external beam WBI or brachytherapy APBI. External beam WBI has enjoyed several advances in the accuracy of the dose calculations. Starting in the late 1980s, dose distributions were little more than pre-calculated isodose drawings that were superimposed onto a hand drawn contour of the patient. The machine beam time was then estimated by using lookup tables that had been created from water based measurements, such as Clarkson Sector Integration (Pla, et al., 1988). This Clarkson Sector Integration was applied to a two-dimensional aperture drawing. The external beam data used for the treatment time assumed that the patient was represented as a square box of water. In the early 1990s, external beam calculations moved from 2D single plane image to a pseudo 3D that utilized stacked CT slices along with the Pencil Beam algorithm that applies corrections for curvature and some in-plane heterogeneity. The pseudo 3D dose calculations lack information from lateral scatter thus the predicted dose is not truly three dimensional.

As recently as early 2000s, 3D external beam calculations that account for heterogeneities in plane as well as lateral scatter were introduced in WBI using model based dose calculation algorithms (MBDCA), such as the Analytical Anisotropic Algorithm, Collapsed-Cone Algorithm, and Grid Based Boltzmann Solvers (GBBS). These represent only a few that are FDA 510(k) approved to use clinically. The section 510(k) of the FDA requires a manufacturer to register their new medical device ninety days prior to marketing as a Premarket Notification. This allows the FDA to classify the new device and authorize the device is safe to market in the United States. Since the introduction of the MBDCAs the medical physics community, aided by American Association of Physicists in Medicine (AAPM), has been cautious when adopting new algorithms. Focused task groups created by AAPM set forth guidelines and recommendations to the medical physics community describing appropriate methods for commissioning new external beam MBDCAs.

Unlike external beam, brachytherapy dose calculations have evolved more slowly into acceptance. Prior to 1995, brachytherapy calculations were based upon the Paterson Parker method of dose distributions. Due to an increase in vendors providing high-dose rate (HDR) remote afterloading brachytherapy devices as well as low-dose (LDR) rate radioactive seeds, the AAPM formed a task group to establish a formalism for brachytherapy dose calculations.

The AAPM Task Group assigned to modifying the brachytherapy dose formalism was Task Group 43, or TG43 (Nath, et al., 1995). The TG43 formalism attempted to more accurately model each available HDR and LDR radioactive seeds available on the market by designating acceptable methods for manufacturers to characterize the seed, while accounting for shielding and anisotropy of the source. The TG43 data was collected either by TLD measurements in water or generated by Monte Carlo (MC) simulations in a homogeneous water phantom. The treatment planning systems (TPS) incorporated TG43 by seed superposition. Where the orientation of the seeds was known, a 2D model of dose could be utilized, when the orientation was unknown the TPS would use a point source model. The dose distributions displayed for the physician were calculated using either polynomial equations or a long-and-away table. TG43 formalism was never designed to accommodate mass-energy absorption coefficients, therefore all patient or treatment device heterogeneities are ignored. As of 1995, TG43 became the standard of practice for brachytherapy calculations and has remained the primary formalism for calculations even into 2017.

On July 21, 2009, Varian Medical Systems received 510(k) approval for Acuros™ BV (Varian Medical Systems, Palo Alto, CA), Varian's trademarked MBDCA that is a modification of Attila™ (Transpire, Inc.) specifically for ^{192}Ir. Acuros™ BV is a GBBS that offers the ability to accommodate specific voxel material attributes necessary to accurately simulate photon transport in a heterogeneous medium for brachytherapy treatment planning.

1.1. Research Objectives

The inspiration for this research is to better characterize the impact and significance when the improved tools, such as Acuros BV, are implemented in the clinic. It is imperative that the treatment planning tools are commissioned in a reliable and reproducible manner, and that physicists fully understand the impact of dose calculations to the patient. This work addresses the clinical implementation of a grid based Boltzmann Solver (GBBS) when used as the treatment planning algorithm for accelerated partial breast irradiation (APBI), and seeks to quantify the dose variation due to tissue inhomogeneity for both ^{192}Ir source and low kV Xoft Axxent spectrum.

This work has three primary research objectives, outlined below.

Objective 1: The first objective is to design, fabricate, and test a reproducible phantom that can be used to validate the commissioning of MBDCAs while correctly accounting for heterogeneities using an ^{192}Ir. A design requirement of the phantom is that it is CT compatible and able to accommodate plugs of various material densities representative in the brachytherapy treatment planning. The phantom was then utilized to investigate the Acuros MBDCA. Specific tasks are outlined in Specific Aims 1.1 and 1.2.

Specific Aim 1.1: Design and fabricate a reproducible phantom that is specifically designed to accommodate the insertion of different physical materials into exact placements.

Specific Aim 1.2: Simulate the phantom utilizing ^{192}Ir as a source in MCNP, which can then be used as the gold standard to assess the MBDCA's ability to accurately account for variation in dose due to the phantom’s heterogeneities.

Objective 2: The second objective is to utilize Attila (parent software to Acuros), to investigate the heterogeneities predicted using a commercially low kV spectrum in the phantom fabricated in the first research objective. This investigation expands Attila to incorporate low energy photoelectric cross sections when calculating dose using the Xoft Accent device.

Specific Aim 2.1: Simulate the 3D phantom in Attila and incorporate low kVp cross sections into the Attila software.

Specific Aim 2.2: Modify a commercially low kVp spectrum as a source term for Attila and MCNP file for comparison of dose predictions at material interfaces.

Objective 3: The third objective is to perform a retrospective clinical investigation using Acuros to determine the clinical impact of improved treatment plans. This involves recalculating previously treated accelerated partial breast HDR patients. The results of clinically relevant dose volumes and maximal dose points will be compared between TG43 and Acuros, which now accounts for patient-specific heterogeneities.

Specific Aim 3.1: Select two hundred previously treated APBI HDR patients that were calculated using TG43 and recalculate patient dose using Acuros. Tabulate and compare the changes to maximum skin dose, maximum rib dose, V90 and V100 indices that are recommended by the American Brachytherapy Society.

Specific Aim 3.2: Review the medical records of the 200 patients and tabulate both acute and chronic skin reactions. Compare the severity of skin reactions to the Acuros associated skin doses and determine if any relevant skin dose tolerances are indicated.

2. Background and Literature Review

2.1. APBI Brachytherapy Device Heterogeneity

2.1.1. ^{192}Ir

In the late 1980s, the technique to introduce the ^{192}Ir high-dose-rate (HDR) remote afterloader brachytherapy source into the patient was accomplished via surgically implanted nylon hollow tubes. These nylon tubes have a four-millimeter internal diameter, which was large enough to accommodate most manufactured ^{192}Ir HDR sources available from FDA approved vendors. The surgical method to insert these tubes is complex and takes a team effort of physician, physicist, therapist and nurse.

The patient lumpectomy cavity is first visualized with contrast-air injected into the cavity via a needle. A template is used to allow the physician to produce adequate spacing between the needles when encompassing the lumpectomy cavity plus a safe margin of extra tissue. This surgical procedure takes approximately two to three hours of the physician and staff's time. Next an axial computed tomography (CT) scan is acquired of the patient with catheters in place and the resultant images are imported into the treatment planning computer. Each tube is delineated as a pathway for the planning system to calculate possible dwell times of the ^{192}Ir source. A physician now draws a clinical target volume (CTV) that is the lumpectomy cavity. The physicist then expands this CTV to create the planning target volume (PTV) which is the CTV plus 1.5 cm margin. This method of treating APBI with nylon multi-catheter implantation does not introduce any heterogeneities into the planned area. Therefore, the original dose calculations using TG43 and source superposition give reasonably accurate dose representation, except next to natural heterogeneities such as bone, air and lung interfaces (Keisch, et al., 2007).

In the early 2000s, due to increased demand for shorter treatment times offered by APBI, newer devices for treating APBI with ^{192}Ir HDR came to market. These new single-entry devices were designed to minimize implantation time to less than a half hour and only require a physician and nurse during the procedure. Unlike the multi-catheter nylon tubes, each new device had its own intrinsic heterogeneities for which the TG43 formalism does not account for in the dose calculations.

In 2003, the first alternative device known as MammoSite® (Hologic Inc., Bedford, MA) was FDA 510(k) approved for treating the remaining lumpectomy cavity in early stage breast cancer (shown in Figure 1). The applicator design is straightforward in that it uses only one central lumen for the HDR treatment. Another unique aspect of this device is that the single lumen is surrounded by a balloon that may be inflated with sterile water. Insertion of the MammoSite® was made possible by the physician creating a path from outer skin into the lumpectomy cavity visualized by ultrasound and using a sharp trocar. Upon inflation, the MammoSite® balloon conformally shapes the surrounding tissue spherically while the single lumen remains centered. The simplicity of the MammoSite® allowed doctors to quickly insert a lumen into the lumpectomy cavity immediately after surgery. With this improved efficiency, more patients began to prefer this method of APBI treatment. One dosimetric limitation when using the MammoSite® is the single lumen causes all HDR dwell locations to be centered within the balloon. Under certain treatment conditions, and at appropriate skin distances, this design was adequate since the ^{192}Ir source irradiated tissue surrounding the balloon with radial symmetry from the dwell source. For the MammoSite® treatments, the PTV is defined as all surrounding tissue within one centimeter from balloon edge. However, if the skin-balloon distance was smaller than the PTV, the skin became exposed to excessive high dose due to the steep fall-off gradient of the ^{192}Ir. American Brachytherapy Society Breast Brachytherapy Task Group published a consensus report recommending prescriptive dosimetric parameters for breast brachytherapy using APBI technique. For the balloon devices, the maximum suggested skin dose should be < 145% of prescribed dose which effectively translates into a minimum balloon to skin distance of 7 mm to meet the recommended skin tolerance (Keisch, et al., 2007).

Figure 1. Original MammoSite® device showing a single lumen. Courtesy of HOLOGIC, Inc and affiliates.

The next device to market was the SenoRx Contura MLB (Hologic, Bedford, MA) as shown in Figure 2. This device is inserted similar fashion as the MammoSite®. The Contura differs from the MammoSite® as it has four additional lumens and two vacuum holes placed at both the proximal and distal ends of the balloon. These four additional lumens surround the central lumen have maximum curvature 5 mm from the center. The curvature of the lumens increases the flexibility to create dose distributions that can be shaped, or contoured, along the skin edge. The Contura is less restrictive to patients, allowing a greater portion to proceed with treatment by preferentially pulling the dose away from the dermis while not compromising the target volume.

Figure 2. Bard SenoRx Contura showing 5 lumens. Courtesy of HOLOGIC, Inc and affiliates.

A third single-entry HDR device is the Strut-Adjusted Volumetric Implant, or SAVI® (Cianna Medical, Aliso Viego, CA) multi-lumen device shown in Figure 3. The SAVI® has no balloon and offers four different lengths to accommodate longer lumpectomy cavities. The SAVI® varies from having six lumens up to nine that surround a central lumen. With the absence of a balloon to center the device inside the cavity, the SAVI® is able to fill the remaining lumpectomy cavity by expanding the device into the shape of a sphere. For insertion, the lumens are collapsed against the central tube to allow a physician to introduce the SAVI® into the lumpectomy cavity via a 1 cm diameter hole. Then a key is slid into the SAVI® that is rotated to cause the central lumen to turn like a cork-screw. This cork screw action bends the outer lumens into a more spherical shape as seen in Figure 3. The lumens retain this shape from the support of metal bands that travel the length of each lumen from the distal tip along the lumen to a proximal anchor band.

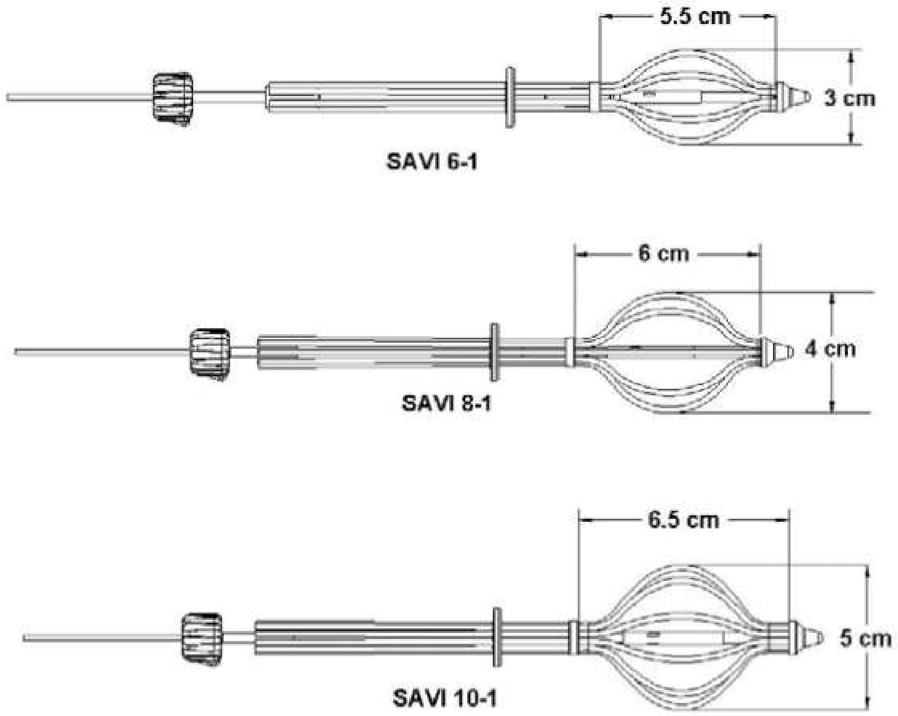

Figure 3. SAVI designs showing 7 to 11 lumens. Courtesy of Cianna Medical, Inc.

The heterogeneities that are encountered during the planning process and the lack of the TG43 formalism accounting for their dose perturbations have been examined over the last twelve years. The impact of heterogeneities in brachytherapy APBI have primarily focused on the following: radiographic-opaque contrast placed in the medium of the balloons, air pockets that exist adjacent to and within the balloons, air pockets that exist within the SAVI after seroma fluids have leaked, boundary conditions such as breast-bone, breast-lung, and breast-skin edge.

The MammoSite and the Contura balloons must have non-ionic radiopaque contrast solution, such as Optiray™ 320 (Mallinckrodt Pharmaceuticals, St. Louis MO), introduced into the saline solution that expands the balloon for visualization during CT scans as shown in Figure 4. Each milliliter of Optiray™ 320 provides 32%

(320 mg/ml) organically bound iodine. The low Z iodine preferentially attenuates low kV x-rays by the photoelectric effect. The reduction in low photons penetrating the balloon is viewed by the CT's algorithm as if the balloon were equivalent in Hounsfield Units (HU) to bone. Kassas (Kassas, et al., 2004) has shown that radiopaque contrast percentages, ranging from 5% to 25%, produced reduction in dose at one centimeter beyond the balloon edge as seen to range from -0.8% to -5.7% respectively. Similar results were reported by Kirk (Kirk, et al., 2004) and Cheng (Cheng, et al., 2005) when dose perturbation factors (DPF) were analyzed. Kirk measured a change of DPF ranging from 0.99 to 0.87 based upon a 6% contrast ratio up to 100%. Cheng found the DPF to be on average 0.965 for contrast ratios ranging from 5% to 25%. Zhang (Zhang, et al., 2007) also found similar percentage reduction in doses for contrast ratios ranging from 5% to 25% iodine to saline, where the dose reduced was found to be -0.64% to -6.17%. Oh (Oh, et al., 2009) found ratios with contrast to without contrast varying from 10% to 25% concentrations and at measured distances to simulate a 35 cm^3 to as large as 60 cm^3 to range from 0.982 to as low as 0.948. These reports suggest that, due to the introduction in radiopaque contrast alone, TG43 calculations underestimates dose at distances beyond the balloon by as little as 1% and up to as much as 6.17%.

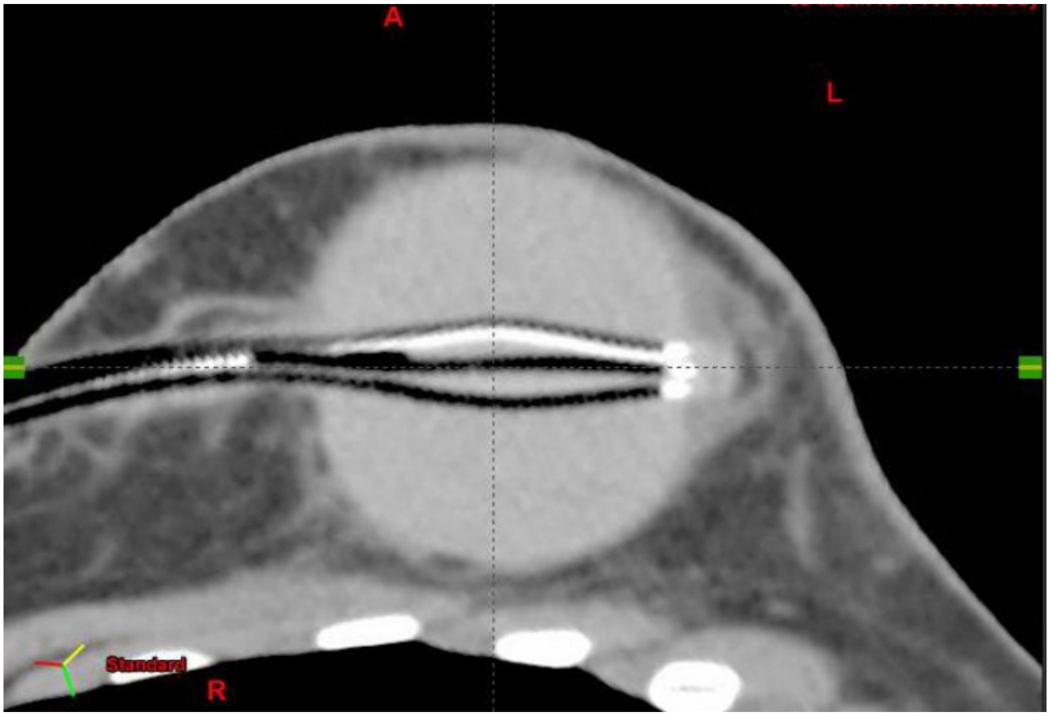

Figure 4. CT axial scan showing contrast inserted inside balloon for visualization. Courtesy of HOLOGIC, Inc. and affiliates.

Authors Huang (Huang & Blough, 2010) and Richardson (Richardson & Pino, 2010) investigated air pockets that exist within the brachytherapy APBI treatments for the MammoSite and the SAVI, respectively. Huang shows that if air cavities are present adjacent to the balloon surface and the planning system cannot account for heterogeneities in its calculations then the breast tissue dose can be estimated using the traditional inverse square law. The SAVI does not include a balloon in its design so the lumpectomy cavity is either void of fluid or sometimes contains a partial volume of seroma as seen in Figure 5. Richardson compared MC simulations and measurements of the SAVI to quantify dose differences ranging from 3% to 9% from multi-dwell SAVI plans with small to large diameters.

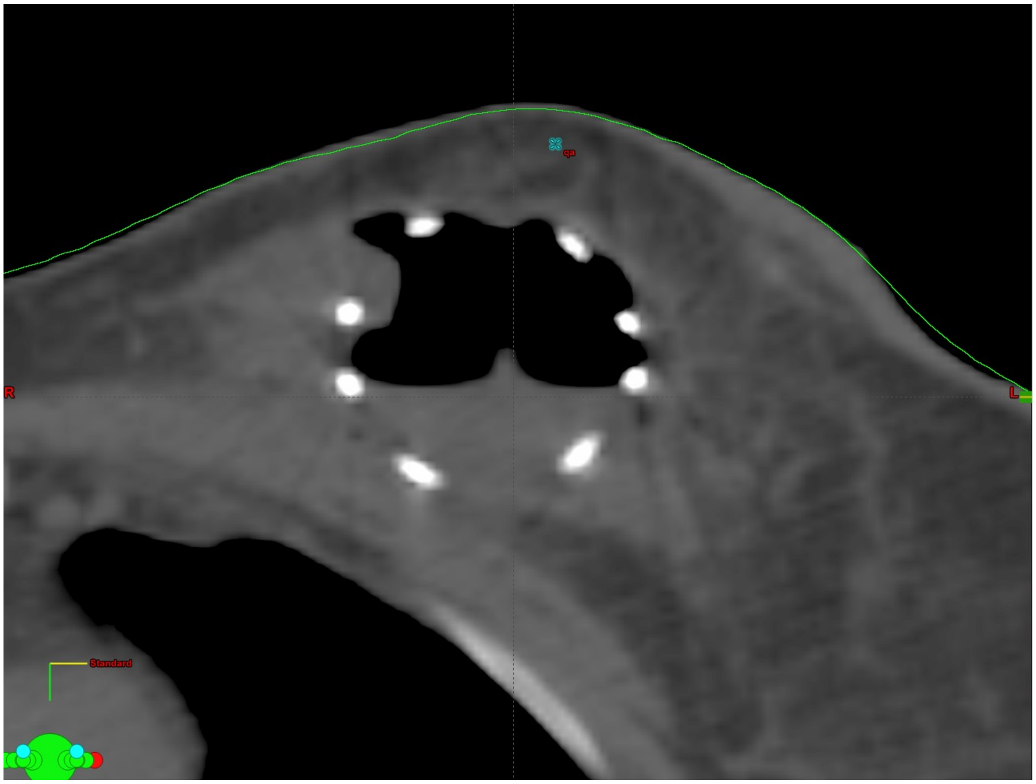

Figure 5. Axial scan of a SAVI in-vitro showing half-filled cavity of seroma fluid. Permission from Arizona Center for Cancer Care, LLC.

The effects of finite boundaries have also been investigated by Cazeca (Cazeca, et al., 2010). Cazeca modeled a MammoSite balloon placed in an average size breast phantom in which MCNP5 was used with F6 point tallies to demonstrate the decreased dose closest to breast-air interface. Cazeca found up to a 6.3% decrease at a point closest to the breast-air interface when the F6 ratio was taken between finite phantom and the infinite phantom. TG43 over predicts dose at skin-air boundaries by up to 6%, while using a GBBS will account for the density change and lack of scatter, providing a more accurate representation of the dose distribution for the clinicians.

2.1.2. eBx

The most recent single entry device to become available is the Xoft Axxent Balloon (subsidiary of iCAD, Nashua, NH) applicator, shown in Figure 6. This device is used exclusively with the complementary Xoft Axxent X-ray (eBx) source, which is a novel design of a miniature x-ray tube pictured in Figure 7. While the physical specifications of the eBx is proprietary, it is known to rely on the same anode-cathode method as traditional x-ray tube. In the clinical setting it typically operated at a maximum value of 50 kVp (White, et al., 2014). At the 50 kVp potential, the average photon energy emitted from the eBx is 27 keV. An advantage of the eBx is that it can offer similar dose rates as the HDR ^{192}Ir treatments, but operate inside a minimally shielded room due the low energies. The eBx balloon is very similar to the MammoSite as the balloon is designed to accommodate the eBx x-ray into one lumen centered in the lumpectomy cavity. Unlike the MammoSite, however, no contrast is injected into the liquid filling the balloon as the iodine would significantly attenuate the low kV energy photons. Instead, the balloon is made of a barium sulfate contrast (Mille & Xu, 2010) to allow CT and x-ray radiographs to visualize its position inside the patient's body. Xoft Inc. (Xoft Inc., 2009) has shown that over the range of balloon sizes available for treatment, the reduction of exiting dose beyond the balloon is reduced by only 6%.

Figure 6. The Xoft Axxent Balloon applicator used exclusively with Xoft Axxent X-ray source. Courtesy of XOFT, a subsidiary of iCAD, Inc.

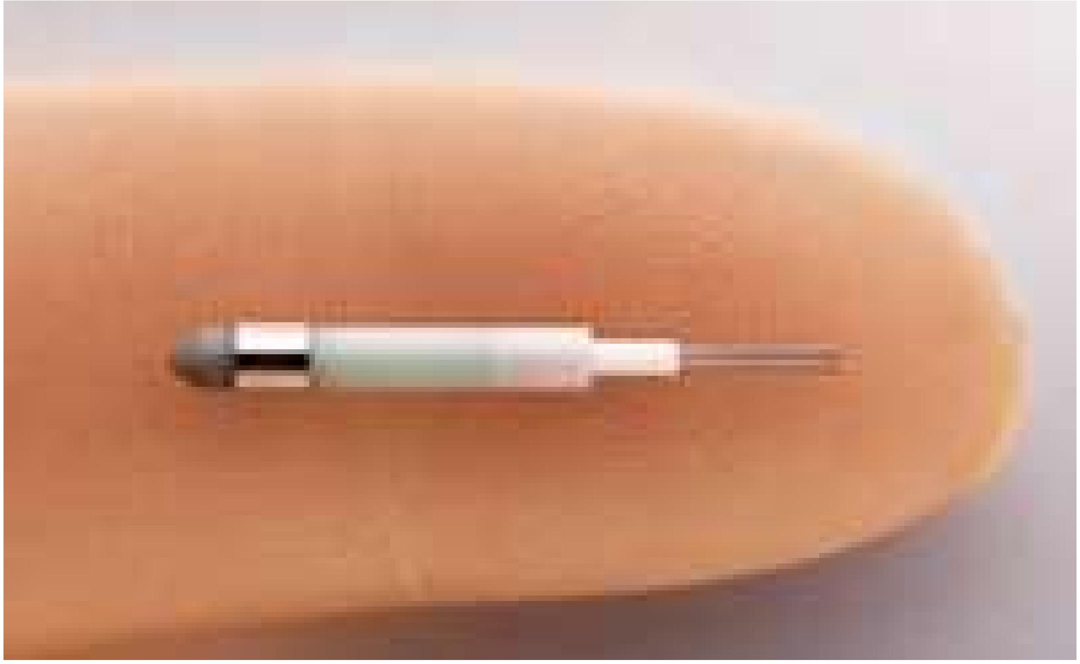

Figure 7. Xoft Axxent Xray source. Courtesy of XOFT, a subsidiary of iCAD, Inc.

Limited research has been conducted examining the effects of air cavities, skin-air edge and breast bone interfaces when using the eBx source. Mille (Mille & Xu, 2010) compared predicted organ dose of ^{192}Ir and eBx inside a mock female phantom using MCNPX F6 tallies. The results confirmed the expected dose reduction to healthy tissue by the low energy eBx source and most notably indicated the maximal rib dose ratio increased by 5.4 times for eBx when compared to ^{192}Ir. Mille (Mille & Xu, 2010) went on to remark that this rib dose increase was due to the, “larger mass attenuation coefficient of bone at low energy attributed to increased photoelectric absorption" (p. 667).

Landry (Landry, et al., 2010) (Landry, et al., 2011) also reports, in two separate papers, on the sensitivity of the low energy spectrum to variations in material compositions. Landry also showed that the three reporting options, now available by some MBDCAs, $D_{w,m}$, $D_{m,m}$ and $D_{w,w}$ needs to be investigated and a consensus on the reporting method to be chosen due the extreme variability in the chosen medium being reported for dose. $D_{w,m}$ is photons are transported in the material and absorbed dose is calculated to a small volume of that water in lieu of that material. $D_{m,m}$ is photons are transported in a medium and the dose is calculated to small volume of that material. While $D_{w,w}$ is the classic method for reporting dose. Landry showed that human tissues that had large Zeff differing from water, in this cases adipose tissue and mammary glands, showed $D_{w,m}/D_{m,m}$ ratios of up to 1.66 at a distance of 1 cm lateral to point sources.

The limited research investigating eBx MBDCA aside from MC is indicative that current models do not account for the low energy spectrum coupled with the transport modeling required to accurately predict dose through composite materials of bone, lung, and air.

2.2. TG-43 Overview

As of January 2017, the most accepted dose calculation used by TPS in brachytherapy planning was published over twenty-years ago, in 1995 by American Association of Physicists in Medicine (AAPM). The report was written by Task Group 43 (Nath, et al., 1995) (TG43) and later updated in TG43 U1 (Rivard, et al., 2004). Since the new formalism was adopted, TG43 report has been referenced extensively and a current search through online American Institute of Physics (AIP) citation shows over seven-hundred and fifty results mentioning TG43.

Some of the benefits that TG43 brought the medical physics community was the new formalism would make dose calculations for brachytherapy incorporate actual manufacturers' source model and utilize standardized datasets (Rivard, et al., 2004). These data sets for the source models were either measured by TLDs or modeled using MC simulations in water.

TG43 states that one of the original problems with classical brachytherapy dose calculation methods was that the factors were based upon measurement done in free space, while the new computers rely on the surrounding medium to be tissue equivalent, or more so, water density. A few flaws pointed out by Rivard (Rivard, et al., 2009) upon review of the classical brachy calculations were concerning source activity and gamma coefficients. As for activity there appeared to be confusion between real, effective, assumed and apparent when relating to the source strength. Rivard also pointed out that from the investigation by Jayaraman (Jayaraman & Lanzla, 1983) literature review showed large discrepancies for choices of exposure rate constants. One constant given in earlier calculations prior to 1978 was that exposure rates constants for ^{192}Ir were reported to vary from 3.9 to 5.0 R cm^{2} mCi^{-1}h^{-1}. This discrepancy was primarily reported due to inconsistent practice of specifying activity between manufacturer and customer choice.

TG43 formalism replaced the more traditional brachytherapy dose calculation as follows.

Equation 1

$$D\ (r) = A_{app}\ f_{med}\ (\Gamma_{\delta})_{x}(1/r^{2})T(r)\phi_{an,}$$

Where:

A_{app} is the apparent activity of the source;

f_{med} is the exposure-to-dose conversion factor;

$(\Gamma_{\delta})_{x}$ is the exposure rate constant for the radionuclide in the source;

T(r) is the tissue attenuation factor;

ϕ_{an} is the anisotropy constant.

Equation 1 assumes a point source and was initially adequate since prior to 1995 it was uncommon practice for the clinical TPS to utilize imaging, such as CT. Therefore, all calculations using Equation 1 were performed to a volumetric area that disregarded source orientation and target volumetric coverage.

TG43 goes on to state that cylindrical sources exhibit substantial anisotropy and that it is next to impossible to take free air measurements around these sources and convert them into water equivalent dose. Therefore, TG43 recommended the use of an anisotropic factor, in lieu of an anisotropic constant. The new equation recommended from TG43 used for ^{192}Ir is as follows:

Equation 2

$$D(r, \theta) = S_K \Lambda [G(r, \theta)/G(r_0, \theta_0)] g(r) F(r, \theta)$$

Air Kerma Strength (S_K) replaces the old A_{app} (activity apparent).

Λ is defined as the dose rate constant with units of cGy h-1U-1

$G(r, \theta)$ is the geometry factor which accounts for the spatial distribution due to the construction of the actual source. In this scenario an ^{192}Ir is approximated by a line source yielding the equation:

Equation 3

$$G(r, \theta) = \beta / (Lr \sin \theta)$$

Where L is the active length of the source, β is the angle subtended by the active source with respect to the point (r, θ).

The radial dose function $g(r)$ accounts for the absorption and scatter in the medium along the transverse axis of the source. This value only applies to the transverse axis where $\theta = \pi/2$.

$F(r, \theta)$ = anisotropy function. This accounts for the anisotropy of the dose distributions around the source due to absorption and scatter in the medium.

This advancement in the algorithm has a simple approach to account for the 3D nature of the dose distribution. Superposition of multiple sources also assisted in predicting volumetric implants to be optimized whereas previous classical calculations viewed the implant as a volume with no correlation to the actual targeted area. It was also standard to assume that dose distributions were deposited in water and therefore, secondary QA tests were performed to reflect a point source in water.

While the QA hand calculations are able to check more complicated source distributions, it requires that water is the medium.

TG43 was not designed to accommodate composition of different materials and tissues that are inherent to patients or introduced by treatment devices. It was also not designed to fully characterize the radiation transport and energy deposition due to the changes in mass energy-transfer coefficients. These assumptions, also transfer to the planning system, which treat the breast, catheters, bones, lungs, and surrounding air as water. As stated by Christopher Lee (Lee, 2014) in 2014, "It is currently unusual for commercial brachytherapy planning systems to use MC modeling or to consider the inhomogeneities of real life situations."

2.3. MCNP5

MCNP5 v1.6 from Los Alamos National Laboratory is a general-purpose Monte Carlo N-Particle code that can be used for neutron, photon, electron, or coupled neutron/photon/electron transport (X-5 Monte Carlo Team, 2003). MCNP transports across three-dimensional modeling of sources and phantom materials by treating regions and overlapping regions as boundaries or zones, as first- and second-degree surfaces.

Continuous energy cross-section data are used by MCNP to simulate photon interactions including incoherent and coherent scattering, photoelectric absorption, and absorption in electron-positron pair production (X-5 Monte Carlo Team, 2003).

MCNP and the MC method has long been considered the gold-standard for dose calculations (Williamson & Zuofeng, 1995) (Daskalov, et al., 1998) (Karaiskos, et al., 1998) (Papagiannis, et al., 2002). The method allows the user to define a neutron photon or electron source of specified dimensions, and stochastically model the interaction probabilities within the defined material. Within the defined space in MCNP, interactions due to particles and photons are tracked and tallied in a variety of ways. This research utilizes both the F6 and *F8 tallies. The F6 tally is a track length estimate of dose deposition, that is based on KERMA and displayed in MeV/g. The *F8 tally more accurately reflects dose distribution by further tracking electron energy deposition using a condensed history algorithm and are provided in MeV.

2.4. Attila™

Attila™ (Transpire, Inc., Gig Harbor, Washington) is a deterministic solver of the linear Boltzmann transport equation (LBTE) created at Los Alamos Research Laboratories. Gifford (Gifford, et al., 2006), writes, "The deterministic approach to solving the LBTE involves discretizing all variables, energy (multigroup approximation), space (finite-difference or finite-element) and angle (discrete-ordinates)" (p. 2253-2254). As many authors (Gifford, et al., 2006) (Gifford, et al., 2008) (Vassiliev, et al., 2010) (Kan, et al., 2013) mention, MC has been the most accurate method for calculating the photon transport needed in radiotherapy. Since MC is adequate for simple space designs and better if only one source, if one takes the typical complexity of the radiotherapy patient scenarios, MC becomes time prohibitive. These deterministic solvers of the LBTE on a mesh is referred to as a grid-based Boltzmann solver (Vassiliev, et al., 2010) (GBBS). Both Gifford and Vassiliev asserts that given enough time and using the same cross-section data with sufficient detail in space, energy and angle, both MC and GBBS will converge on the same solution. A major advantage to using GBBS is that based upon the assumptions made when discretizing the scenario, the efficiency of calculations compared to MC is significantly improved. The deterministic nature of the GBBS reduce calculation times compared to the explicit modeling of large number of histories required for MC.

The Attila interface allows the user to define complex 3D created CAD drawings. Spatial discretization is performed automatically during the import into Attila using a unstructured tetrahedral mesh, according to Gifford. Attila is also very versatile in its ability to define source terms. Users are allowed to enter complex composition of materials and the associated multigroup cross sections that are generated using coupled electron-photon cross section generating code (CEPXS) (Lorence, et al., 1989). The energy discretization is accomplished by taking the maximum particle energy range $E_{min} \leq E \leq E_{max}$ and converting the spectrum into a finite number of intervals (Gifford, et al., 2006).

2.5. Acuros™ BV

The Acuros™ BV (Varian, Palo Alto, California), known further as Acuros, is a specialized adaptation of Attila that is specific to ^{192}Ir brachytherapy, and remains a numerical solver for the Linear Boltzmann Transport Equation (LBTE).

Acuros was designed specifically as an alternative to MC where calculation speed is necessary in clinical environments. Acuros solves the static, or time-independent, form of the LBTE. For a computation volume, V, with surface, δV, the LBTE is given by:

Equation 4

$$\hat{\Omega} \cdot \vec{\nabla}\Psi + \sigma_t \Psi = q_{scat} + \sum_{p=1}^{p} \frac{q_p}{4\pi} \delta(\vec{r} - \vec{r_p})$$

Equation 5

$$\Psi = 0, \vec{r} \in \delta V, \widehat{\Omega} \cdot \vec{n} < 0$$

"The LBTE, Equation 4, is a six-variable integro-differential equation which is solved in Acuros™ BV by discretizing three variables in space, two variables in angle, and one variable in energy"(p. 15) (Varian Medical Systems, Inc, 2009).

Zourari (Zourari, et al., 2010) showed comparisons of single sources bound inside a homogenous water phantom with 15 cm radius between Acuros and MCNPX. Their results showed a 1% agreement over most points with the largest errors of 2% to 3% at points lying on angles from the longitudinal axis.

Acuros source library is predefined from the manufacturer's dimensions and spectrum for the Varian HDR and PDR sources. The geometry of the space along with Varian's predefined voxel spacing and HU information are sent to the Acuros solver inside the TPS.

2.6. MOSFETS and Diodes

The two detectors used to perform physical measurements of the ^{192}Ir source are the semiconductor solid state dosimeters (diodes) and the Metal Oxide Field Effect Transistor (MOSFET). These silicon based detectors were chosen particularly for their small active volumes. The diodes used were the Equidose® II diode detectors (CNMC, Nashville, TN) having a detector size of 0.8 x 0.8 mm^2. The MOSFET is model TN-502RD (Best Medical Ontario, Canada) which has an active region of 0.2 x 0.2 mm^2. These small volumes gave excellent pinpoint measurements.

Advantages of the diodes is that they give immediate readout, show high sensitivity with good stability (Tanderup, et al., 2013). The Equidose® II detectors demonstrate low degradation of response even at high levels of radiation doses up to 30,000 Gy. The disadvantages of diodes include their dependence on direction, energy, and temperature.

MOSFETs demonstrate nearly isotropic response to radiation, and can be designed to reduce the temperature dependence as was done with the Best Medical dual-MOSFET-dual bias detector. Soubra (Soubra, et al., 1994) demonstrates the dual-MOSFET design offers greater stability than traditional MOSFETS in linearity, reproducibility, response stability and temperature dependency. They have also been used for ^{192}Ir measurements for brachytherapy cases such as by Qi (Qi, et al., 2007) and Oh (Oh, et al., 2009). Qi quantified that relative deviations between the measured doses and planned doses with MOSFETs to be under 5%. Oh used MOSFETs to measure full scatter and lacking full scatter breast phantom ^{192}Ir treatments. The comparison between MCNP and MOSFET predicted dose using measurements were in good agreement.

2.7. Reasons to Adopt MBDCAs

The implementation of TG43 creates standardization of data sets used in brachytherapy dose calculations and at the time helped to increase the accuracy of clinical results (Rivard, et al., 2009) (Beaulieu, et al., 2012) . Yet, the data was obtained in liquid water phantom or calculated by MC assuming water, therefore, there are many dosimetric parameters that are inherently not taken into account.

However, due to the short stopping ranges of typical brachytherapy source electrons, charged particle equilibrium (CPE) exists within millimeters of the brachytherapy source surface. Since CPE exists and there are low radiative losses due to the low energies of these sources, absorbed dose to water, D_w, can be approximated by Kerma, or K_w, alone.

Dose to water for brachytherapy sources can then be written as in equation 6.

Equation 6

$$Dw \cong K \cong Kcoll \cong \Psi(\frac{\bar{\mu}_{en}}{\rho})$$

As can be seen in Figure 26, ratios of $\frac{\bar{\mu}_{en}}{\rho}$ for typical human body tissues to water are shown. TG43 can over and under estimate dose to tissue while MBDCAs will take the mass-energy absorption coefficients for various materials into account.

TG43 also overestimates the dose at the patient's tissue-air interface as shown by Lymperopoulou (Lymperopoulou, et al., 2006) and Pantelis (Pantelis, et al., 2005) Both authors comment that part of the data used for TG43 is calculated by MC with the source sitting in the center of a water phantom whose radius is at least 15 cm and up to 40 cm for higher energy brachytherapy sources. Therefore, at a distance away from the source the TG43 data relies heavily upon scatter contribution. Both Lymperopoulou and Pantelis investigations show the overestimation of TG43 calculated doses at the tissue-air interfaces. Although, Pantelis suggests this can be viewed as a safety margin when determining appropriateness of treatment plans when the limiting skin dose is taken into account.

Another important advancement when transitioning to MBDC algorithms is the option for the reporting dose to various mediums. Current practitioners have decades of patient data that was scored to water, $D_{w,w}$, as the medium. Acuros offers the user the option to specify the resultant calculations either in dose deposition in the medium but scored in water, $D_{w,m}$; the dose to medium and scored in the medium, $D_{m,m}$; and dose transported in water and scored in water, $D_{w,w}$. While the reporting for external beam radiation therapy (EBRT) has been advised to use $D_{w,m}$ because at EBRT energies, mass energy absorption coefficients between human tissues does not vary greatly. Alternatively, due to the large role that photoelectric interactions play at low energy brachytherapy ($\leq {}^{192}$Ir), Rivard (Rivard, et al., 2009)$^{)}$ and Beaulieu (Beaulieu, et al., 2012) suggest reporting $D_{m,m}$. Landry et al.$^{(E)}$ showed for low energy sources, ≤50 keV, photon energies that $D_{w,m}/D_{m,m}$ for Adipose tissue and eBx is a ratio of 1.64 -1.67. This jump comes from Adipose tissues effective Z, and when compared to water at the low energy which subsequently gives large differences in the mass-energy absorption coefficients.

Recommendations from TG186 in moving from the TG43 to an MBDCA are summarized as follows. Initial investigations should focus on modeling an unbounded, or a bounded phantom with radius of 40cm, and calculating a centered brachytherapy source using both TG43 and the MBDCA. The comparison should show good agreement.

Another recommendation of TG186 is to calculate the MBDCA on clinically relevant tissues heterogeneities and compare to benchmark cases. The benchmark cases should be calculated using well known and reliable MC code.

3. Materials and Methods

3.1.Acuros^{TM} BV Validation for ^{192}Ir

3.1.1. CT Electron Density Phantom and HU Calibration

The CT Electron Density Phantom (CTEDP) (Sun Nuclear, Middleton, WI), Figure 8, material is made of solid water (ρ = 1.018 g/cm^3) and has a relative electron density of 0.989 g/cm^3. The CTEDP disk has dimensions of 33 cm diameter and 5 cm thickness. This disk has sixteen evenly spaced cylindrical holes drilled around the center of the axis. The inner radius contains eight holes evenly spaced at a radius of 5.5 cm from the axis, while the outer eight holes are evenly spaced at a radius of 10.5 cm from central axis. The commercially available CTEDP comes documentation of the manufacturer's calibrated density in both physical and electron density for each plug. All sixteen plugs were inserted into the CTEDP and arranged so as to minimize artifacts during the CT scan. The CTEDP was then placed onto the CT table such that the plugs were perpendicular to the CT detector rotation. The density of the plugs varies from 0.29 g/cm^3 to 1.823 g/cm^3. This variation in densities allows the user to confirm the CT rendering and averaged Hounsfield Unit as described at the console of the CT scanner.

The use of the CTEDP in this research was to show confirmation that Varian BrachyVision would be interpreting the Hounsfield Units (HU) sent from the CT scans appropriately. A GE 4 slice CT scanner (General Electric, Fairfield, Connecticut) was used to scan the CTEDP. All sixteen plugs were inserted into the phantom and placed onto the CT table such that the plugs were perpendicular to the CT detector rotation. For this measurement, the CT scanner settings were set to the clinics customary 120 kVp, while current was automatically optimized by the scanner. The slice thickness was set to 2.5 mm to provide a high spatial resolution and reduce voxel averaging between adjacent slices. Once the CT scan was performed, the GE CT console software allowed measurements to be performed by placing a scribed square on the CT screen that measures and displays a mean value of Hounsfield Units from within the square (shown in Figure 9). The average HU for each CTEDP plug was measured and tabulated. Table 1 shows the relationship between increasing density and Hounsfield Unit. The CT scans of the CTEDP were then exported via a network in Dicom format. Within the TPS, the Dicom images were imported and rendered three dimensional. The TPS also allows the operator the use of a tool to scribe a square of equal dimensions to the CT. Each plug had its HU and SD measured and those results are also shown in Table 1. Dr. Roberto Molteni wrote in his AAOMR presentation (p. 6) “The Hounsfield Units (HU) is a linear transformation of the linear attenuation coefficient measurement into one in which the radio density of distilled water (at standard pressure and temperature) is defined as zero HU, while the radio density of air at STP is defined as -1000 HU. For a material X with linear attenuation coefficient μ_x, the HU value is therefore given by:” (Molteni, 2011)

Equation 7

$$\boldsymbol{HU} = \frac{\mu_{\mathbf{x}} - \mu_{\mathbf{water}}}{\mu_{\mathbf{water}} - \mu_{\mathbf{air}}} * \mathbf{1000}$$

Figure 8. CT Electron Density Phantom

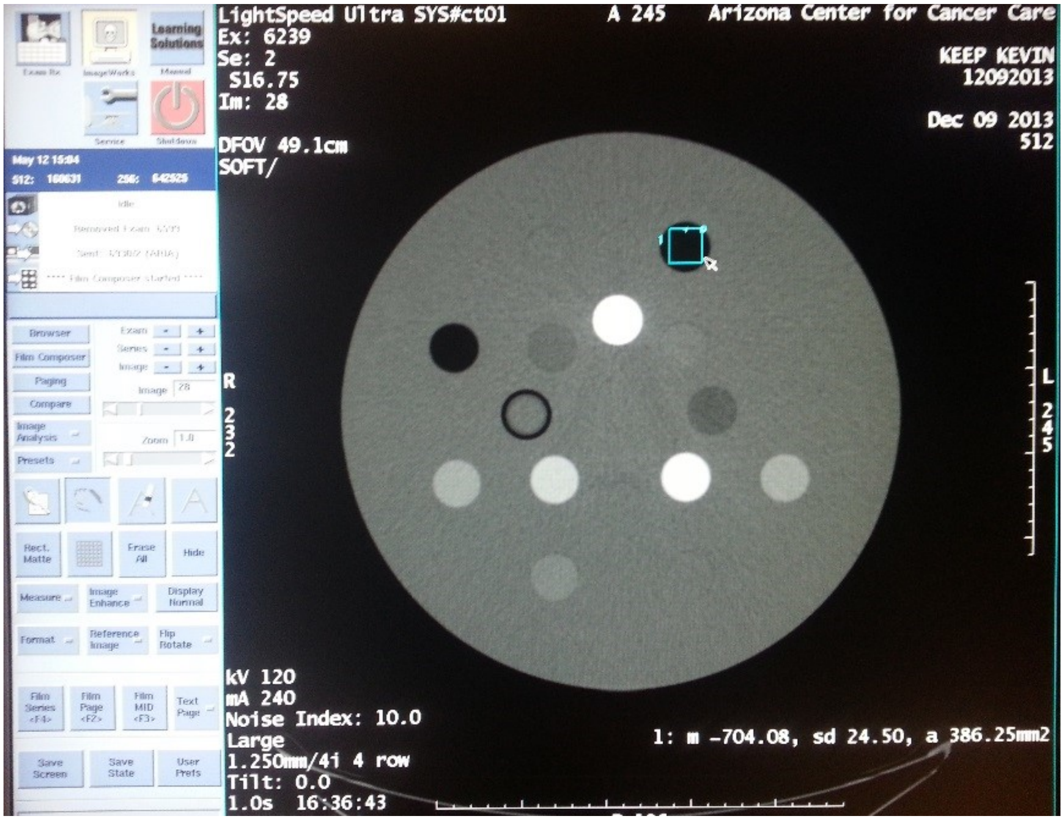

May 12 15:04
512: 160631 256: 642525
Idle
**** Film Composer started ****
Image 28
Zoom 1.0

LightSpeed Ultra SYS#ct01
A 245
Arizona Center for Cancer Care
Ex: 6239
Se: 2
S16.75
Im: 28
KEEP KEVIN
12092013
Dec 09 2013
512
DFOV 49.1cm
SOFT/
kV 120
mA 240
Noise Index: 10.0
Large
1.250mm/4i 4 row
Tilt: 0.0
1.0s 16:36:43
1: m -704.08, sd 24.50, a 386.25mm2

Figure 9. CT Electron Density Phantom scan for Hounsfield Unit confirmation.

Table 1. Hounsfield Unit comparison CT to Varian BrachyVision.

CT Electron Density Phantom						
	Physical	Electron	HU for GE CT		Eclipse (HU)	
	Density	Den. Rel.	Measured	Measured	Measured	Measured
Rod Type	(g/cm3)	Water	Mean	SD	Mean	SD
Ln-300	0.290	0.286	-704.1	24.5	-707.2	25.9
Ln-450	0.480	0.465	-512.4	34.7	-518.9	23.5
AP6 Adipose	0.943	0.926	-86.5	20.1	-88.1	20.8
BR-12 Breast	0.979	0.956	-43.2	20.3	-44.5	22.5
Water	1.000	1.000	4.6	19.0	2	23.0
CT Solid H2O	1.018	0.989	.1.7	21.7	2.5	20.6
"	1.018	0.989	1.8	19.6	3.6	19.5
"	1.018	0.989	2.2	21.3	2.7	21.3
"	1.018	0.989	2.2	17.2	3.7	17.4
BRN-SR2 Brain	1.053	1.049	29.8	29.8	28.9	24.4
LV1 Liver	1.090	1.059	72.3	15.7	73.5	18.3
IB Inner Bone	1.140	1.093	221.4	18.7	215.1	19.1
B200 Bone Mineral	1.152	1.104	226.5	17.7	227.3	17.8
CB2-30% CaCO3	1.335	1.280	447.0	22.5	451.2	22.5
CB2-50% CaCO3	1.559	1.469	801.8	23.8	807.9	28.5
SB3 Cortical Bone	1.823	1.695	1202.0	30.6	1202.5	34.5

The importance of the HU to the results from Acuros comes from interpretation of the voxel HU during calculations. BrachyVision supplies to Acuros the average HU of each voxel, and Acuros then determines the material from a predetermined lookup table that is recreated in Table 2. The material composition is necessary for Acuros to determine which macroscopic cross sections to apply for each voxel during calculations. The lung, adipose tissue, skeletal muscle, cartilage and bone densities are shown in Table 2.

3.1.2. Design of the QA Phantom (QAP) and Importing

For the purposes of this investigation, a new design for a phantom that allows the user to test any MBDCAs ability to correctly account for heterogeneities was created. The design allows for calibrated heterogeneities to be alternated in a fixed geometry such that any MBDCA model can analyze their transport code when applied. It has been shown that MBDCAs can be compared to the industry gold standard MC, therefore, this Quality Assurance Phantom (QAP) tests will focus on MC comparisons as well as physical measurements. The MBDCA for this study will be Acuros.

The original design of the phantom was a small clear plastic box that would hold water. A platform was created using two thin plastic sheets cut to the rectangular dimensions that fit snugly into the box. These two sheets were held apart by plastic washers and screws to reduce CT artifact. Both of the plastic sheets had holes cut to allow the insertion of one of the density plugs, and hold the plug firmly in place. Another hole was cut approximately 1 cm from the density plug hole to allow a six French hollow tube to be placed in this void that would allow the ^{192}Ir source a hollow tube to travel into the box phantom with reproducible setup. The platform was then placed horizontal into the insect box. This box water phantom idea was cancelled due to the following problems: 1) the platform would float when the Lung-300 (ρ = 0.29 g/cm^3) plug was inserted, 2) allowing the source to travel into a tube submerged in water was risky should the hollow tube leak, 3) the platform was so tight, it retained air cavities that would not escape. The greatest concern was if problem two did occur, it would rust the ^{192}Ir source and render it unusable for patients.

The final QAP design that was used for this research was a sheet of Plastic Water® (PW) having dimensions of 30 cm X 30 cm X 5cm, shown in Figure 10. Plastic Water® is stated as being fabricated from epoxy resins and powder to control density and radiation properties. The manufacturers also state that it has a density of 1.02 g/cm^3. A GE CT scan of this 5 cm slab showed the average HU = 62, which correlated to a density of 1.058 g/cm^3 from Table 1. While this slab did not have any accompanying manufacturer's chemical composition paperwork for review, the material would be uniform for all measurements making it ideal. Therefore, the disturbance of the fluence from the Plastic Water's® unknown composition would be uniform for all measurements.

The QAP was next drilled with two holes as shown in Figure 10. The first hole was located four and one-half centimeters from the block edge and was cut to the diameter of three millimeters. This hole accommodates the insertion of a six French hollow catheter tube with no air gaps. These six French tubes are sold by the HDR manufacturers and provide the radioactive source attached to its travel wire a confined travel path. The second hole was placed 0.5 cm from the phantom edge between the first hole and the phantom's edge. This hole was drilled with a three-centimeter diameter to accommodate the density plugs. Each plug is approximately three-centimeter in diameter and fit snug within the cut hole so that air gaps were minimized. The holes were drilled such that the detector placed on the outside edge of the phantom would be perpendicular to the ^{192}Ir source and the shortest distance between the source and detector would pass perpendicular through the plug's diameter.

Figure 10. Solid water phantom 30x30x5 cm^3

The next part of the study was the acquisition of the QAP. The QAP was placed flat on the CT table and scanned using the high resolution scan setting of 2.5 mm slices with axial cuts. Axial cuts were chosen, instead of helical acquisition CT slices, to reduce the averaging of pixel information between slices since the CT scanner was an eight slice. Therefore, the axial cuts provided better resolution of the QAP. Five CT scans were taken, one for each different density plug inserted into the hole. The fifth scan the hole was left empty. The materials were chosen to be as naturally occurring in a human body as possible. They were the Solid Water ($\rho = 1.018$ g/cm^3), the water plug ($\rho = 1.000$ g/cm^3), the lung Ln-300 plug ($\rho = 0.29$ g/cm^3), the cortical bone SB3 Cortical Bone ($\rho = 1.823$ g/cm^3), and of course the void or air ($\rho = 0.001225$ g/cm^3 at STP). Each set of axial scans was imported into the BrachyVision planning system, where the pre-determined CT Hounsfield Unit file was applied to each CT set automatically by the planning system.

All five CT sets had outlines manually drawn to show the exterior shape defining the body of the QAP and the plug. While each plug was defined as the physical dimensions of cylinder size three centimeter in diameter the actual material was not globally defined as a specific composition. Instead, it was left to BrachyVision to determine the HU for each voxel and pass this information over to Acuros, a decision that would most likely simulate actual clinical use. The area that had been left void of a plug, or air, was simply included into the exterior drawing so that Acuros would incorporate this area during calculations. The pictures shown in Figure 11 demonstrates the noticeable differences seen by the planning system.

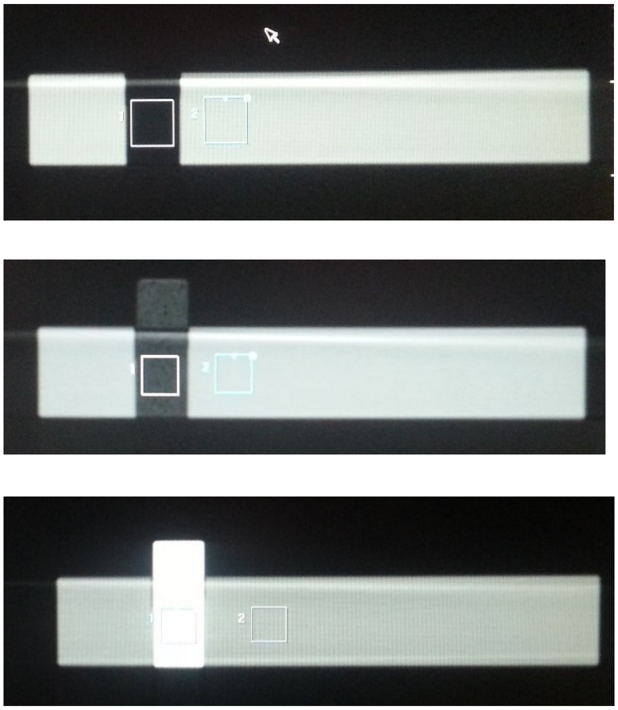

Figure 11. Examples of air, lung and cortical bone plugs.

Next the placement of the ^{192}Ir seed was defined. The three-millimeter hole mentioned earlier was used as a guide in BrachyVision to delineate the path that the ^{192}Ir source would travel through. The travel path is drawn starting with the most distal position or tip of the tube and then points are chosen along the travel path to the end of the defined tube or most proximal position. The user may define this travel path by mouse clicks directly on the computer rendered images. BrachyVision can then simulate stopping positions of the ^{192}Ir source, called dwell positions. The length of activation and frequency of dwell positions can be defined by the user up to a resolution of 1 mm steps. For all five QAP scenarios a single dwell position was used. This dwell position was chosen to be at the center of the phantom along the 3mm tube and given coordinates of (0, 0, 0) at the dwell position's center as seen in Figure 13.

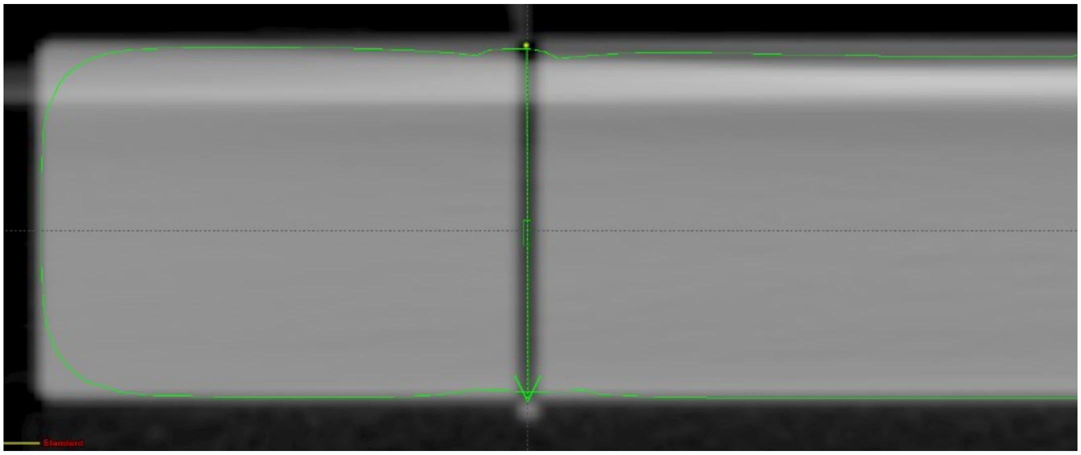

Figure 12. BrachyVision display of the 192Ir source wire.

In Figure 13, a point was defined at (0, 0, 5 cm) that would serve as the reference calculation point (CP). The CP will also be the physical location on the QAP for the placement of the MOSFET and Diode during all measurements. Upon advisement from Varian BrachyVision help desk, the defined volume for calculations was reduced to 12x8x5 cm^3 to give better calculation resolutions.

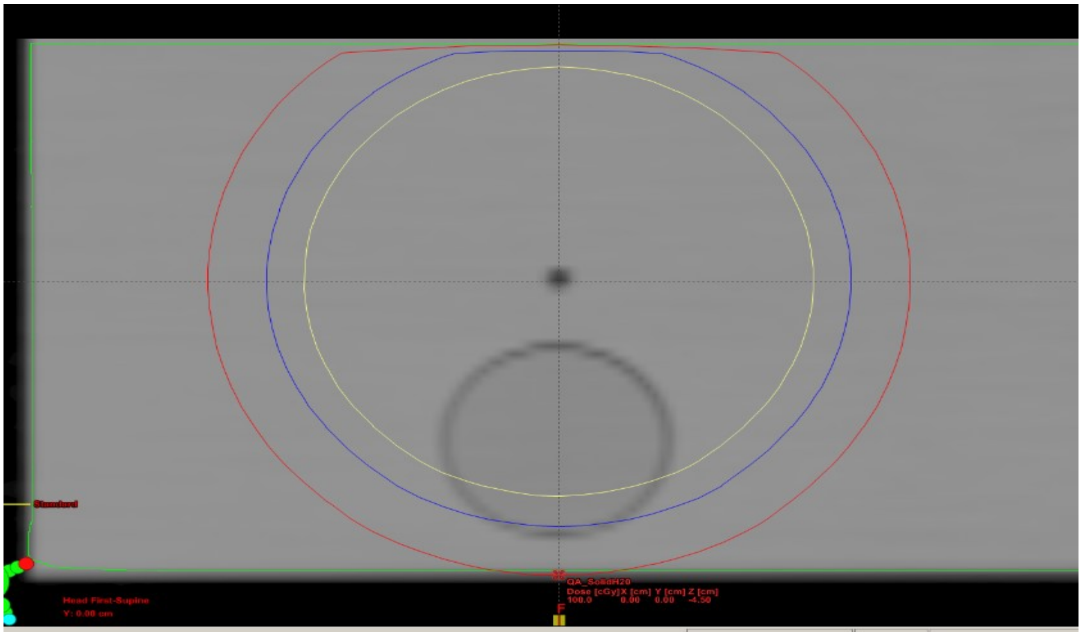

Figure 13. BrachyVision display of Calculation Point

3.1.3. Application of Acuros^{TM} BV

BrachyVision allows the user to display dose either as $D_{w,m}$ or $D_{m,m}$ after calculating with Acuros. Regardless of whether the dose display material is left as water or the actual material, Acuros uses a cross-section library of common patient material properties which is available inside BrachyVision shown in Table 2. This material library contains the CEPXS (Lorence, et al., 1989) (Sandia National Laboratories, Albuquerque, New Mexico) generated macroscopic atomic cross sections. CEPXS software is a multi-group coupled electron-photon cross-section generating code. The CEPXS software does not account for Rayleigh (coherent scatter) which did not play a significant role at the ^{192}Ir energy levels. These macroscopic cross sections are used by Acuros to accurately calculate the photon scatter associated from Compton, photo-electric and pair production for these compounds or mixtures of elements.

If the user wants to display the Acuros results in $D_{m,m}$ then a volume must be drawn inside BrachyVision, which outlines the material to be defined. This volume is then given a macroscopic material property. For this research, the dose display was intentionally left to display the $D_{w,m}$. BrachyVision then takes the HU for each voxel and correlates that to a density. This density information is then given to Acuros which uses Table 2 to determine which cross-sections to use during calculations. The final step then converts the dose in that voxel back to dose deposited as if the voxel were water. $D_{w,m}$ was chosen because it will imitate the practical use of Acuros in the clinic. Choosing $D_{w,m}$ would be the fastest method for calculating a patient in the clinic which is a necessity. The typical planning course in a clinic for breast brachytherapy would be to import the patient's CTs and immediately plan the ^{192}Ir treatment. Attempting to define each area of the breast as adipose tissue, bone, cartilage, lung, and muscle for Acuros to return the results as $D_{m,m}$ would unnecessarily increase the planning time.

Table 2. Material Mass Densities from Varian BrachyVision Recreated.

Material	Density		
	Low (g/cm3)	Nominal (g/cm3)	High (g/cm3)
Air (STP)	0.001	0.001205	0.1306
Lung	0.1306	0.26	0.605
Adipose Tissue	0.605	0.92	0.985
Muscle, Skeletal	0.985	1.05	1.075
Cartilage	1.075	1.1	1.475
Bone	1.475	1.85	2.225

For each of the four scenarios using different density plugs (water, bone, air and lung), Acuros was utilized to calculate the dwell time needed to give 100 cGy at the CP which was 4.5 cm distance along a perpendicular bisector of the ^{192}Ir source. This calculation is accomplished by choosing the Acuros optimizer and typically lasted less than one minute. The resultant dwell times are shown in Table 4. These dwell times were used during the physical measurement of the QAP and also used in the comparison between Acuros and MC.

3.1.4. In-Vitro Validation Measurements of ^{192}Ir

The experimental measurements for the application of Acuros utilized the ^{192}Ir HDR unit, the MOSFET and diode as detectors, and the QAP phantom. Measurements were taken on two separate days and over two months between measurement days

The HDR unit available for measurements was manufactured by Varian Medical Systems (Palo Alto, California). The unit shown in Figure 14 was a GammaMedplus^{TM} iX Remote Afterloader design (GammaMed) that comes available with 24-channels. The design of the GammaMed afterloader has a leaded safe which houses the ^{192}Ir source when not in use. A circular motor extends the wire and source out and retracts the source into the safe. The GammaMed is actually rated to be operated with a 555 GBq (15 Ci) source but in the United States, the GammaMed is only licensable for the 370 GBq (10 Ci) source strength. The GammaMed houses an ^{192}Ir (22.42 g/cm^3) seed that is imbedded inside a stainless steel capsule which a dark blue representation is shown in Figure18. The ^{192}Ir pellet is 0.6 mm diameter and 3.5 mm active length. The capsule dimensions are 0.9 mm diameter and 4.52 mm length. The Air Kerma Rate is 0.063 Gy/h (+/- 5%) for 555 GBq at 1m. The source when loaded for patient treatment begins at approximately 370 GBq (10 Ci). The orange color shows the stainless steel cable that is laser wielded to the end of the stainless steel capsule. The distal end of the seed has a laser wielded end to encapsulate the ^{192}Ir wire. The ^{192}Ir isotope (shown as light blue) is created artificially in a nuclear reactor by irradiating ^{191}Ir (37% abundance) with neutron bombardment. The ^{192}Ir probability of decay is 95% beta decay to ^{192}Pt emitting gamma rays and a 5% probability of decaying via electron capture to ^{192}Os.

Figure 14. GammaMedplus™ iX Remote Afterloader

The available detectors used were the previously mentioned Equidose II skin diodes and the Best Medical Mobile MOSFET. Both detectors were initially calibrated by using a Varian Clinac iX 6MV x-ray beam. The calibration setup used Solid Water® with approximately 10 cm material to give adequate backscatter. A PTW Farmer N30013 0.6 cc (PTW, Freiburg Germany) Chamber along with a PTW Unidos E electrometer, both were ADCL traceable calibrated, were first used to confirm the calibration of the 6MV beam at depth of maximum dose.

Once the 6MV beam was calibrated to 1.00 cGy /MU, the first two centimeters of solid water was replaced with Bolx™ Bolus that is tissue equivalent. Both the MOSFET and diode were placed on the Solid Water® with the appropriate amount of bolus on top to place the detectors at maximum depth dose for a SSD setup, with a 10 x10 cm^2 field.

The Best Medical Mobile software allows the user to adjust parameters within the software such that the MOSFET's response may be calibrated. This calibration must be modified as the response of the MOSFET will change with increasing radiation damage.

The diode electrometer allows the user to modify the response by adjusting the gain on the analog readout. The diode, unlike the MOSFET, has a higher resilience to radiation damage.

Figure 15. Best CNMC Equidose II Diode Detectors

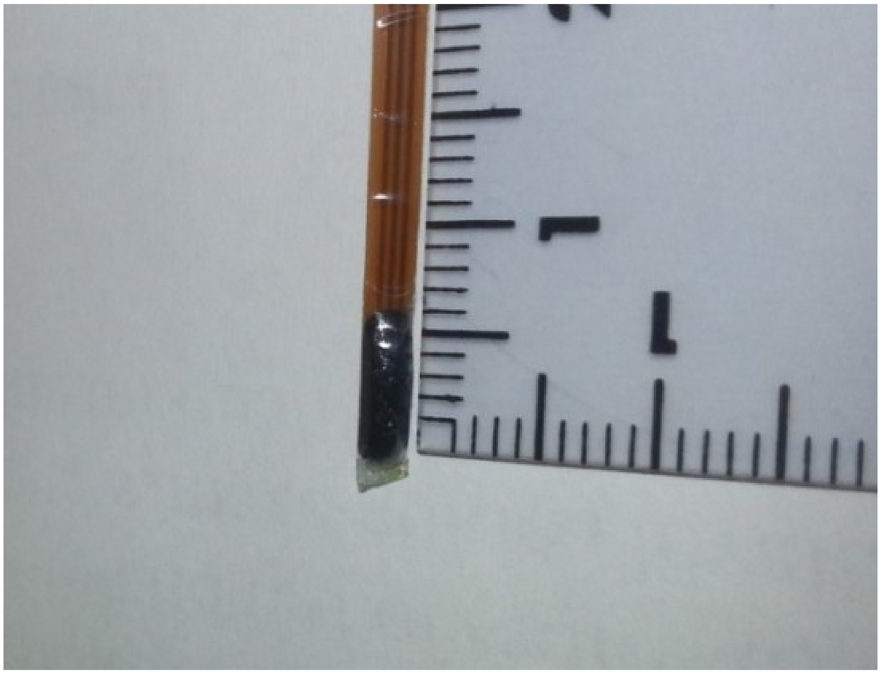

Figure 16 MOSFET model TN-502RD (Best Medical Ontario, Canada)

Once both detectors were calibrated, the QAP was placed on the table with no added scatter as shown in Figure 17. The 6 French transfer tube was inserted into the source hole and connected HDR unit. The QAP had been marked from the initial CT where the calculation point would be located. The placement of the detector was within ±0.5 mm from the actual BrachyVision calculation point. A minimum of two non-trending readings were taken for both detectors.

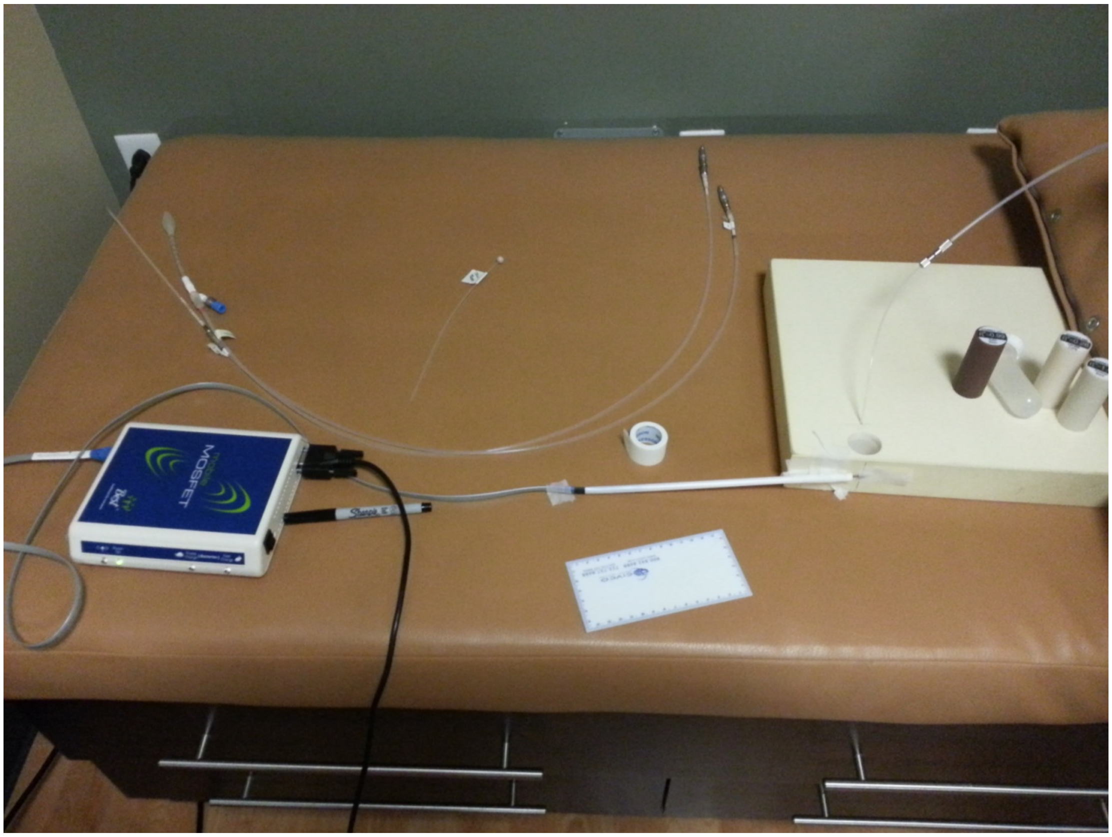

Figure 17. Picture of the QAP physical measurements showing the position of the MOSFET.

3.1.5. MC ^{192}Ir Scenario

The MC QAP phantom was designed to have similar dimensions to the calculated volume utilized inside BrachyVision. The MC QAP volume areas were defined as a 9x9x5 cm^3 water block with the ^{192}Ir source position at the center. The 9x9x5 cm^3 volume was a reasonable comparison as the scatter contribution from further distances would not contribute significantly. The volume at a radius of fifty centimeters and beyond was defined as a void with no importance to calculations. Inside this boundary and up to the QAP defined edges the volume was given the value of air with importance to track photon and electrons. Inside the QAP edges, the volume was set to a material of water with importance set to track photons and electrons. To mimic the density plug, a cylindrical volume was subtracted from the QAP and placed parallel to the axis of the ^{192}Ir source. This cylinder had dimensions of 5 cm in height with 3 cm in diameter and was given importance to track photons and electrons. The MC design for the ^{192}Ir GammaMed source was created from the dimensions and materials set forth in the ESTRO report from the High Energy Brachytherapy Source Dosimetry (HEBD) Working Group, "Dose Calculation for Photon-Emitting Brachytherapy Sources with Average Energy Higher than 50 keV: Full Report of the AAPM and ESTRO" (Perez-Calatayud, et al., 2012). On page 67 the source is shown with exact dimensions for the stainless steel capsule, the ^{192}Ir source, and the stainless steel mesh cable. The ^{192}Ir spectrum was then found from the National Nuclear Data Center as seen in Appendix A for the energy spectrum and abundance. A visualization of the ^{192}Ir source is shown in Figure 18.

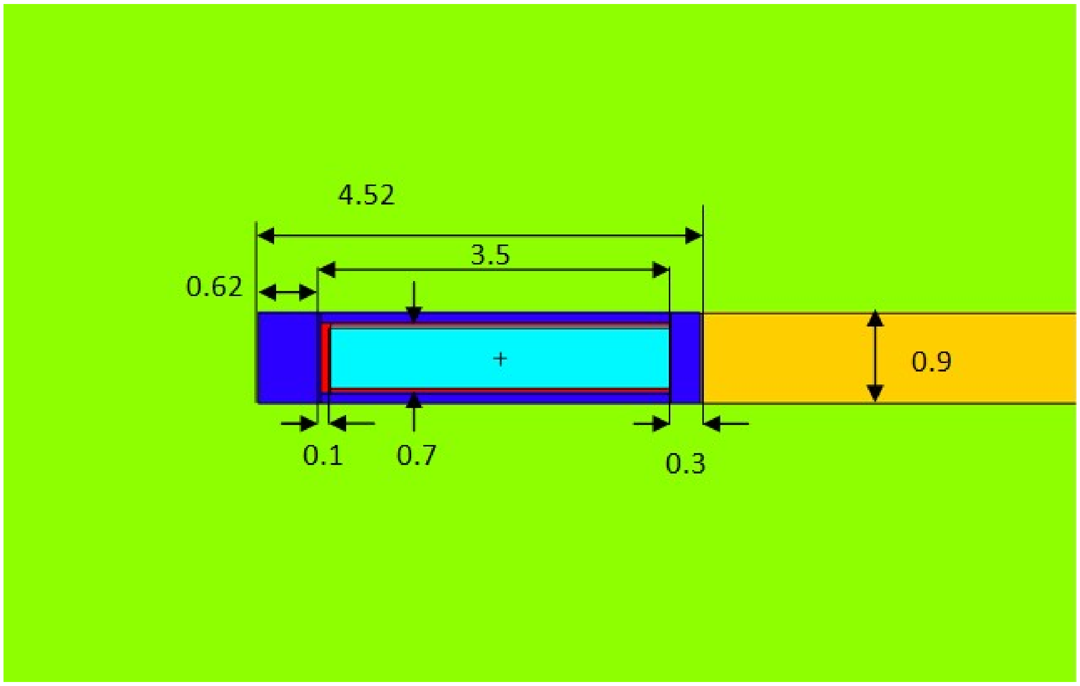

Figure 18. MCNP Visual Editor's GammaMedplus source modeled.

For a more complex comparison, it was decided to look at multiple points, or tallies. These points of interest, or tallies, were created within the boundaries of the MC QAP as spheres with radius of 0.05 cm to mimic point detectors. The calculation points started at seven millimeters from the source and continued incrementally at two millimeter steps until the edge of the phantom. All tallies were placed on a perpendicular bisector of the ^{192}Ir source and are visually shown in Figure 19. The placement was done intentionally such that these tally volumes would not sit on two boundaries except exiting the phantom. The exiting tally was placed intentionally to show correlation between the MOSFET and diode measurements to MC calculations.

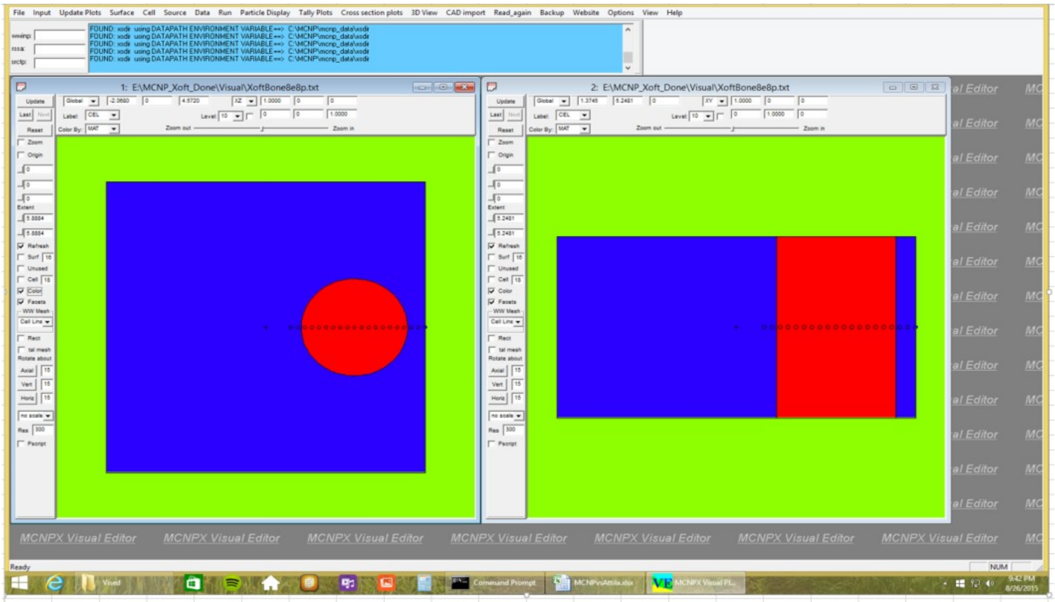

```
FOUND: xsdir  using DATAPATH ENVIRONMENT VARIABLE ==>  C:\MCNP\mcnp_data\xsdir
FOUND: xsdir  using DATAPATH ENVIRONMENT VARIABLE ==>  C:\MCNP\mcnp_data\xsdir
FOUND: xsdir  using DATAPATH ENVIRONMENT VARIABLE ==>  C:\MCNP\mcnp_data\xsdir
FOUND: xsdir  using DATAPATH ENVIRONMENT VARIABLE ==>  C:\MCNP\mcnp_data\xsdir
FOUND: xsdir  using DATAPATH ENVIRONMENT VARIABLE ==>  C:\MCNP\mcnp_data\xsdir
```

Figure 19. MCNP QAP design with calculation points.

The calculation point's volumes were used to score the F6 tallies. The results from the F6 tallies were then converted to Dose by the Equation 8.

Equation 8

$$D(cGy) = \ x\left(\frac{MeV}{g}\right)x1.602*10^{-6}\left(\frac{erg}{MeV}\right)*3.7*10^{10}\left(\frac{Bq}{Ci}\right)*\left(\frac{dis}{Bq*s}\right)*10Ci$$

$$*\ 2.354\left(\frac{particle}{dis}\right)*1.13\left(\frac{contained}{apparent}\right)*10^{-7}\left(\frac{joule}{erg}\right)$$

$$*\ \ 1000\left(\frac{g}{kg}\right)*\left(\frac{Gy*kg}{joule}\right)*Time\ (\text{sec.})$$

As suggested by TG 186, tests were performed to first confirm the accuracy of this projects ^{192}Ir source model. To facilitate this test, the outer volume sphere that appears as an air volume up to a radius of fifty centimeters was given a phantom material of water (1.0 g/cm^3). This was to simulate the BrachyVision's TG43 calculations which assumes all of the known area to be water equivalent, or essentially creating a semi-infinite phantom. The MC infinite phantom test had the tally points set to F6 and *F8 for comparisons. When using Acuros settings inside BrachyVision, a semi-infinite phantom was created with the GammaMed ^{192}Ir source placed at the center. The semi-infinite phantom material was set to water (1.0 g/cm^3).

The next MC test was to show how strongly the scattered dose contributes to these tally points as the phantom size is reduced. The MC F6 tallies results from using the QAP phantom surrounded by air were then compared to the MC F6 tallies from the semi-infinite phantom. The lack of lateral scatter and the contribution to points close to boundary edges was the primary reason for performing this test. The results from this test were to indicate the possible reduction in dose to the patient's skin-air boundary interface when Acuros was applied to previously treated patients.

The inhomogeneity test for this part of the research was accomplished by applying Acuros to all four scenarios within BrachyVision where the scans differed only by the cylinder plug. The four scenarios were solid water plug, cortical bone plug, lung plug and the cylinder left void to mimic air. BrachyVision was then allowed to use Acuros solver directly on these CT scans and the results were recorded as $D_{w,m}$.

The MC input file for this part of the research is shown in Appendix A. The cylinder material was modified four times to accommodate the scenarios of water, cortical bone, lung and air as was previously calculated with Acuros. It was necessary to use MC histories between $1x10^7$ to $1x10^9$ to lower the acceptable criteria for point sources in MC to relative errors less than 0.05. These results are displayed later as the $D_{w,m}$ figures when compared to Acuros results. To better understand the influence of reporting $D_{m,m}$ for ^{192}Ir energy spectrum, all four MC scenarios were recalculated with the tally points modified to be that of the material instead of water. These results are graphically compared in later figures.

3.2. Attila® Validation using a Low kV Spectrum

3.2.1. Attila

Attila software was used for the investigation of a low kV spectrum. The Xoft Axxent spectrum was chosen as the low kV source spectrum because it is FDA 510k approved for clinical HDR treatments in lieu of the ^{192}Ir source. As stated earlier, Attila software is the parent software to Acuros BV. Attila offers the user more flexibility when creating test scenarios since Acuros was a specific rewrite for Varian BrachyVision. As such, Attila requires a few steps to be performed before an actual dose calculation can be created. These steps are; phantom importation, mesh generation, importing the relevant cross section library for the energy level, create a source library, creating a base calculation, defining the materials with their respective weight fractions, defining how Attila will display the results by specifying either points and/or rings for recorded dose.

The phantom to be used in Attila was first created in a software program called Solidworks (Dassault Systèmes SOLIDWORKS Corp., Waltham, Massachusetts). Solidworks is a 3-D computer modeling drafting program. The original QAP at 30x30x5 cm^3 turned out to be too large to accommodate a fine mesh needed for accurate measurements when using a low kV spectrum. When imported, the mesh settings created a very coarse grid which subsequently led to rather larger than expected errors when compared to the MC results. Therefore, the QAP dimensions were reduced to 9x9x5 cm^3 block, with the origin placed at the box's geometric center. A cylinder cutting the box was centered at distance 2.5 cm lateral to origin, or coordinates (2.5, 0, 0) with a 3 cm diameter hole. The cut was then replaced with a cylinder of dimensions 3 cm diameter and 5 cm height as seen in the Figure 20. This phantom was then saved in Parasolid format and imported into Attila software. Inside Attila software, the phantom was then converted using Attila's automatic meshing module which calculated the optimum tetrahedra to cover the QAP areas. The mesh is required to facilitate the transport calculations on the phantom as seen by Figure 21. These tetrahedra discretize the volumetric space and further reduce the calculation time needed by reducing the number of calculation points. BrachyVision does a similar reduction by creating a grid across the image. At each grid point dose is calculated, and the dose between these points is interpolated.

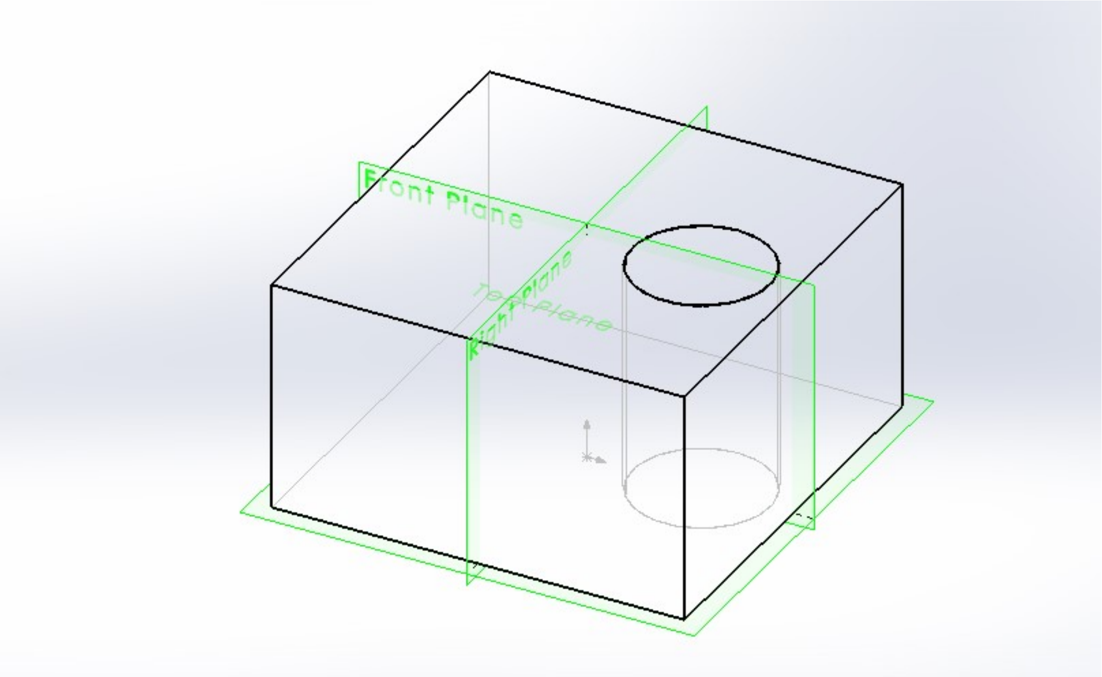

Figure 20. Solidworks Study Phantom

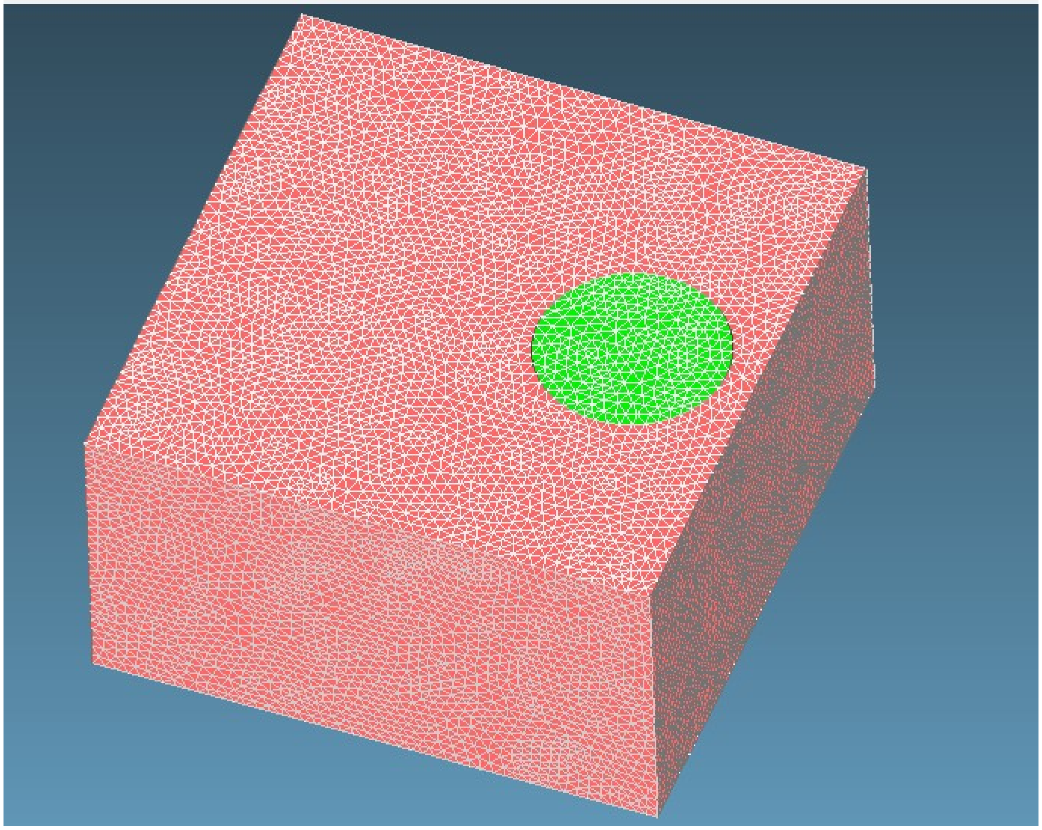

Figure 21. Attila Mesh applied to study phantom.

The cross-section files were generated by CEPXS. Once imported into Attila, these cross-sections are then available for grouping different energy ranges together or left as detailed steps. In this scenario each energy group was left as detailed beginning from 50 kV down to 6 kV with steps of 2.5 kV. The final two steps were setting up the source spectrum and choosing Attila's First Scattered Distributed Source Calculations, or FSDS.

The base calculation choices for Scattering Options and Default Angular Quadrature, were to set to 4 and 18, respectively. It should be noted that Attila offers the user several choices while Acuros is specifically set to one optimized Scattering Options and Default Angular Quadrature. Acuros settings were chosen to optimize between accuracy and speed. Obviously, the higher the settings made in Attila, the longer the calculation times.

Next, each material was given its associated physical density. As an example, water was set to 1.000 g/cm^3. The next screen allows the user to assign materials to volumetric areas. For these tests, the green area shown in Figure 21, was changed between water, cortical bone, air and lung whose material compositions were the same as used in the Acuros tests.

The last entries needed for Attila were assigning a point source, position in the phantom and the spectrum. The point source was given Attila phantom center coordinates of (0, 2.5, 0). The original spectrum for the Xoft, 50 kVp spectrum was extremely high resolution. It is shown in Figure 22, and was data collected by Dr. Michael Mitch using a Canberra GUL0110P Ge Spectrometer. In an effort to reduce the number of entries needed in Attila and MC, a more simplified spectrum was created by changing the step size to a coarser resolution. Each kV point was associated with the normalized abundance of that energy. A graph of the reduced graduated step size is shown in Figure 23.

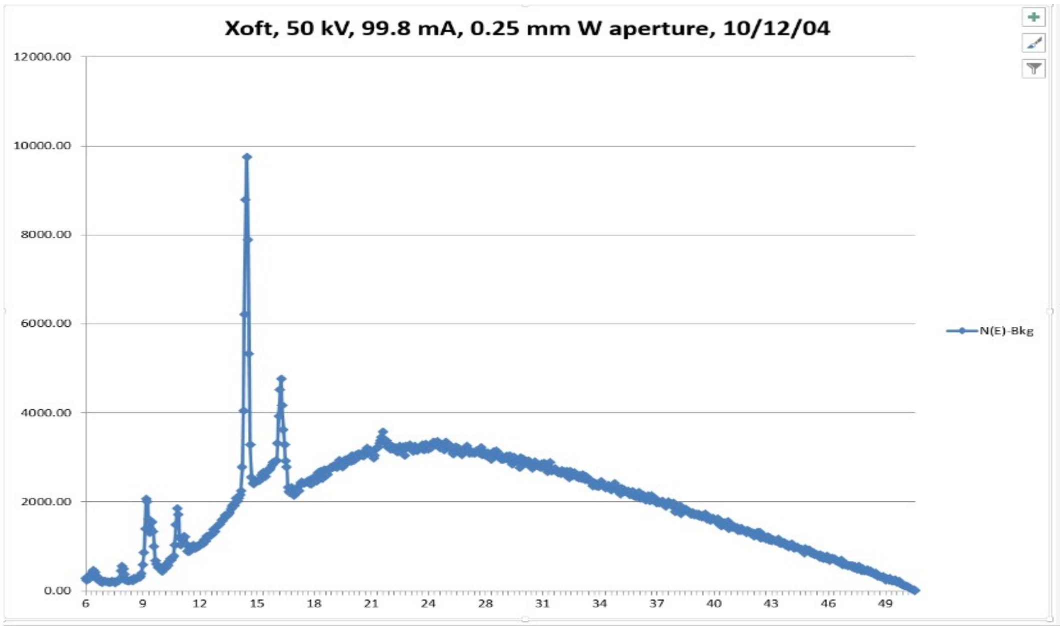

Figure 22. 50kV, Xoft Spectrum Courtesy of XOFT, a subsidiary of iCAD, Inc.

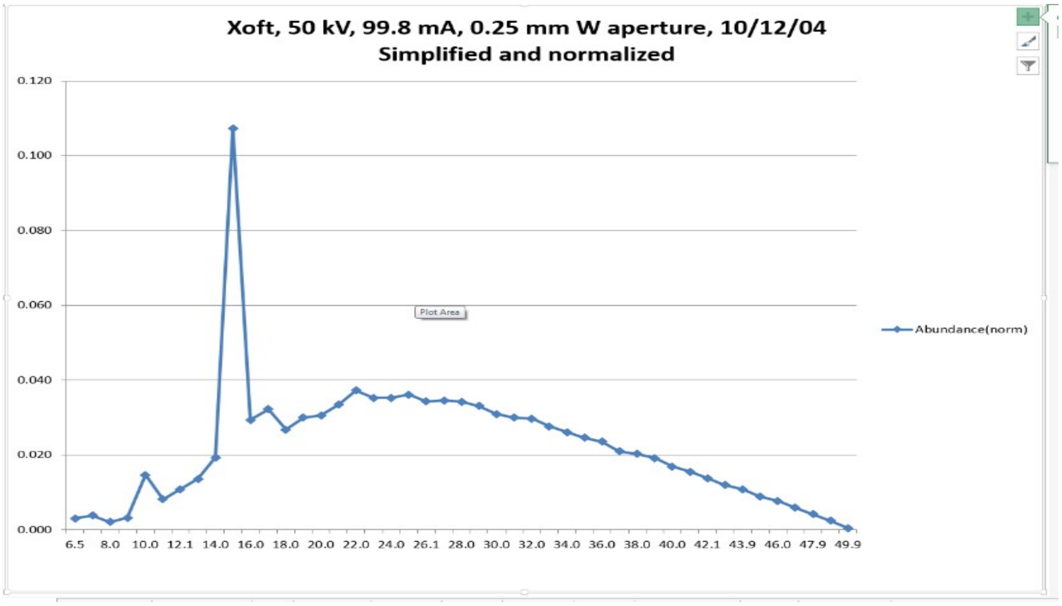

Figure 23. 50 kV reduced Xoft Spectrum for MCNP and Attila

3.2.2. MC Modeling of Xoft® Spectrum

As with the ^{192}Ir source investigation, a MC input file was created to simulate the same 9x9x5 cm^3 phantom. The source spectrum was recreated identical to the Attila source spectrum. The ^{192}Ir defined source with its dimensions was replaced by a single point source due to the design of the Xoft source was proprietary. Also, if a model of the Xoft would have been attempted, the MC design would need to attempt to simulate the cathode to anode reproduction of a miniature x-ray tube and its Bremsstrahlung. Each simulation was calculated with 2x10^9 histories which resulted in the relative error to be less than 2%. An F6 tally was used for each calculation point and the material was left as the composition of the points surrounding medium to record $D_{m,m}$. As a comparison each scenario was recalculated with each point's material changed to water to simulate $D_{w,m}$.

3.3.Patient Review with Acuros^{TM} BV

3.3.1. Patient Parameters

This part of the research expects that the commissioning of Acuros has already occurred. That Acuros calculations are within ±5% of MC calculations over clinically important distances chosen to start at one centimeter from a source to less than 4 cm distance. This range was chosen as SAVI applicators use dose calculations within one centimeter of a source and Contura or MammoSite applicators will begin their dose normalizations outside the balloon volumes. If the typical radius of a balloon is 2 cm, then the normalization distance is at 3 cm (1 cm distance from balloon edge).

An application was submitted to and approved by Oregon State University Institutional Review Board to perform a retrospective study of two hundred previously treated TG43 brachytherapy patients by recalculating the dose distributions using Acuros. All patients had been treated to a curative dose of 3400 cGy given 340 cGy/fraction for ten fractions as described by National Surgical Adjuvant Breast and Bowel Project (NSABP) and Radiation Therapy Oncology Group (RTOG) protocol of NSABP B-39 protocol, or B-39.

The primary aim of B-39 was to determine if APBI provides equivalent local tumor control when compared to WBI for early stage breast cancer. While there were many secondary aims of B-39, one important part of this study was to provide qualitative dosimetric data that shows the distribution of the brachytherapy dose and correlates to long term outcome. A second important aim was to compare acute and late toxicities between the radiation therapy regimens.

Data that was submitted to B-39 was chosen such that an accurate portrait of each patient's dose distribution would be recorded and compared to the outcomes of both disease and patient specific tissue reactions. For disease area coverage the B-39 investigation chose to record the volumes of planning target breast tissue (PTV_Eval) receiving 100% of the 34 Gy total ($V_{100\%}$). Another value was the volume of target covered by 90% of the 34 Gy ($V_{90\%}$), or 30.6 Gy. These values were important to allow investigators to later understand if local recurrences, counted as failures, appeared within this PTV_Eval were subjected to inferior dose coverage.

Two maximum dose constraints given by B-39, were the volume of tissue receiving 51 Gy and 68 Gy. Since fat necrosis was found by Wazer (Wazer, et al., 2001), to be related to the volume of breast tissue being irradiated, B-39 limited the maximum volume of breast tissue that could receive 51 Gy (150% of prescribed dose) and 68 Gy (200% of the prescribed dose) to 50 cm^3 and 10 cm^3, respectively. B-39 also set a limit for the maximum skin dose to $\leq$ 49.3 Gy at any point on the skin to avoid any possible acute or chronic skin reactions. According to Bray (Bray, et al., 2016), acute radiation dermatitis is the most common skin reactions following treatment. Cox (Cox, et al., 1995), shows the RTOG/EORTC skin scoring criteria for acute (1-4 weeks after treatment) and chronic, or late, skin reactions in Table 3. Cox wrote that chronic skin reactions are radiation induced skin reactions that are refusing to heal or can even be new complications arising from previously irradiated areas several months later. In some cases, radiation recall can occur due to concurrent chemotherapy. According to Bray (Bray, et al., 2016), radiation recall is an acute inflammatory reaction of the previously irradiated area of skin when the patient receives certain chemotherapy agents. Usually the reaction is greatest within the first few months following radiation treatment.

Table 3. Toxicity Criteria of the Radiation Therapy Oncology Group (RTOG) and the European Organization for Research and Treatment of Cancer (EORTC)

RTOG/EORTC Skin Scoring Criteria	
Score	ACUTE Skin
0	No change over baseline
1	Follicular, faint or dull erythema/epilation/dry desquamation/decreased sweating
2	Tender or bright erythema, patchy moist desquamation/moderate edema
3	Confluent, moist desquamation other than skin folds, pitting edema
4	Ulceration, hemorrhage, necrosis
	CHRONIC Skin
0	None
1	Slight atrophy, pigmentation change; some hair loss
2	Patch atrophy, moderate telangiectasia; total hair loss
3	Market atrophy; gross telangiectasia
4	Ulceration
5	Death Directly Related To

3.3.2. Patient Data Preparation

In preparation for using Acuros, each patient that received treatment with a Contura or MammoSite device had the balloon volume drawn in the TPS replaced with a macro density equivalent to 1.00 g/cm^3, or water. The TPS allows the user to modify a drawn structure by assigning any density or material provided it is within range of densities commissioned. The necessity to modify the balloon's volume began at the initial CT simulation. During the patient scan the saline solution contained inside the balloon is not discernible from the surrounding tissue. Therefore, a 1 cm^3 of non-ionic contrasting agent was injected into the balloon through a specially designed port that allows fluid to be entered into the balloon from outside the patient's body. While the contrast agent allows the user to clearly define the balloon edges from surrounding tissue, the CT will incorrectly assign a higher HU to this balloon volume and pass that information to BrachyVision and subsequently to Acuros. Based upon the density table, Acuros will assign a bone to this balloon volume, and erroneously use this higher density material, and subsequent mass-energy absorption coefficients, when calculating the photon transport.

The SAVI device does not require this modification to be performed. Although the SAVI does have metallic struts that lend support to the catheter tubes. These supports clearly show in the TPS as a dense material but are relatively tiny. For this research it was decided to leave these inhomogeneities present and allow Acuros to account for the material.

3.3.3. Patient Data Collection

Besides the collection of both TG43 and Acuros parameters from B-39. The patients' data were also graded for follow up toxicity levels as reported at two and twelve month follow up visits. The acute reactions were noted from the 2 month follow up notes and the chronic reactions were noted from the 6 month and one year follow up reports.

4. Results and Discussions

4.1. Measurements using ^{192}Ir

4.1.1. Diode and Mosfet measurements

An easily reproducible phantom was constructed to allow for physical Quality Assurance measurements. While the first design using water would have been ideal for consistency with other published papers, the use of solid water allowed for easy placement of the detector, the density plug and source position. Solid water also allowed for physical measurements at exact distances. Another benefit of using solid water was that the chance of getting the source wet was no longer an issue.

The diode and MOSFET measurements showed reproducible and relevant results that were consistently accurate. The measurements were taken over several months, which allowed the source to decay and subsequently, the dwell time to increase proportionately to accommodate the lowered source strength. As can be seen in Table 2, the results standard deviation (SD) were within 2%, while the dwell times varied by up to 29% change between the two most extreme cases of air and cortical bone plug to produce one Gray at the measurement point.

Table 4. Diode and Mosfet Measurements.

	Acuros™ BV						
	Time (sec)	Diode	SD	Ratio	Mosfet	SD	Ratio
Plug	For 100cGy	cGy	cGy	Measurement/ Acuros	cGy	cGy	Measurement/ Acuros
Water	177.5	102	2	1.02	100.6	2	1.01
Air	152.8	102	1	1.02	99.7	2	1.00
Ln300 (0.29g/cc)	158.7	100	1	1.00	99.7	2	1.00
Cortical Bone (1.9g/cc)	197.5	102	1	1.02	97.5	1	0.98

The diode and MOSFET measurements showed several conclusive results. One conclusion is that diodes and MOSFETs respond to the energy spectrum of ^{192}Ir brachytherapy source with almost an equivalent response. Another compelling result is that Acuros predicted the dwell times needed to give one Gray at the measurement point for all four scenarios. This meant that Acuros accurately calculated the photon transport through the different material compositions, took into account the lack of side scatter and finally the lack of backscatter. The accurate prediction of the lack of backscatter contributing to the dose measurement is especially made evident as neither the diode nor Mosfet had backscatter material behind them during data collection.

4.1.2. Acuros^{TM} BV and MC comparison using ^{192}Ir

The next comparison for Acuros was performed by creating a MC input deck file that mimicked the geometry of the QAP. The MC phantom was modeled with the same dimensions as the QAP and given the density of 1.052 g/cm^3 and material composition of water (88.8 % O, 11.1% H). The plug was delineated as a cylindrical volume to mimic the CTEDP plugs. The same four scenarios were then calculated in MCNP5 with 2x10^7 and greater histories which produced results with relative errors less than 3%. Unlike the single point measurement from the diode and Mosfet measurements, a series of perpendicular points were taken starting at seven millimeters from the source and continued to the edge of the phantom at an interval of every two millimeters. The step size was done intentionally so that no point would be positioned on the interface of water and plug adjacent edges.

TG186 recommends a full-scatter homogeneous phantom to be the initial test when investigating an MBDCA for the first time and compare to the TG43 data which has been extensively modeled. Likewise, comparing Acuros and TG43 results for ^{192}Ir under full-scatter would test the fabricated MC ^{192}Ir model's energy spectrum and design. The design directly affects the attenuated spectrum. This full-scatter MC setup was created by modifying the air surrounding the designed QAP to the material composition of water with density of 1.00 g/cm^3. This surrounding area had a diameter of 100 cm. For the ^{192}Ir source energy spectrum a sphere of water with this diameter size effectively created a semi-infinite phantom as suggested by TG186.

Two MC tallies, F6 (MeV/g) and *F8 (MeV), were chosen to compare against TG43 due to the easy conversion to dose as was shown in Equation 8. The *F8 tally was first modified by dividing by the volume of the collecting sphere. The results of F6, *F8 and Acuros for the semi-infinite phantom are shown in Table 5.

Table 5. Comparison of F6, *F8, Acuros and TG43 for ^{192}Ir On Semi-Infinite Phantom

Infinite Water Phantom of ^{192}Ir: F6, *F8, Acuros Normalized to TG43			
Distance (cm)	F6/TG43	*F8/TG43	Acuros/TG43
0.7	0.99	0.99	1.06
0.9	0.99	1.00	1.04
1.1	1.00	1.02	1.02
1.3	1.00	0.98	1.00
1.5	1.00	0.99	0.98
1.7	1.00	1.04	1.00
1.9	1.00	1.01	1.00
2.1	1.00	1.02	1.00
2.3	1.00	1.01	1.00
2.5	1.00	0.99	0.99
2.7	1.00	0.99	1.00
2.9	1.00	0.98	1.00
3.1	1.01	1.00	1.00
3.3	1.00	1.07	1.00
3.5	1.00	0.98	1.00
3.7	1.01	1.01	1.00
3.9	0.99	0.99	1.00
4.1	1.02	0.96	1.00
4.3	1.01	0.99	1.00
4.5	1.02	0.98	1.00

As can be seen by ratio of F6, *F8 and Acuros to TG43, the overall results are less than 2%. The decision to use F6 for the rest of the research was made after this test simply because F6 needed 2x10^{8} histories to produce less than 2% relative error at calculation point 4.5cm. The MC calculation time needed to produce this low relative error was 40.34 minutes. For the same MC input deck file with the tallies modified to *F8, histories of 5x10^{9} were needed to reduce relative error to just 3.6% at calculation point 4.5 cm. Due to the increased histories, the *F8 tally calculation time was 1984.43 minutes. As can be seen from Table 5, there was remarkably no difference in the results when normalized to TG43. In fact, the *F8 calculation had a repeating error at calculation point 3.3 cm of showing 7% greater than expected. This large deviation in dose could not be resolved and more than likely due to statistical noise.

Both MC tallies ratio to TG43 produced nearly identical results. This was not surprising since TG43 data was partly TLD and MC fabricated. Any differences would have derived from energy spectrum differences or mistakes in recreating the geometric design of the source. It is unclear why *F8 showed greater variability. Perhaps because *F8 sums both the photon and electrons transported. The F6 tally only sums the dose deposited from photons, which has been shown in literature to be acceptable for such low energy electrons. These low energy electrons are assumed to dump their energy at the point of creation thus causing immediate charged particle equilibrium (CPE).

For the Acuros to TG43 ratio, all calculation points at 1 cm distance and beyond were almost unity. The discrepancy of the first few points was more likely due to the primary photon contribution, as scatter would not be the dominating factor at these distances. This could be part of the trade-off of accuracy that Acuros solver deals with as the TG43 data for this distance was primarily generated by MC simulations as can be seen by the F6 and *F8 MC results at short distances from the ^{192}Ir source. Acuros is also held to the grid size given to it by BrachyVision and as such may need a finer spatial resolution to produce closer results to TG43.

The next scenario was to inspect the impact that reduced lateral phantom scatter would create as this would model the transition from TG43 infinite phantom assumption to an actual patient's limited body dimensions. The results are shown in Table 6. This experiment was accomplished by comparing the MC results of a reduced dimension (9 x 9 x 5 cm^3) water phantom that simulates the QAP used in the diode and Mosfet measurement phase of this research. When taking the absolute difference between finite and semi-infinite phantoms the results show a heavy reliance on the lack of lateral scatter which is accentuated as distance from the source increases. In fact, this experiment represents the expected results of the lack of scatter contribution from an actual patient's body dimensions, one would expect to see a difference between Acuros and TG43 dose at skin-air boundaries to be overestimated by TG43 up to 12.8%. Which would mean that if TG43 predicted 34 Gy on the skin-air edge, the actual dose would be 29.6 Gy. This inconsistency may adjust the threshold for skin reactions to a lower dose. This also shows the necessity of dose calculations to account for lateral and backscatter contributions at ever increasing distances and interfaces.

Table 6. MC Comparison of Finite and Infinite Phantom for ^{192}Ir

MCNP5 F6: Dose (cGy) of Finite Vs Infinite Water Phantom for 192Ir					
	Finite Phantom (9x9x5 cm^3)		Infinite Phantom		%
	F6 (cGy)	S.D. (cGy)	F6 (cGy)	S.D. (cGy)	Diff
0.7	4538.0	15.0	4550.0	15.0	-0.3%
0.9	2762.0	11.6	2773.5	11.6	-0.4%
1.1	1862.5	9.5	1875.0	9.6	-0.7%
1.3	1337.9	8.0	1350.2	8.1	-0.9%
1.5	1005.3	6.9	1017.4	7.0	-1.2%
1.7	775.1	6.1	787.5	6.1	-1.6%
1.9	621.1	5.5	633.9	5.5	-2.0%
2.1	504.1	4.9	517.0	4.9	-2.5%
2.3	419.2	4.4	431.7	4.5	-2.9%
2.5	354.3	4.1	366.9	4.1	-3.4%
2.7	301.3	3.8	313.2	3.8	-3.8%
2.9	259.8	3.5	272.6	3.5	-4.7%
3.1	227.4	3.3	240.5	3.3	-5.5%
3.3	196.8	3.0	209.2	3.1	-5.9%
3.5	173.0	2.8	186.8	2.9	-7.4%
3.7	154.4	2.7	167.6	2.7	-7.9%
3.9	135.8	2.5	148.6	2.5	-8.7%
4.1	124.2	2.4	137.6	2.4	-9.7%
4.3	110.5	2.3	123.7	2.3	-10.6%
4.5	99.4	2.1	114.0	2.2	-12.8%

The next step in validating was to apply Acuros to controlled scenarios that introduced specific materials with known densities. These scenarios would be duplicated in MC and the same multiple points of interest would then be compared. The following figures show graphical representation of Acuros and MC results for each of the four density plug scenarios described earlier in the paper. Each point was connected to show the exponentially reducing nature of the plot.

The MC simulation used three patient applicable densities of lung, water and cortical bone. Air was also chosen due to the extreme differences in density seen at skin-air boundaries. All of these materials and their compositions with densities are listed in Table 7.

Table 7. Material Compositions

Material	Atomic Composition (ICRU44)	Density (g/cm^3)
Water	88.81% O, 11.19% H	1.00
Cortical Bone	3.4% H, 15.5% C, 4.2% N, 43.5% O, 0.1% Na, 0.2% Mg, 10.3% P, 0.3% S, 22.5% Ca	1.69 to 1.823
Lung	10.3% H, 10.5% C, 3.1% N, 74.9% O, 0.3% Na, 0.2% P, 0.3% S, 0.3% Cl, 0.2% K	0.3
Air	0.0124% C, 75.53% N, 23.18% O, 1.28% Ar	0.001205

The initial comparison shown in Figure 24 was using the solid water plug (1.000 g/cm^3) which showed good agreement. Since the Acuros calculated the dose distributions based upon the HU BrachyVision determined in each voxel, it was decided to show MC $D_{w,m}$ and $D_{m,m}$ even for the solid water experiment. Normally, $D_{w,m}$ and $D_{m,m}$ would be more relevant for materials whose composition differed from water and subsequently the mass-absorption coefficients would possibly drive the differences seen between $D_{w,m}$ and $D_{m,m}$ for a given scenario. Inside BrachyVision, the average material density measured gave a HU that correlated to a density 1.06 g/cm^3. For the MC simulation of $D_{w,m}$ each calculation voxel was given a value of 1.000 g/cm^3, while for Dm,m each calculation point density was left as 1.06 g/cm^3. This was not expected to show any significant differences in the results, but was performed to cover any possible questions when comparing Acuros, $Dw_{,m}$ and $D_{m,m}$.

The noticeable difference between Acuros and MC at the points close to the source probably stem from the differences in the primary fluence. This fluence can be affected by the design of the source housing and the actual source spectrum differences. Another possible difference is that the MC calculation points are not exactly without dimension. As stated earlier, the MC tally points do have a finite volume of 5.236x10^{-4} cm^3, while Acuros is limited to the resolution of the calculation grid that BrachyVision gives to it.

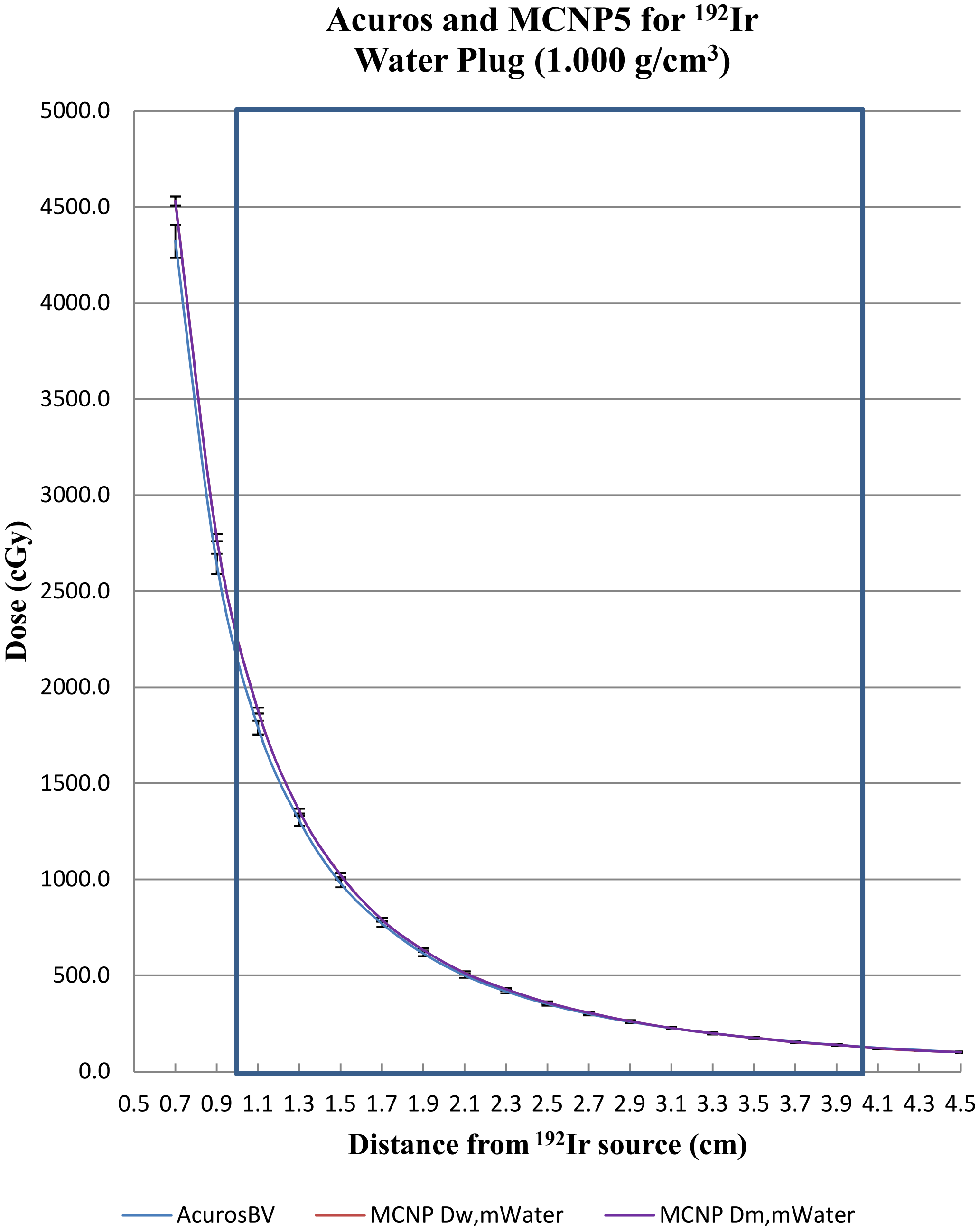

Figure 24. Acuros™ BV and MCNP5 water plug comparison with ^{192}Ir on QAP.

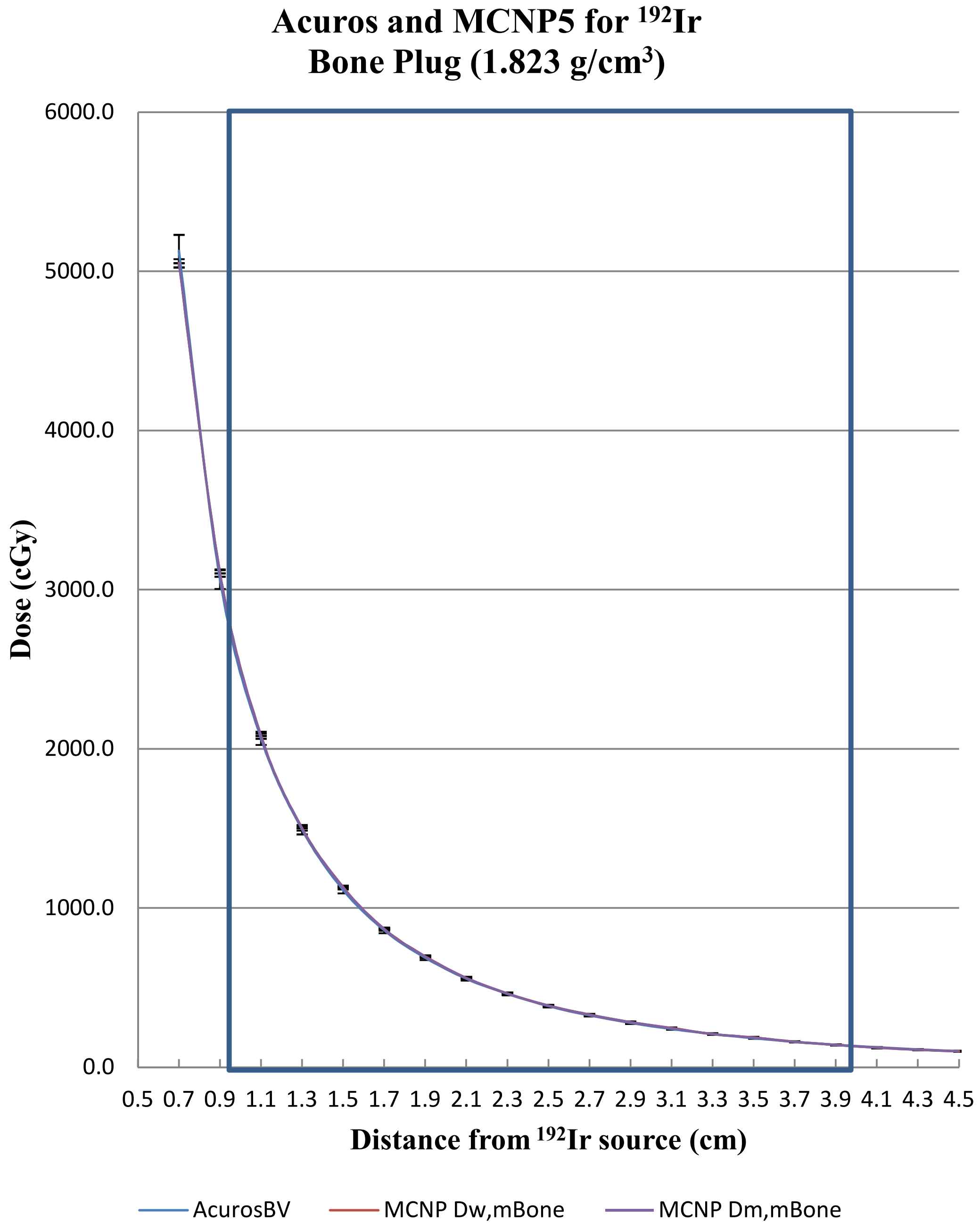

Figure 25. Acuros™ BV and MCNP5 cortical bone plug comparison with ^{192}Ir.

In Figure 25, the setup used a cortical bone plug of 1.69 g/cm^3 electron density. The results of Acuros showed good agreement to both $D_{w,m}$ and $D_{m,m}$. The dose reporting for MC's $D_{w,m}$ and $D_{m,m}$ were surprising at how close the two were. It was anticipated that $D_{w,m}$ and $D_{m,m}$ should show different results simply due to the differences in material composition. At the energy level from ^{192}Ir, the lateral scatter appears to be strong enough to compensate for the small volume of water in the $D_{w,m}$ scenario and the differences were negligible.

In Figure 26, the μ_{en}/p ratios of the material to water are shown for all three scenarios tested in this research. The mass-energy coefficients data was taken from Hubble and Seltzer website for NIST Physical Measurement Laboratory last updated July 2004. Reviewing the table of ratios, it was expected that the $D_{w,m}$ and $D_{m,m}$ calculations for ^{192}Ir would have showed some differences for the cortical bone tests. While the ^{192}Ir energy spectrum weighs heavily towards photon energy greater than 0.2 MeV, Figure 26 shows that the low energy test of eBx spectrum may show dramatic dose differences between $D_{w,m}$ and $D_{m,m}$.

The mass-energy absorption coefficients at the average x-ray energy of 0.35 MeV for ^{192}Ir appears to be high enough to avoid the dramatic difference in coefficients between cortical bone and water. The ratio of μ_{en}/p equal to 6.8 for cortical bone to water at 0.030 keV and then returns to almost unity above 0.2 MeV photon energy as can be seen in Figure 26. This may also account for the lack of difference seen in Figure 25 between $D_{w,m}$ and $D_{m,m}$.

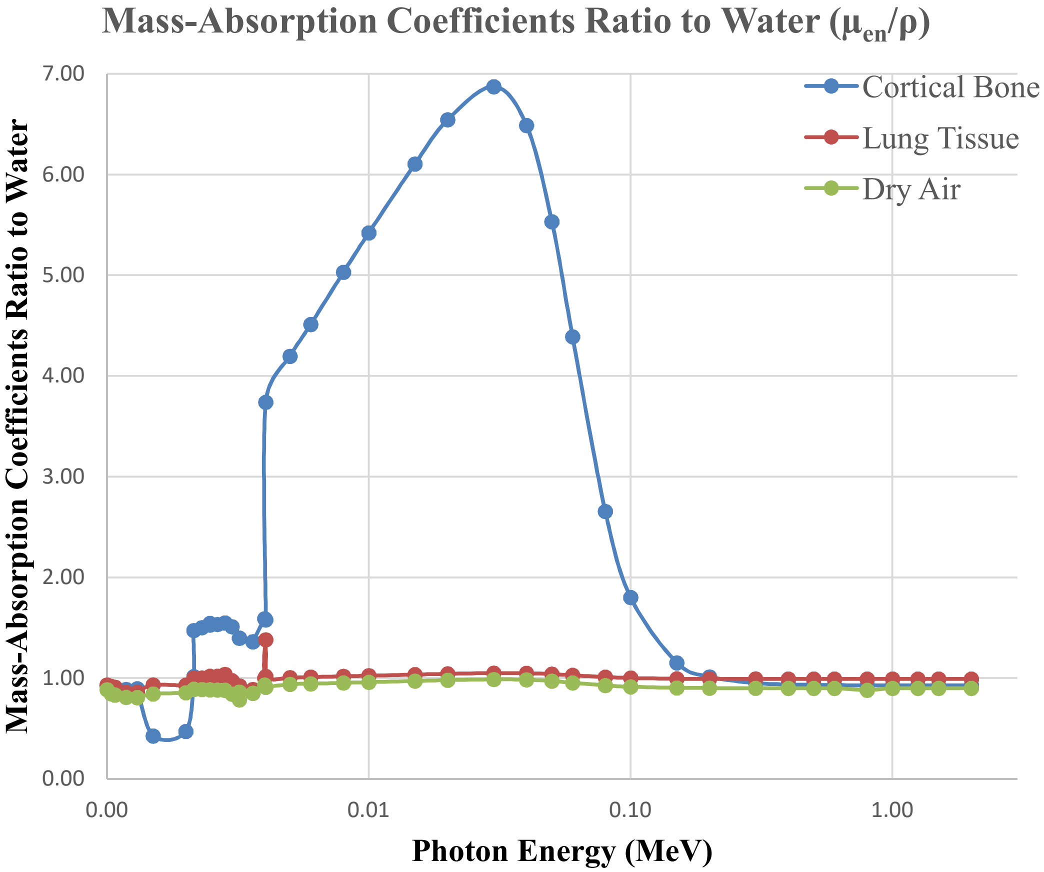

Figure 26. Mass-Absorption Coefficients Normalized to Water

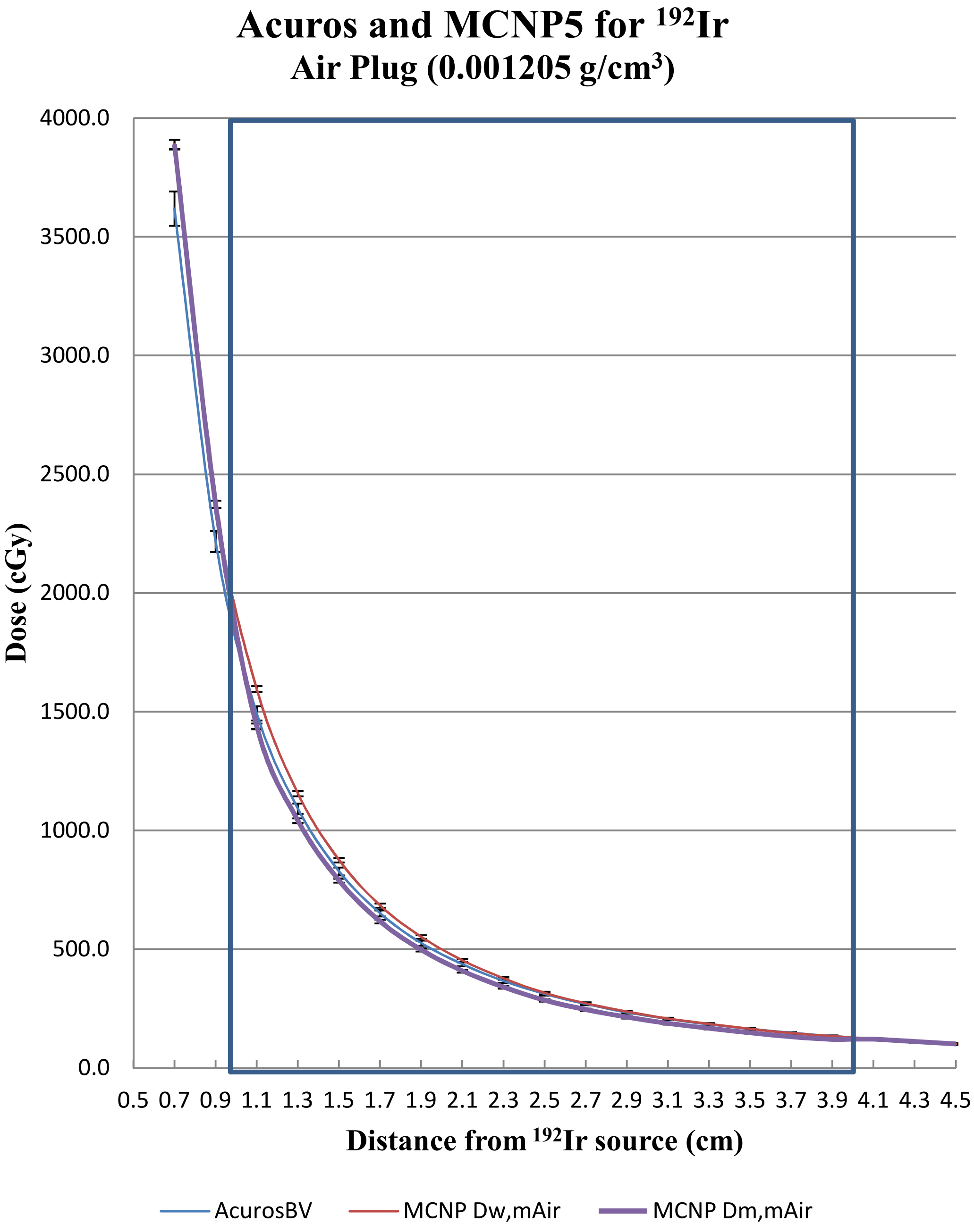

Figure 27. Acuros™ BV and MCNP5 air plug comparison with 192Ir.

The results of the air plug, or the cylinder volume with no plug, are shown in Figure 27. The calculation point at 0.7 cm showed the greatest discrepancy between Acuros and MC out of all four tests. It was expected that Acuros will show differences at shallow depths where the primary fluence is the greatest contribution as seen from the earlier semi-infinite phantom test. Another possible contribution to the differences seen in Figure 27 may be due to the lack of backscatter starting at 1 cm distance from the source. Acuros results were actually surrounded by the $D_{w,m}$ and $D_{m,m}$. The $D_{w,m}$ results showed a greater dose deposition than $D_{m,m}$. This was expected as the water filled tally points for $D_{w,m}$ would provide denser medium resulting in greater dose being deposited.

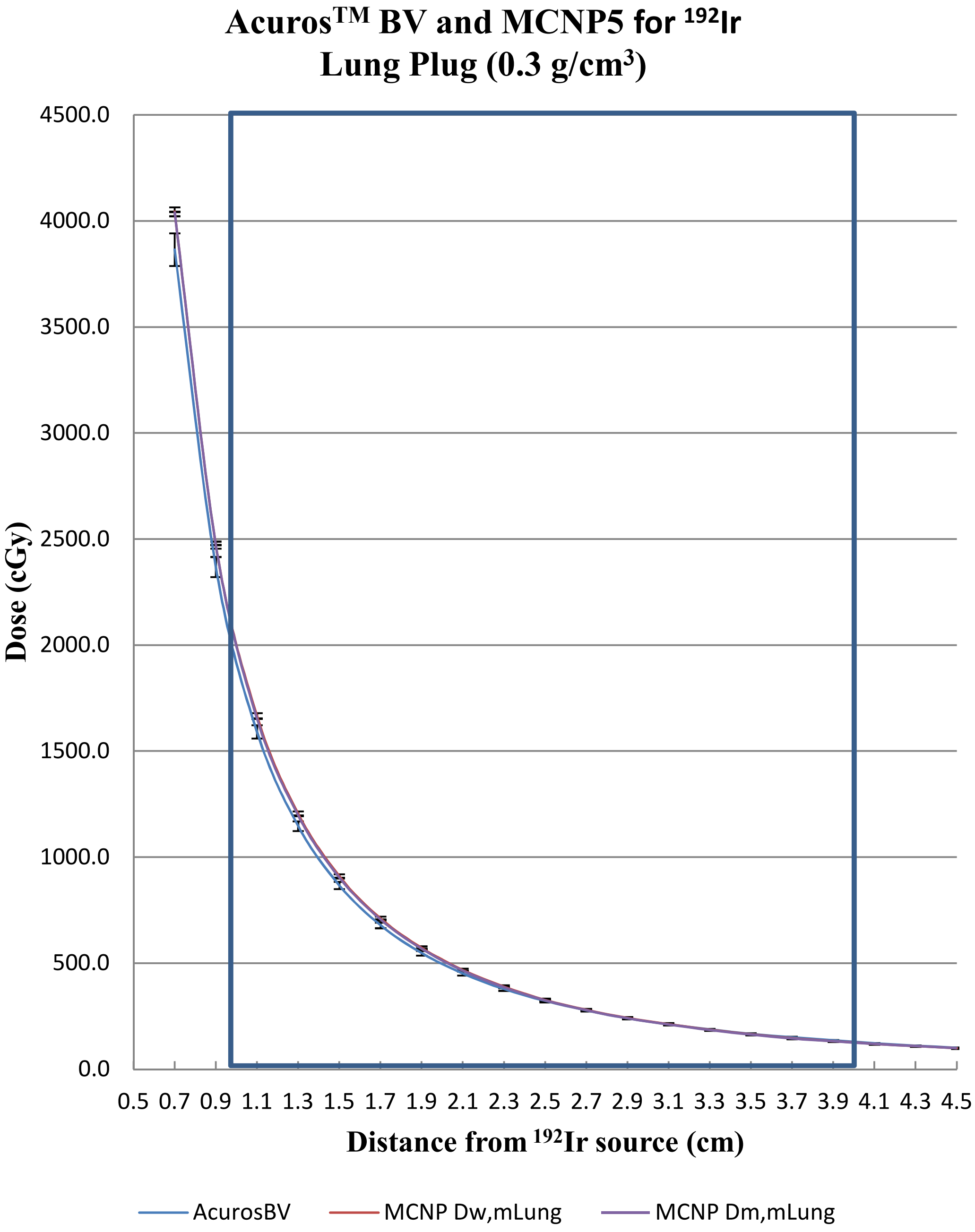

Figure 28. Acuros™ BV and MCNP5 Lung plug comparison with 192Ir

The lung material (ρ=0.3 g/cm^3) showed good agreement between Acuros, $D_{w,m}$ and $D_{m,m}$. As the lung to water mass-energy absorption coefficients ratio suggest, $D_{w,m}$ and $D_{m,m}$ are practically identical. Acuros results showed excellent agreement to MC especially dealing with the transitions to a less dense material. Out of all four tests, Acuros showed the greatest under-dose for lung plug right before the second transition between the lung to water interface.

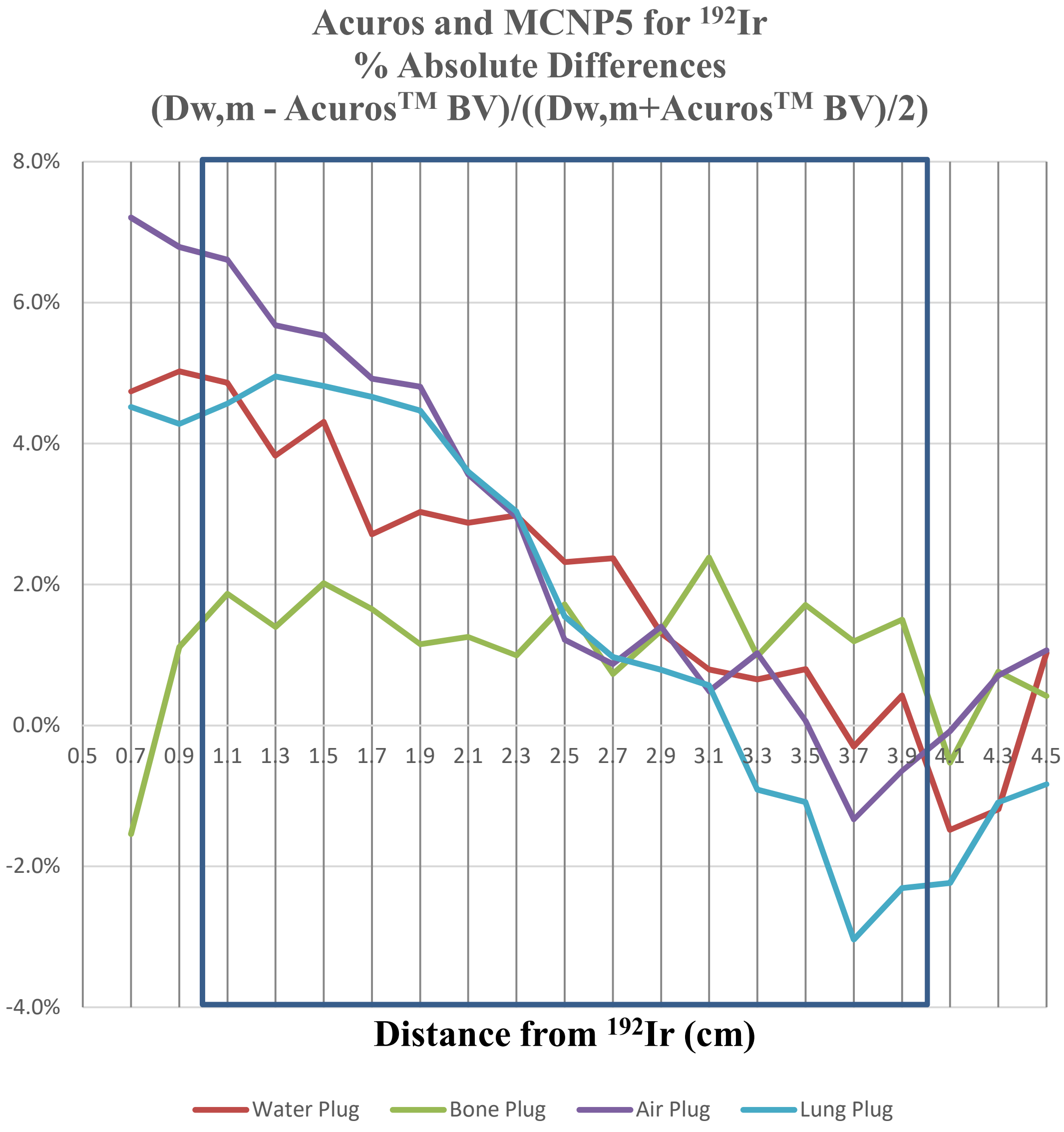

Figure 29. Acuros™ BV and MCNP5 absolute differences with 192Ir.

The absolute difference between all $D_{w,m}$ and Acuros scenarios are shown in Figure 29. Half of the water, air and lung calculation points for $D_{w,m}$ were 2% greater than Acuros. These greater $D_{w,m}$ points were all closest to the source. This could indicate that this research MC photon spectrum and source design may differ from Acuros, since the primary fluence would dominate dose contribution at these close distances. Although, the spatial dose calculation from BrachyVision may play a large part in the differences this close to the source.

Another observation is that the Acuros calculations now include noise associated to the CT and TPS estimation of voxel density. When Acuros dose response was normalized to TG43 in a uniform semi-infinite water sphere (1.0 g/cm^3), Acuros overestimated the dose by up to 6%, 4% and 2% at points 0.7, 0.9 and 1.9 cm, respectively. When reviewing the dose differences in Figure 29, Acuros overestimates the dose at close distances for water, lung and air, while underestimating the dose for bone. Although, the estimation of dose for bone at 0.7 cm is no longer 6% higher but now lower by 1.5%. This discrepancy is probably attributable to the average voxel density supplied to BrachyVision from the CT. This voxel data is again averaged when BrachyVision applies its calculation grid and this new voxel density is supplied to Acuros. At the 0.7 cm point, BrachyVision voxel density must be significantly less dense for air, lung and water because Acuros underestimated the dose compared to MC. The bone scenario at 0.7 cm calculation point voxel density follows this logic as Acuros overestimation of dose is reduced significantly lower than earlier calculated in the semi-infinite phantom.

Leading up to point 3.7 cm calculation point, all tests with density of 1.0 g/cm^3 or less show an ever decreasing underestimation of dose by Acuros when compared to MC. At 3.7 cm and beyond, the lung and air tests start to show trend towards unity between Acuros and MC. Once again this may be the voxel averaging causing the apparent density of the voxels closest to the edges to become denser. The results of the bone plug test were close to showing the smallest difference in results between MC and Acuros. Almost all bone calculation points were within ±2%.

4.2. Low kV Analysis with Attila and MC

The next validation was a comparison of a low energy spectrum that would force the MBDCA to primarily use photoelectric interactions. Attila was chosen as it has the versatility to transport low energy kV photon spectrum. Attila is not FDA 510k approved for patient use as of yet, so this comparison was created on a volumetric phantom similar to part one of this investigation. All tallies are left as Kerma (MeV/g) and as such will be described as dose.

A 3D modeling software named Solidworks was utilized to fabricate the rectangular box and an area off center defined as a cylinder with the same dimensions as the CTEDP plugs. This box was then exported into Attila. Once imported into Attila a finite mesh of tetrahedral areas was applied to the entire volume of the box. which is Attila's method for discretizing space. By converting the box into discrete tetrahedral volumes, Attila reduces calculation times by reducing the number of calculation points. Due to the low energy photons being transported across the box, the dose was inconsistently changing by every millimeter. So to increase the detail of the calculation points the meshing needed to be reduced to a very fine resolution, which was accomplished by maintaining the same number of mesh points but reducing the size of the phantom. For simplicity, the Attila phantom will also be called the QAP.

The Axxent Xoft source with maximum operating energy of 50 kVp was chosen as the spectrum to examine. This would simulate a commercially available therapeutic xray source. The source spectrum was collected by Dr. Michael Mitch, and made available from Dr. Thomas Rusch, Xoft co-founder. The detailed energy spectrum contained an extensive amount of points and proved to be difficult to enter by hand. Therefore, the spectrum was reduced by increasing the step size into larger bins and the probabilities were renormalized. This spectrum was then entered into both Attila and MC. Xoft's energy spectrum was the only modeled part of this experiment, it is not within this investigation to model the actual x-ray tube. Although, it is this author's belief that Attila would be able to appropriately model the Xoft source.

As with ^{192}Ir comparison and Acuros, Attila calculated the KERMA/history results at multiple points adjacent to the low kV point source. The first point began at seven millimeters from the source and then stepped at intervals of two millimeters until the edge of the phantom. The cylinder's edge began one centimeter from the source and continued for three centimeters. Beyond the plug was another half centimeter of phantom. The entire phantom, except the cylinder, was assigned 1.0 g/cm^3 density and material properties of water.

The initial comparison was performed identical to the ^{192}Ir. The eBx source was placed at the center of a semi-infinite phantom. The MC file was modified from a smaller 9x9x5 cm^3 phantom by changing the surrounding air to a material composition of water and giving it the density of 1.00 g/cm^3. A duplicate number of histories of 5x10^8 were used. The F6 tally results were kept as MeV/g/history and compared by normalizing the finite phantom results to the semi-infinite phantom results.

As expected, the finite phantom shows the effects of loss and scatter as the distance increases from the source. When comparing the dose differences at each calculation point calculation point for ^{192}Ir and eBx, both scenarios show an almost steady decrease in dose up to the 3.3 cm calculation point distance. From 3.3 cm to 4.5 cm, the eBx dose reduction increases by almost twice the amount lost as shown by ^{192}Ir. This was unexpected, since it was expected that the eBx would be reliant upon the primary flux and that scatter would not contribute as greatly at increased distances.

Table 8. Comparison of Finite and Semi-Infinite Phantom for Low kV Energy

MCNP5 F6: KERMA (MeV/g) of Finite Vs Infinite Water Phantom for eBx					
	F6 (MeV/g/history)				%
	Phantom (9x9x5 cm^3)	S.D	Infinite	S.D	Diff
0.7	9.56E-04	1.72E-06	9.57E-04	1.72E-06	-0.1%
0.9	5.20E-04	1.25E-06	5.21E-04	1.25E-06	-0.2%
1.1	3.15E-04	9.46E-07	3.17E-04	9.19E-07	-0.4%
1.3	2.06E-04	7.21E-07	2.07E-04	7.26E-07	-0.6%
1.5	1.43E-04	5.87E-07	1.44E-04	5.92E-07	-0.8%
1.7	1.03E-04	4.86E-07	1.05E-04	4.92E-07	-1.2%
1.9	7.65E-05	4.13E-07	7.77E-05	4.12E-07	-1.5%
2.1	5.84E-05	3.50E-07	5.97E-05	3.52E-07	-2.1%
2.3	4.57E-05	3.02E-07	4.69E-05	3.05E-07	-2.5%
2.5	3.62E-05	2.64E-07	3.74E-05	2.69E-07	-3.2%
2.7	2.88E-05	2.33E-07	2.99E-05	2.36E-07	-3.8%
2.9	2.39E-05	2.10E-07	2.49E-05	2.14E-07	-4.2%
3.1	1.99E-05	1.89E-07	2.10E-05	1.93E-07	-5.3%
3.3	1.64E-05	1.69E-07	1.75E-05	1.75E-07	-6.5%
3.5	1.34E-05	1.52E-07	1.46E-05	1.58E-07	-8.2%
3.7	1.14E-05	1.38E-07	1.25E-05	1.44E-07	-9.0%
3.9	9.59E-06	1.26E-07	1.09E-05	1.34E-07	-11.8%
4.1	8.01E-06	1.14E-07	9.24E-06	1.22E-07	-13.3%
4.3	6.75E-06	1.04E-07	8.16E-06	1.14E-07	-17.2%
4.5	5.56E-06	9.23E-08	7.05E-06	1.30E-07	-21.2%

The first test was using Attila and MC to simulate the eBx low energy transport when applied to the QAP. The plug was assigned to the material of water with density of 1.00 g/cm^3. The MC results were calculated using 5×10^8 histories. The results of the MC F6 and Attila output are graphed in Figure 30. Since both MC and Attila were given the identical energy spectrum, it is not surprising that the results have an average percent difference of -0.1% and a maximum difference of ±2.8%. These results show that Attila's assumptions when discretizing energy and space did not detract from the accuracy of the results when compared to MC.

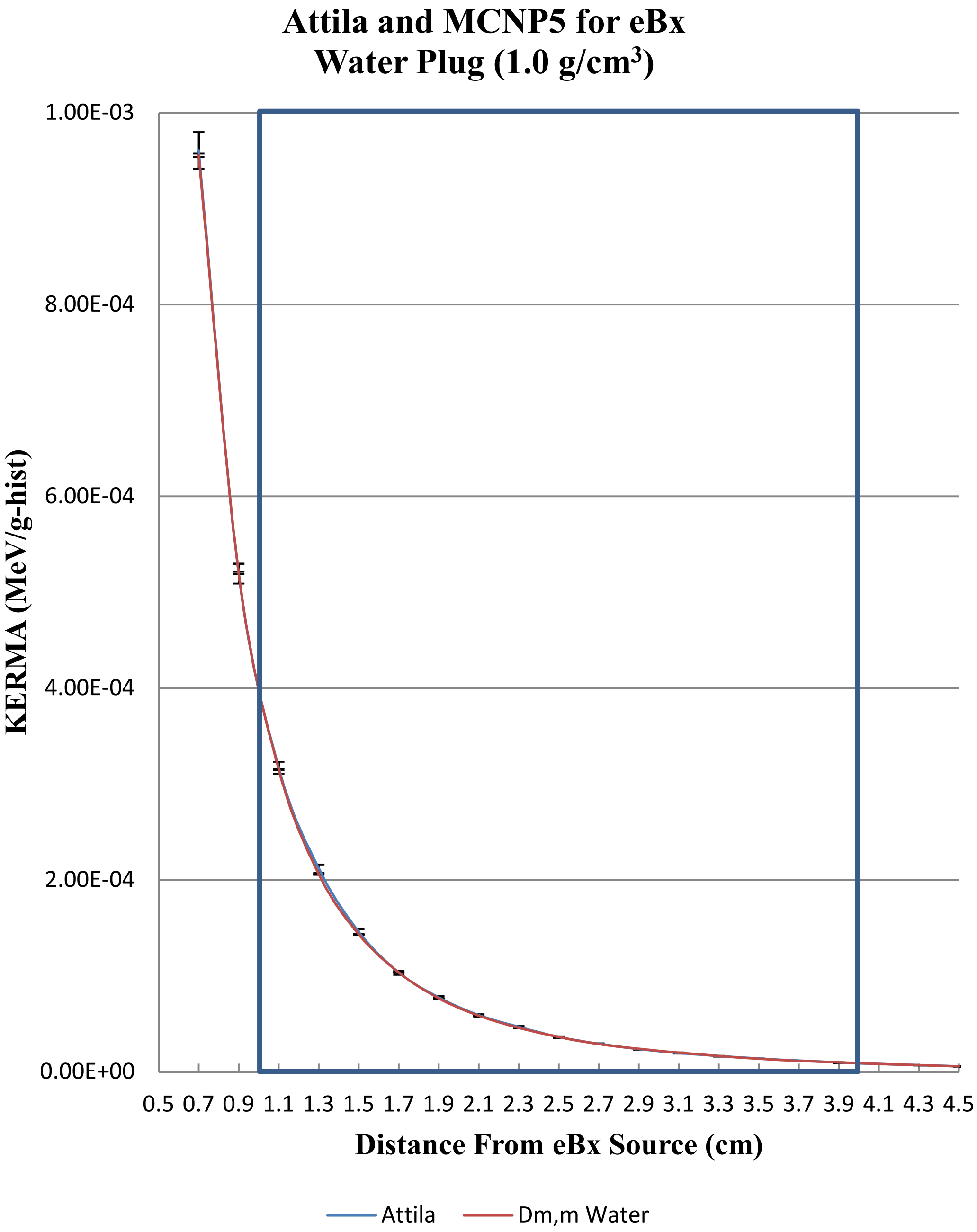

Figure 30. Attila and MCNP5 water plug comparison with low kV spectrum.

The second test the plug was given the material composition of bone with density of 1.69 g/cm^3. The MC results were calculated using 5×10^8 histories. The results of the MC F6 and Attila output are graphed in Figure 31. The average difference of the MC and the Attila for the bone plug was -5.5% and a maximum difference of 0.3% and a minimum of -15.1%. The Kerma$_{m,m}$ results leading up to the water-bone interface show a relatively high agreement with less than a 0.5% difference. The results for both MC and Attila into the bone plug both show a dramatic increase at the interface. For comparison, the Kerma$_{w,m}$ (Kerma reported to water but transported in medium) was calculated at each point. If the Kerma$_{w.m}$ results were chosen to be displayed by the user from the TPS instead of the Kerma$_{m,m}$, the discrepancy would be 147.2% difference or a Dm,m/Dw,m greater than 5.5 times difference in Kerma. This reporting difference at the water-bone interface would certainly produce necrosis of tissue at this distance from the source if the TPS dose reporting was chosen to be dose to water instead of medium. This further supports the idea that the TG43 reporting of all surrounding medium as water would substantially underestimate the actual dose if bone was within close proximity to a low energy source.

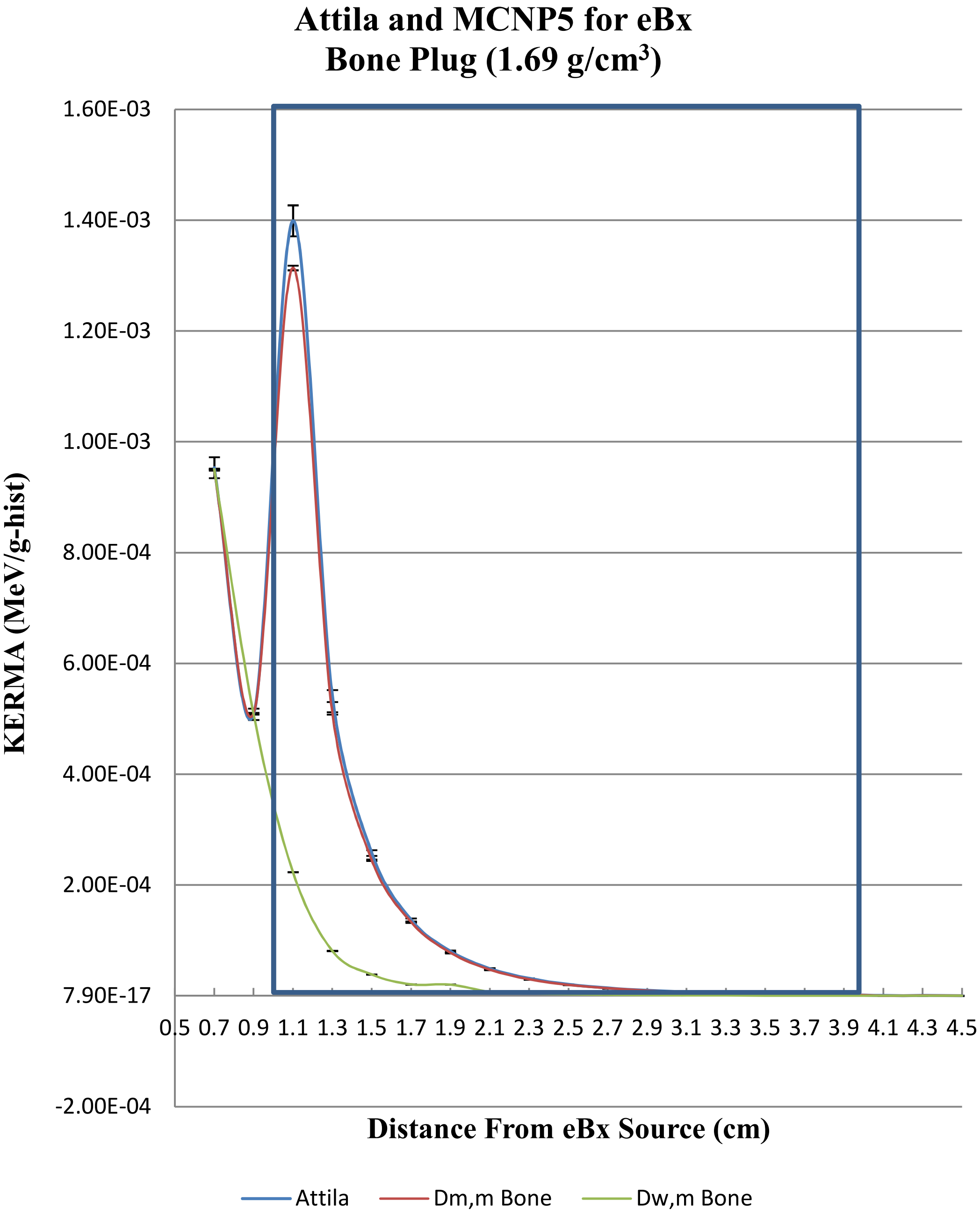

Figure 31. Attila and MCNP5 bone plug comparison with low kV spectrum.

The MC Visual Editor was utilized to show the display of the secondary buildup of Kerma at the water-bone interface. The MC bone plug file was loaded into the Visual Editor and 1x10^5 particle histories were calculated. This increase in Kerma at the interface shows the explicit effect from the low energy peaks in the mass-energy absorption coefficient for bone.

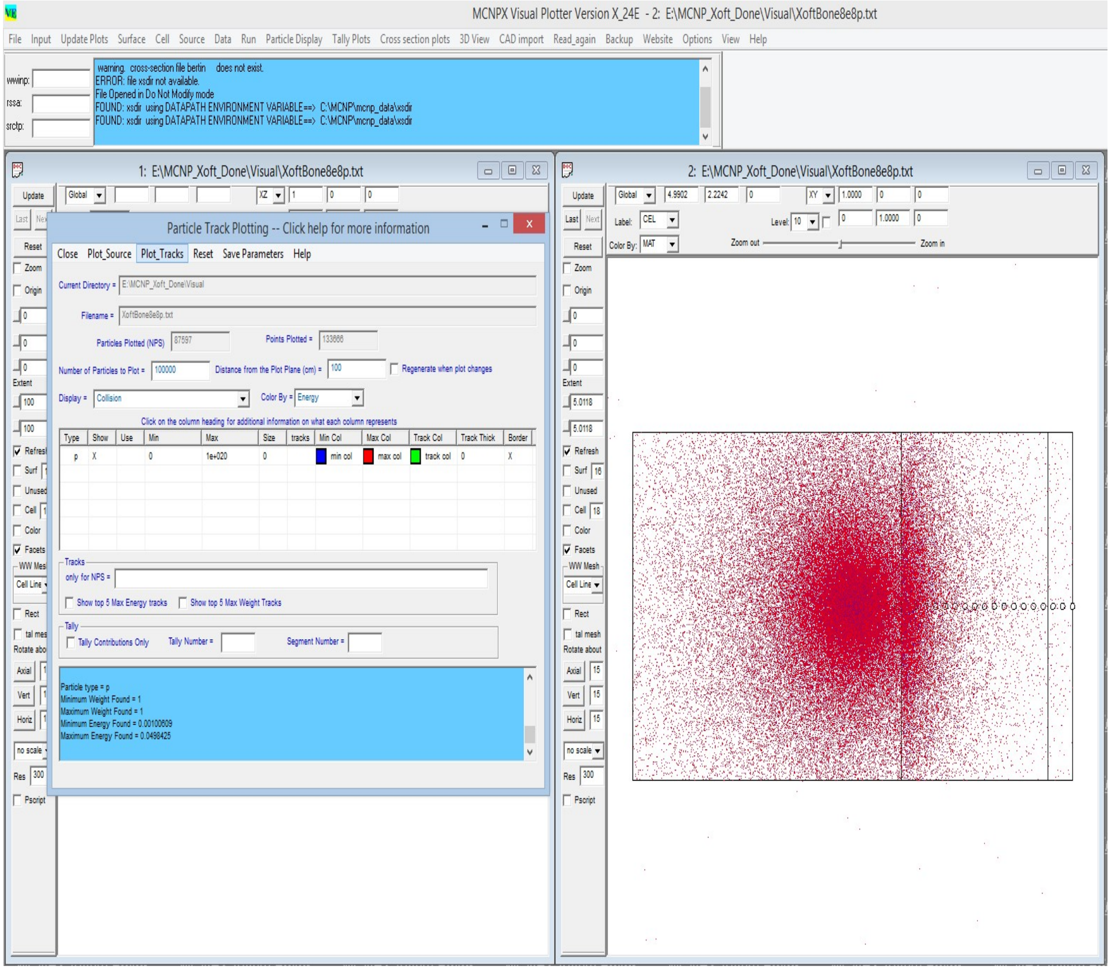

```
warning.  cross-section file bertin     does not exist.
ERROR: file xsdir not available.
File Opened in Do Not Modify mode
FOUND: xsdir  using DATAPATH ENVIRONMENT VARIABLE==>  C:\MCNP\mcnp_data\xsdir
FOUND: xsdir  using DATAPATH ENVIRONMENT VARIABLE==>  C:\MCNP\mcnp_data\xsdir
```

Current Directory = E:\MCNP_Xoft_Done\Visual
Filename = XoftBone8e8p.txt
Particles Plotted (NPS) 87597
Points Plotted = 133666
Number of Particles to Plot = 100000
Distance from the Plot Plane (cm) = 100
☐ Regenerate when plot changes
Display = Collision
Color By = Energy

Click on the column heading for additional information on what each column represents

Type	Show	Use	Min	Max	Size	tracks	Min Col	Max Col	Track Col	Track Thick	Border
p	X		0	1e+020	0		🟦 min col	🟥 max col	🟩 track col	0	X

Tracks
only for NPS =
☐ Show top 5 Max Energy tracks ☐ Show top 5 Max Weight Tracks

Tally
☐ Tally Contributions Only
Tally Number =
Segment Number =

```
Particle type = p
Minimum Weight Found = 1
Maximum Weight Found = 1
Minimum Energy Found = 0.00100609
Maximum Energy Found = 0.0498425
```

Global 4.9902 2.2242 0 XY 1.0000 0 0
Label: CEL
Level: 10
Color By: MAT

Figure 32. Soft X-ray buildup at tissue-bone interface calculated by MC Visual Editor.

The third test the plug was given the material composition of air with density of 0.001205 g/cm^3. The MC results were calculated using 5x10^8 histories. The results of the MC F6 and Attila outputs are graphed in Figure 32. The average difference of the MC and the Attila for the air plug was 4.4% and a maximum difference of 8.9% and a minimum of -1.4%. The Kerma$_{m,m}$ results leading up to the water-air interface show a relatively high agreement with less than a 0.6% difference. At the transition into the air plug, Attila over estimates the dose compared to MC for the first 0.5 cm. After which, Attila continues to steadily underestimate the dose deposited compared to MC by up to a maximum of -8.9%. Upon approaching the air-water interface, Attila's dose response compared to MC shows an increasing trend. Attila's lack of dose to points lying inside the air plug could show that Attila's calculations are underestimating low energy lateral scatter contribution when compared to MC results. Yet, Attila seems to show a very close approximation to MC dose at the initial water-air interface.

The Kerma$_{w,m}$ response at each point compared to the Kerma$_{m,m}$ results showed near unity. These equivalent dose results with the air material replaced by water proves the relationship shown by the mass-energy absorption coefficients from Figure 26.

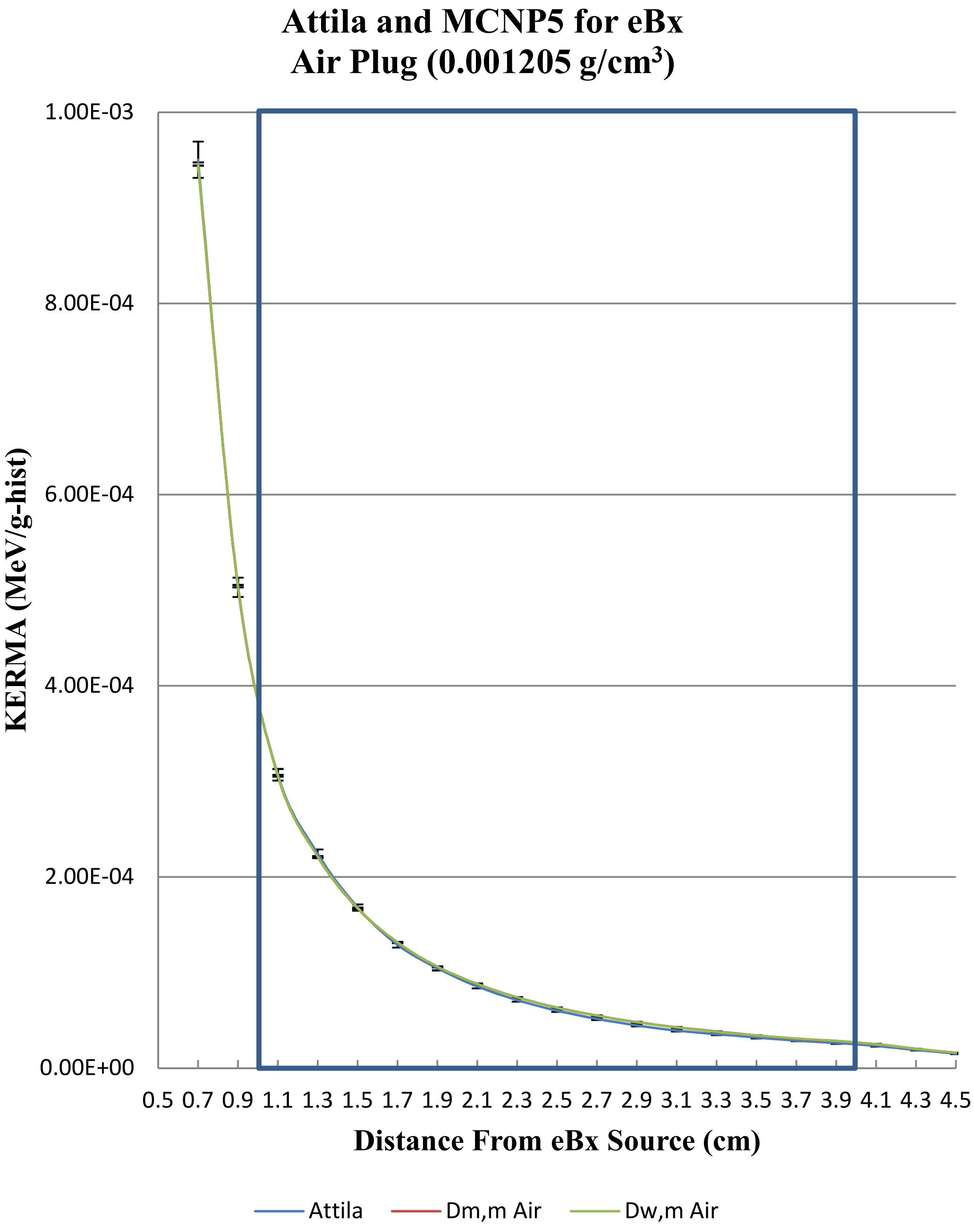

Figure 33. Attila and MCNP5 air plug comparison with low kV spectrum.

The fourth test the plug was given the material composition of lung with density of 0.3 g/cm^3. The MC results were calculated using 5x10^8 histories. The results of the MC F6 and Attila outputs are graphed in Figure 33. The average difference of the MC and the Attila for the lung plug was 2.7% and a maximum difference inside the lung plug of 9.0% and a minimum of -1.9%. The kerma$_{m,m}$ results from Attila show an almost equivalent response to MC dose leading up to the water-lung interface. At the transition into the lung plug, Attila again over estimates the dose compared to MC for the first 0.5 cm. After which, Attila continues to steadily underestimate the dose deposited compared to MC by up to a maximum of -5.8%. Upon approaching the exiting lung-water interface, Attila dose response compared to MC shows an increasing trend back toward unity. Attila's lack of dose to points lying inside the lung plug could again show that Attila's calculations are underestimating low energy lateral scatter contribution as was shown with the air plug. While the lack of scatter contribution could be a significant factor, another contributing factor could be if the Attila space discretization was not small enough.

Outside of the lung plug, the Kerma$_{w,m}$ and Kerma$_{m,m}$ results showed almost unity. Unlike the air plug, the Kerma$_{w.m}$ underestimates the dose within the lung plug as compared to Kerma$_{m,m}$. This underestimation of dose was unexpected as the mass-energy absorption coefficients for lung ratio to water are relatively close to one as seen from Figure 26. In fact, it was expected that the results from the dose to water point would exceed the dose to the lung point due to the increased density of the water.

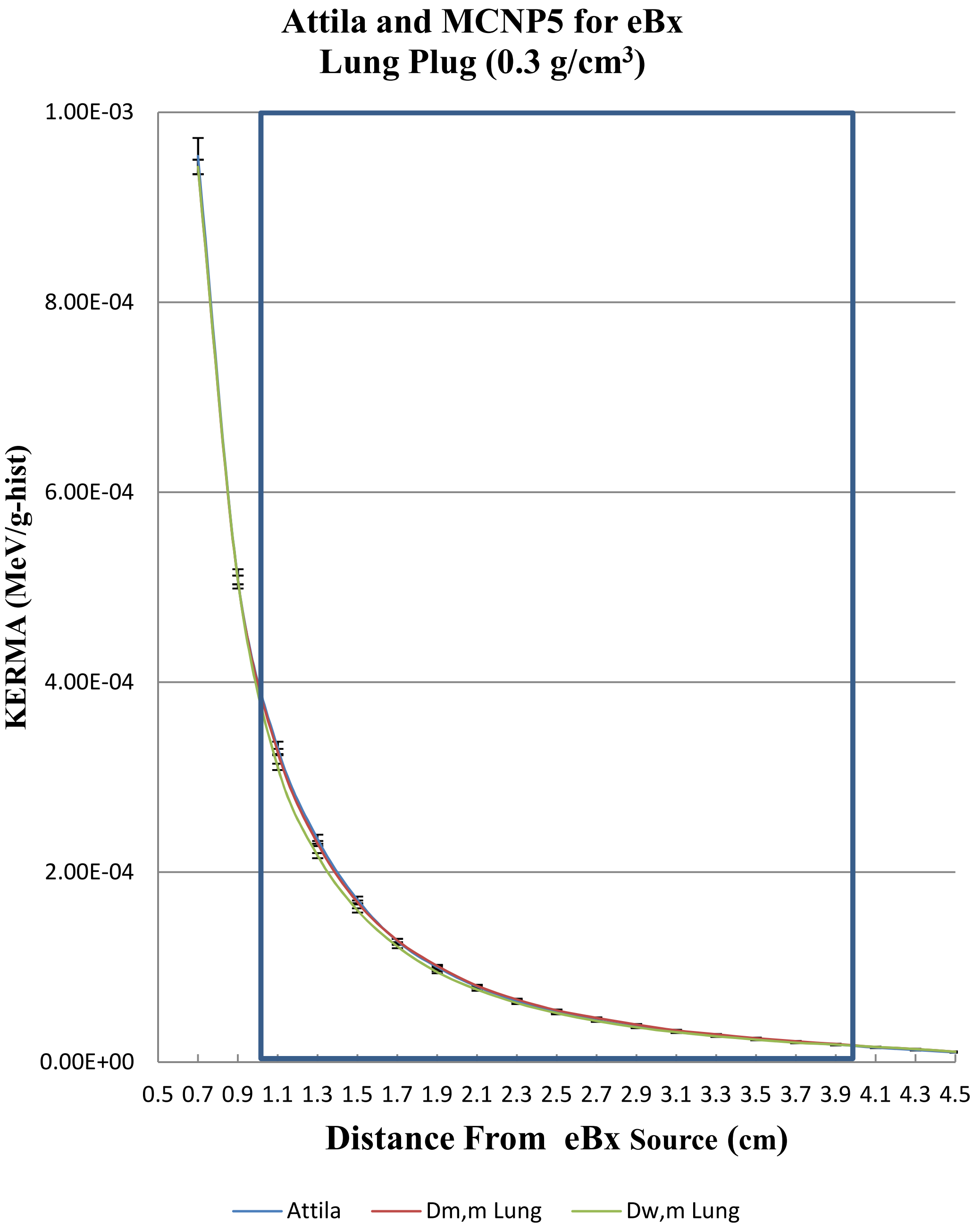

Figure 34. Attila and MCN5 lung plug comparison with low kV spectrum.

In review of Figure 35, the water, lung and air showed the best correlation between MC and Attila. As can be seen, Attila overestimates the dose to bone for all points. A contributing factor that could cause differences to increase as distances increase from the source was the dramatically small number of reactions that occur from using such a low energy spectrum. This could be seen as an increased noise to signal ratio and cause MC and/or Attila's results to differ greatly. This noise can be seen at the 3.7 cm to 4.1 cm points as the results sporadically jump back and forth instead of trending in one direction. The dose comparison between MC and Attila correlate well up to 2.5 cm from the point source, with the maximum deviations still within ±5%, except for the water-bone interface.

Attila's method to discretize space, energy, and angular scatter when calculating the dose could be showing a greater error when transporting such low energy photon spectrum. The error from spatial sampling was evident as initial Attila calculations were made with the mesh sampling too large on the original imported QAP. It is still possible that the mesh should be further reduced based upon the photon energy. The lower the photon energy spectrum perhaps an even finer mesh sampling size would be needed to give better resolution. As always, when increasing the mesh sampling density, the trade-off will be that the calculation times will increase.

The last point is the energy being investigated. Since the eBx spectrum is a maximum 50 kVp, the peak photon energy occurs around 16 keV. At this energy the photoelectric interaction dominates the photon absorption. For this research it was also assumed that all liberated electrons expend their energy exactly at the point of photoelectric interaction occurred. Depending upon the resolution of the mass-energy absorption data that Attila is utilizing at this low photon energy, it could be a major contributing error to Attila's results versus MC. Although, only the differences starting at up to 2.9 cm from the source and beyond begin to jump dramatically. The Attila and MC dose differences for the uniform water plug remained below 2.8%, with the average result being almost no change. At least for a uniform scenario, Attila's estimations were able to accurately predict MC.

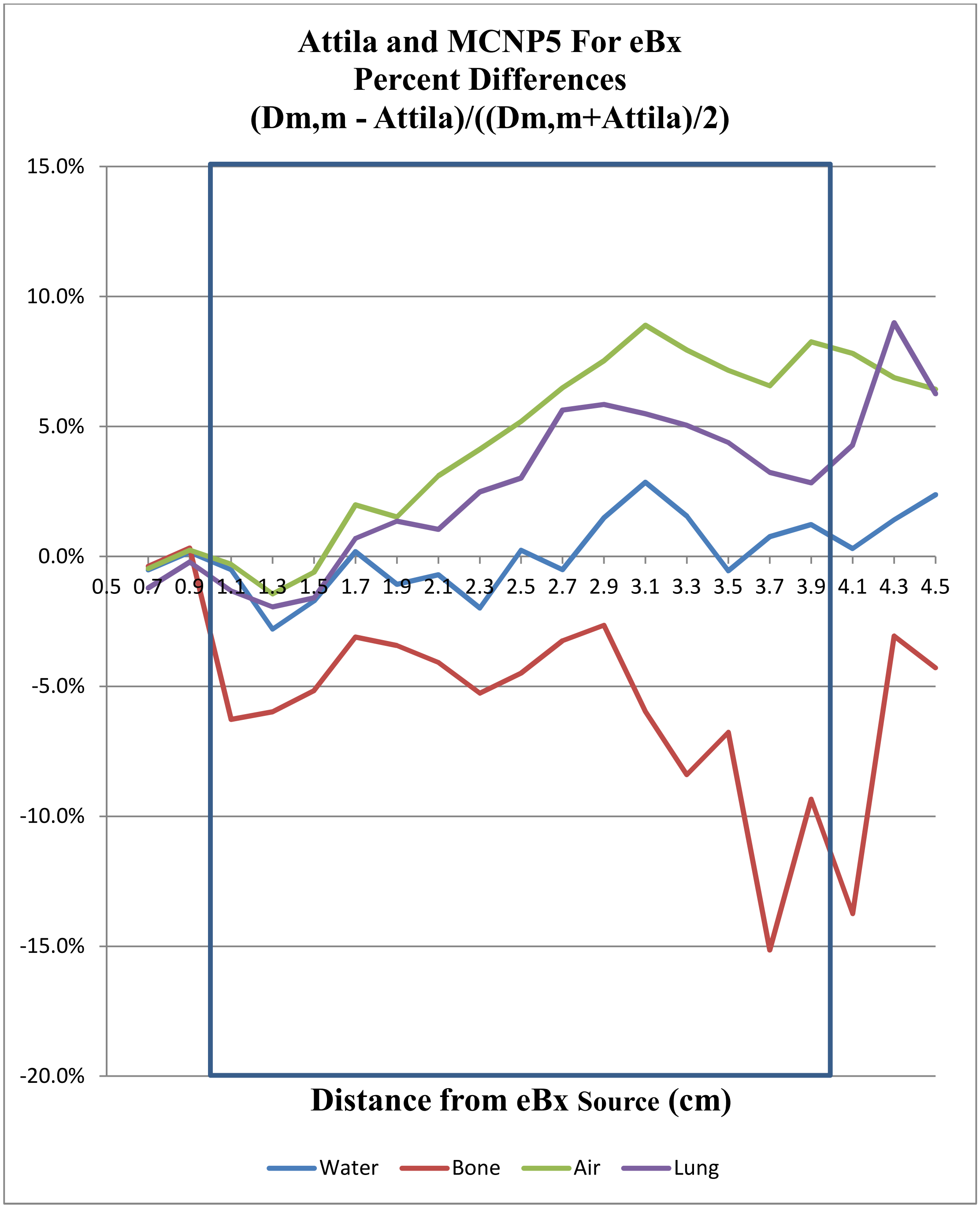

Figure 35. Attila and MC Percent Differences with low kV spectrum.

4.3. Patients with Acuros™ BV

In this research section, a large cohort of two hundred patient's statistics were reviewed. These patients already received the prescribed treatment dose of 340 cGy/fx for 10 fractions to a total of 3400 cGy at 1 cm from the cavity edge for SAVI or balloon edge, for the cases of Contura and MammoSite. Each patient plan was originally calculated using the TG43 formalism, as is customary at this clinic. Each patient's plan was then recalculated using Acuros. When recalculating, the same dwell positions and dwell times were used. Therefore, the new dose distributions would now incorporate any patient specific heterogeneities. Instead of painting in large patient areas and assigning macro material densities as was shown by White (White, et al., 2014), each case's individual patient voxel information was left untouched. By using the original voxel information, this would recreate a more realistic use of Acuros as can be expected within a clinical environment. Relevant clinical statistics were then collected for review.

A primary question that is asked by physicians when new calculation methods become available is, what is the difference in dose from the legacy algorithm to the new algorithm? The physician is interested in whether overall dose distributions will change remarkably that cause a prescription dose modification. A classic example was TG43 prescription adjustment by up to 17% for low kV source implants such as ^{125}I prostate seed implants.

Another important question asked by physicians, are there any expected dose changes to sensitive structures. An example of significant changes due to the newer algorithms could be the dramatic dose increase for low eBx when encountering a tissue-bone interface. The following tables have been created to answer some of these questions.

In tables 9 and 10, the dose difference between TG43 and Acuros are shown for the first 2mm of skin edge, maximum rib dose, $V_{100\%PD}$, $V_{95\%PD}$, and $V_{90\%PD}$. The $V_{100\%PD}$ is interpreted as what volume of the target is encompassed by 100% of the prescribed dose or in this case 3400 cGy. The largest changes were seen for the maximum rib dose for both MammoSite, Contura and SAVI. Unlike the eBx increase in rib dose, the ^{192}Ir dose difference shows that TG43 rib dose exceeded the Acuros rib dose, implying that the rib dose was less for all Acuros calculations. Unlike the eBx calculations where the $\mu_{en/\rho}$ bone to water was significantly greater than unity, the $\mu_{en/\rho}$ played very little roll at ^{192}Ir energies. Most likely, the reduced Acuros dose was attributable to the reduced dose at distance seen overall by the Acuros calculations primarily attributed to the less dense breast tissue.

Another point of interest is that the Contura and MammoSite plans show the larger decrease in dose volume coverage. This may be due to the water volume was redrawn and given a static uniform density of water, or 1 g/cm^3, which is denser than breast tissue.

The dose at a distance from the SAVI was expected to increase since the cavity is usually filled with air and would have seen a lack of attenuating material. As shown in Table 10, this was not the case. Instead the data may suggest that since SAVIs place their dwells so close to the surrounding PTV_Eval (1 cm margin) that each dwell contributes dose to the adjacent area and therefore uses smaller dwell times. If the dwells are contributing locally and have reduced dwell times, their contributions at a distance across the air filled cavity could be largely insignificant. The lack of fluid filled cavity would become inconsequential to overall dose homogeneity.

Table 9. Contura and MammoSite Patients Acuros vs. TG43

Points and Volumes of Interest from 166 patients
TG43 - Acuros

	Maximum Difference	Average Difference	Standard Deviation
Skin Dose	346.8 cGy	204 cGy	± 68 cGy
Rib Dose	384.2 cGy	136 cGy	± 68 cGy
Vol.$_{100\%PD}$	8.7%	5.6%	± 1.1%
Vol.$_{95\%PD}$	8.5%	4.9%	± 1.3%
Vol.$_{90\%PD}$	8.6%	3.8%	± 1.7%

Table 10. SAVI Patients Acuros vs. TG43

Points and Volumes of Interest from 34 patients
TG43-Acuros

	Maximum Difference	Average Difference	Standard Deviation
Skin Dose	265.2 cGy	110 cGy	± 105 cGy
Rib Dose	598.4 cGy	75 cGy	± 119 cGy
V100%	6.8%	2.2%	± 1.2%
V95%	6.0%	2.1%	± 1.2%
V90%	6.9%	2.1%	± 1.5%

One of the major limiting organ doses in breast brachytherapy is the dermis. RTOG 0413, B-39 defined the acceptable skin dose to be limited to 145% of the 3400 cGy prescribed dose, or 4930 cGy. The documented reactions of the dermis vary from least to greatest severity start at erythema, epilation, hyperpigmentation, dry desquamation, moist desquamation, and ulceration (Bray, et al., 2016).

In Tables 11 to 13, the data is shown for acute and chronic skin reactions. Part of this investigation expected to see skin reactions trend with increased skin doses. As can be seen from the Tables, all Contura, MammoSite, and SAVI averages, the Acuros dose was less than TG43. This dose decrease could be attributable to a large number of factors. One scenario could be the Contura and MammoSite balloon volumes are filled with uniform density of water while the breast tissue is less dense. This would actually show a reverse effect that less dose is deposited in less dense material for this energy range average of 380kV photon. Another observation is made at the skin and air interface. This interface was expected to see a significantly reduced dose at skin surface due to lack of backscatter from air density. A possible decrease in dose might have been as great as the Finite to Semi-infinite water phantom investigation. Looking back to Section 4.1, the last few calculation points in Table 6 showed ^{192}Ir contributed 12.8% less due to lack of surrounding scatter medium. For these two hundred cases, the average reduction in dose at skin-air interface was 6% decrease from TG43 to Acuros. It is possible that the patient's body acts as a semi-infinite phantom due to the extra scatter material in the cranial and caudal directions from the dwell positions. This increase in lateral dimensions may provide adequate lateral scatter to compensate for the lack of backscatter seen at the skin-air interface.

This skin-air interface reduction in dose is once again unclear as whether it's due to lack of backscatter or simply the reduction of dose deposited due to less dense breast tissue, or both.

The last two tables show the Acute and Chronic skin reactions average maximum skin doses for TG43 and Acuros. The observations showed that all maximum skin doses were different between the two calculations. In almost every scenario, the Acuros maximum skin dose was less than the TG43 by 6%. While this lowered dose was expected, the overall data did not show a maximum skin threshold where acute and chronic skin reactions would be a definitive result from treatment. The data showed that the smallest maximum dose to show measurable acute TG43 skin reactions from Contura, SAVI and MammoSite were 98%, 88% and 98% of prescribed dose, respectively. While the smallest maximum dose to cause measurable acute skin reactions for Acuros skin reactions from Contura, SAVI and MammoSite were 93%, 83% and 93% of prescribed dose, respectively. These low doses associated with observable acute skin reactions may be associated with personnel judgment when grading skin reactions, or some patients skin may react to even low doses.

Table 11. Two hundred patient results overview.

						TG43	Acuros
	#Patients				Min. Skin Dist. Avg.	Max Skin Dose Avg.	Max Skin Dose Avg.
	200	%		Patients	(mm)	%PD	%PD
Contura	157	79	Rt	78	4	130	123
			Lt	79	5	130	124
Savi	34	17	Rt	17	11	109	105
			Lt	17	10	117	114
MammoSite	9	5	Rt	4	18	85	80
			Lt	5	9	116	110

Table 12. Acute Skin Reactions are tabulated with TG43 and Acuros™ BV maximum skin dose.

Acute Reactions					TG43	Acuros
			% of Total Patients	Avg. Minimum Skin Dose	Avg. Max. Skin Dose	Avg. Max. Skin Dose
		#patients	%	(mm)	%Pres. Dose	%Pres. Dose
Contura	Rt	31	16	4	130	123
	Lt	20	10	4	128	122
SAVI	Rt	2	1	18	91	86
	Lt	3	2	14	108	102
MammoSite	Rt	2	1	15	103	98
	Lt	0				

Table 13. Chronic Skin Reactions are tabulated with TG43 and Acuros™ BV maximum skin dose.

Chronic Reactions					**TG43**	**Acuros**
			% of Total Patients	Avg. Minimum Skin Dose	Avg. Max. Skin Dose	Avg. Max. Skin Dose
		#patients	%	(mm)	%Pres. Dose	%Pres. Dose
Contura	Rt	23	12	5	126	119
	Lt	21	11	4	127	121
SAVI	Rt	2	1	19	84	80
	Lt	4	2	12	112	109
MammoSite	Rt	0				
	Lt	0				

5. Conclusions

5.1. Physical Measurements

The initial investigation was to aid the clinical medical physicist by fabricating a reproducibly measurable scenario that would utilize the Acuros capability to model the transport of photons especially when encountering inhomogeneous materials. Physical measurements were also taken using diode and Mosfet. Even with Acuros calculating significantly different dwell times due to the air, lung or bone plugs, the measured results showed good accuracy and precision. Following the recommendations of TG186, the DICOM images of this phantom could be uploaded to a community database for further tests.

Further investigations that could give more detailed information would be to modify the phantom to accommodate MOSFETs entered into various holes in the QAP. If these holes were also drilled into the plugs, this might allow confirmatory measurements of any MBDCAs dose distributions when encountering inhomogeneities.

5.2. Acuros^{TM} BV vs. MC

To further support the use of Acuros in clinical scenarios, the calculations at multiple points were then compared to results from a MC model of the QAP. Since the medical physics community has not completely adopted a reporting method, this investigation showed both $D_{w,m}$ and $D_{m,m}$.

The initial investigation utilizing a full-scatter phantom showed excellent agreement between this research source design and Acuros when applied to a semi-infinite phantom. As was shown in Table 5, the MC calculations with the tally points collected both as F6 and *F8 tracked very closely to TG43. This was not unexpected as MC has been used to generate some of the parameters for TG43. While the *F8 will be more exact for tallying photon and electron transport the number of histories was excessive to produce acceptable uncertainty. The results from this research show that F6 is a reasonable tally choice to lower the necessary history counts to produce low statistical uncertainties. Also, F6 appeared to be as accurate as *F8 since the continuous slowing down approximation for the ^{192}Ir liberated electrons is so low, it can be assumed that all energy absorption takes place at the point of photon energy transfer.

For each of the different material plugs (water, air, cortical bone and lung) the Acuros comparison to MC showed good accuracy and precision. For the bone tally results, the lack of significant differences between Acuros and $D_{w,m}$ shows that the average mass-energy coefficient for the ^{192}Ir energy spectrum must be primarily from Compton reactions and close to unity with water.

Future research would be to inspect the differences between Acuros applied to macro density material instead the CT provided voxel density. This might have brought the Acuros and MC results closer.

5.3. Attila® vs. MC

The use of Attila and it's versatile interactive program was vital when investigating the low energy emitting x-ray tube for Axxent Xoft. Attila's interface for importing any 3D created environment was very powerful. When Attila voxelizes the 3D volumes by applying a tetrahedral mesh to the problem, the result gives a visual description of the discretization of space.

The results from Attila when compared to MC for the Xoft spectrum pushed the optimizer to its lowest limits as most MC works disregard photon energies less than 10 keV and the Xoft spectrum average energy was approximately 15 keV. As can be seen from the F6 tally graphs for the differing material scenario, Attila's results were very accurate. This further supports the commissioning for this GBBS when encountering heterogeneities.

Further research could be performed to fabricate the Xoft miniature x-ray tube in 3D dimensions, import into Attila and transport the electrons to produce the bremsstrahlung radiation and correlate results to the actual Xoft spectrum. Another investigation would be to properly model the Xoft energy spectrum and the forward hemi-spherical photon distribution with Attila and apply this to 3D breast patient volumes to determine more relevant Xoft distributions at lung, bone and skin interfaces.

5.4. Application of Acuros on Actual Patients

The two hundred patient study was primarily performed to see what clinically relevant values would change and to what extreme. The investigation also reviewed post-radiation treatment tissue effects, and using Acuros, attempt to correlate acute or chronic tissue responses to a dose constraint.

Several key volumetric indicators that have been tabulated in previous research studies like RTOG 0413, were examined. They were the $V_{90\%PD}$, $V_{95\%PD}$, $V_{100\%PD}$, maximum skin dose and maximum bone dose. Surprisingly, in almost every recalculated patient case the Acuros doses were lower than TG43 at bone-tissue and skin-air interfaces for ^{192}Ir. While it was assumed that the skin-air interface would be less than TG43 due to the lack of backscatter, it was surprising to see the reduced dose $V_{100\%PD}$ and $V_{90\%PD}$. These reduced volume doses are likely to be caused by the fact that breast tissue is less dense than water.

The investigation of the air pocket that remains inside a SAVI cavity once fluid drains out also showed lowered doses than expected. The hypothesis that SAVI treatments are producing greater dose distributions at a distance from the SAVI device due to the lack of attenuating fluid being present inside the cavity was false. The results for all SAVI recalculations from TG43 converted to Acuros showed lowered volumetric dose coverage, similar to the MammoSite and Contura.

The normal tissue reaction and dose data was collected in the investigation. The information was graphed and sorted in an attempt to correlate acute or chronic skin toxicities with an average dose calculated by Acuros. There appeared to be no clear dose to the skin surface that would have predicted an erythemic threshold. In fact, due to the Acuros calculations showing reduced dose deposition at the dermis, it was surprising that some patients still showed acute and chronic tissue complications.

Further research using Acuros and investigating breast brachytherapy could be the effects that balloon contrast have on distance dose distributions. In the current research, all contrast filled balloons were volumetrically assigned material of water and density of 1.0 g/cm^3. There is no doubt that the balloon contrast is preferentially reducing the lower photon energies from transmitting outside the balloon volume. Therefore, it may prove beneficial to model this contrast composition and allow Acuros to determine if there is further reduction of dose than is already predicted. This may mean that the TG43 calculations when applied to SAVI devices actually displays a more relevant dose distribution than when applied to MammoSite or Contura devices. As for further research into normal skin toxicities, a more pro-active grading on normal tissue reactions immediately correlated to Acuros calculations may benefit the practitioner in determining the best radiation plan for each breast brachytherapy treatment.

6. Bibliography

Beaulieu, L. et al., 2012. Report of the Task Group 186 on model-based dose calculation methods in brachytherapy beyond the TG-43 formalism: Current status and recommendations for clinical implementation. *Medical Physics,* 39(10), pp. 6208-6236.

Bray, F. N., Simmons, B. J., Wolfson, A. H. & Nouri, K., 2016. Acute and Chronic Cutaneous Reactions to Ionizing Radiation Therapy. *Dermatologic Therapy,* Volume 6, pp. 185-206.

Cazeca, M. J., Medich, D. C. & Munro, J. J. I., 2010. Effects of breast-air and breast-lung interfaces on the dose rate at the planning target volume of a MammoSite catheter for Yb-169 and Ir-192 HDR sources. *Medical Physics,* 37(8), pp. 4038-4045.

Cheng, C., Mitra, R., Li, X. A. & Das, I. J., 2005. Dose perturbations due to contrast medium and air in MammosSite treatment: An experimental and Monte Carlo study. *Medical Physics,* 32(7), pp. 2279-2287.

Correa, C. et al., 2017. Accelerated Partial Breast Irradiation: Executive summary for the update of an ASTRO Eveidence-Based Consensus Statement. *Practical Radiation Oncology,* 7(2), pp. 73-79.

Cox, J. D., Stetz, J. & Pajak, T. F., 1995. Toxicity Criteria of the Radiation Therapy Oncology Group (RTOG) and the European Organizaiotn for Research and Treatment of Cancer (EORTC). *International Journal Radiation Oncology Biology Physics,* Volume 5, pp. 1341-1346.

Daskalov, G. M., Loffler, E. & Williamson, J. F., 1998. Monte Carlo-aided dosimetry of a new dose-rate brachytherapy source. *Medical Physics,* 25(11), pp. 2200-2208.

Gifford, K. A. et al., 2006. Comparison of a finite-element muligroup discrete-ordinates code with Monte Carlo for radiotherapy calculations. *Physics in Medicine and Biology,* Volume 51, pp. 2253-2265.

Gifford, K. A. et al., 2008. Optimization of deterministic transport parameters for the calculation of the dose distrubution around a high dose-rate 192Ir brachytherapy source. *Medical Physics,* 35(6), pp. 2279-2285.

Huang, Y. J. & Blough, M., 2010. Dosimetric effects of air pocket sizes in MammoSite treatment as accelerated partial breast irradiation for early breast cancer. *Journal of Applied Clinical Medical Physics,* 11(1), pp. 46-56.

Jayaraman, S. & Lanzla, L. H., 1983. An overview of errors in line source dosimetry for gamma-ray brachytherapy. *Medical Physics,* 10(6), pp. 871-875.

Kan, M. W., Yu, P. K. & Leung, L. H., 2013. A review on the Use of Grid-Based Boltzmann Equation Solvers for Dose Calculations in External Photon Beam Treatment Planning. *BioMed Research International,* pp. 1-10.

Karaiskos, P. et al., 1998. Monte Carlo and TLD dosimetry of an 192Ir high dose-rate brachytherapy source. *Medical Physics,* 25(10), pp. 1975-1984.

Kassas, B., Mourtada, F., Horton, J. L. & Lane, R. G., 2004. Contrast effects on dosimetry of a partial breast irradiation system. *Medical Physicc,* 31(7), pp. 1976-1979.

Keisch, M. et al., 2007. *AmericanBrachytherapy.org.* [Online]
Available at: https://www.americanbrachytherapy.org/guidelines/
[Accessed 1 May 2017].

Kirk, M. C. et al., 2004. Dose perturbation induced by radiographic contrast inside brachytherapy balloon applicators. *Medical Physics,* 31(5), pp. 1219-1224.

Landry, G. et al., 2010. Sensitivity of low energy brachytherapy Monte Carlo dose calculations to uncertainties in human tissue composition. *Medical Physics,* 37(10), pp. 5188-5198.

Landry, G. et al., 2011. The difference of scoring dose to water or tissues in Monte Carlo dose calculations for low energy brachytherapy photon sources. *Medical Physics,* 38(3), pp. 1526-1533.

Lee, C., 2014. Recent developments and best practice in brachytherapy treatment planning. *British Institute of Radiology,* 87(20140146), pp. 1-14.

Lorence, L., Morel, J. & Valdez, G., 1989. *Physics Guide to CEPXS: A Multigroup Coupled Electron-Photon Cross-Section Generating Code,* Albuquerque: Sandia National Laboratories.

Lymperopoulou, G. et al., 2006. A dosimetric comparison of 169Yb and 192Ir brachytherapy of the breast, accounting for the effect of finite patient dimensions and tissue inhomogeneities. *Medical Physics,* 33(12), pp. 4583-4589.

Mille, M. M. & Xu, X. G., 2010. Comparison of organ doses for patients undergoing balloon brachytherapy of the breast with HDR 192Ir or electronic sources using Monte Carlo simulations in a heterogeneous human phantom. *Medical Physics,* 37(2), pp. 662-671.

Molteni, R., 2011. *From CT Numbers to Hounsfield Units in Cone Beam Volumetric Imaging: the effect of artifacts.* Chicago, American Academy of Oral & Maxillofacial Radiology.

Nath, R. et al., 1995. *Dosimetry of Interstitial Brachytherapy Sources,* College Park: American Association of Physicist in Medicine.

Oh, S. et al., 2009. Measurements of dose discrepancies due to inhomogeneities and radiographic contrast in balloon catheter brachytherapy. *Medical Physics,* 36(9), pp. 3945-3964.

Oh, S. et al., 2009. Measurements of dose discrepancies due to inhomogeneities and radiographic contrast in balloon catheter brachytherapy. *Medical Physics,* 36(9), pp. 3945-3954.

Pantelis, E. et al., 2005. The Effect of Finite Patient Dimensions and Tissue Inhomogeneities on Dosimetry Planning of 192Ir HDR Breast Brachytherapy: A Monte Carlo Dose Verification Study. *International Journal Radiation Oncology Biology Physics,* 61(5), pp. 1596-1602.

Papagiannis, P. et al., 2002. Dosimetry comparison of 192Ir Sources. *Medical Physics,* 29(10), pp. 2239-2246.

Perez-Calatayud, J. et al., 2012. *Dose Calculation for Photon-Emitting Brachytherapy Sources with Average Energy Higher than 50 keV: Full Report of the AAPM and ESTRO,* College Park: American Association of Physicists in Medicine.

Pla, C., Pdgorsak, E. B. & El-Khatib, E., 1988. Calculation of dose profiles in homogeneous phantoms for irregular, partially attenuated, photon beams. *Medical Physics,* 15(4), pp. 511-516.

Qi, Z.-Y.et al., 2007. Verification of the plan dosimetry for high dose rate brachytherapy using metal-oxide-semiconductor field effect transistor detectors. *Medical Physics,* 34(6), pp. 2007-2013.

Richardson, S. L. & Pino, R., 2010. Dosimetric effects of an air cavity for the SAVI partial breast irradiation applicator. *Medical Physics,* 37(8), pp. 3919-3926.

Rivard, M. J., Coursey, B. M., DeWerd, L. A. & Hanson, W. F., 2004. Update of AAPM Task Group No. 43 Report: A revised AAPM protocol for brachytherapy dose calculations. *Medical Physics,* 31(3), pp. 633-674.

Rivard, M. J., Venselaar, J. L. & Beaulieu, L., 2009. The evolution of brachytherapy treatment planning. *Medical Physics,* 36(6), pp. 2136-2153.

Rivard, M. J., Venselaar, J. L. & Beaulieu, L., 2009. The evolution of brachytherapy treatment planning. *Medical Physics,* 36(6), pp. 2136-2153.

Shah, C. et al., 2013. The American Brachytherapy Society consensus statement for accelerated partial breast irradiaiton. *Brachtherapy,* pp. 267-277.

Skowronek, J., Wawrzyniak-Hojczyk, M. & Ambrochowicz, K., 2012. Brachytherapy in accelerated partial breast irradiation (APBI)-review of treament methods. *Journal of Contemporary Brachytherapy,* pp. 152-164.

Soubra, M., Cygler, J. & Mackay, G., 1994. Evaluation of a dual bias dual metal oxide-silicon semiconductor field effect transistor detector as radiation dosimeter. *Medical Physics,* 21(4), pp. 567-572.

Tanderup, K. et al., 2013. In vivo dosimetry in brachytherapy. *Medical Physics,* 40(7), pp. 1-15.

Varian Medical Systems, Inc, 2009. *BrachyVision-Acuros Algorithm Reference Guide,* Palo Alto: Varian Medical Systems, Inc.

Vassiliev, O. N. et al., 2010. Validation of a new grid-based Boltzmann equation solver for dose calculation in radiotherapy with photon beams. *Physics in Medicine and Biology,* Volume 55, pp. 581-598.

Veronesi, U., Cascinelli, N. & Mariani, L., 2002. Twenty-Year Follow-Up of a Randomized Study Comparing Breast-Conserving Surgery with Radical Mastectomy for Early Breast Cancer. *The New England Journal of Medicine,* pp. 1227-1232.

Wazer, D. E. et al., 2001. Clinically Evident Fat Necrosis in Women Treated with High-Dose-Rate Brachytherapy ALone for Early-Stage Breast Cancer. *International Journal Radiation Oncology Biology Physics,* 50(1), pp. 107-111.

White, S. A. et al., 2014. Comparison of TG-43 and TG-186 in breast irradiation using a low energy electronic brachytherapy source. *Medical Physics,* 41(6), pp. 1-12.

White, S. A. et al., 2014. Comparison of TG-43 and TG-186 in breast irradiation using a low energy electronic brachytherapy source. *Medical Physics,* 41(6), pp. 1-12.

Williamson, J. F. & Zuofeng, L., 1995. Monte Carlo aided dosimetry of the microselectron pulsed and high dose-rate 192Ir sources. *Medical Physics,* 22(6), pp. 809-819.

X-5 Monte Carlo Team, 2003. *MCNP - A General Monte Carlo N-Particle Transport Code, Version 5,* Los Alamos: Los Alamos National Laboratory.

Xoft Inc., 2009. *Axxent Controller Operator Manual-Model 110.* Sunnyvale, CA: Xoft Inc..

Zhang, Z., Parsai, E. I. & Feldmeier, J. J., 2007. Three-dimensional quantitative dose reduction analysis in MammoSite balloon by Monte Carlo calculations. *Journal of Applied Clinical Medical Physics,* 8(4), pp. 139-151.

Zourari, K. et al., 2010. Dosimetric accuracy of a deterministic radiation transport based 192Ir brachytherapy treatment planning system. Part 1: Single sources and bounded homogeneous geometries. *Medical Physics,* 37(2), pp. 649-661.

Appendix A: 192Ir MCNP Input Deck

```
Ir-192 Gamma Med Plus Brachytherapy source
c Beginning of Cell Cards
c
c Ir-192 source
1   2   -22.42   -12 22 -23   imp:p,e 1  $ inside cylinder with radius 0.03
c
c stainless steel capsule
2   1   -7.8   -10 11 21 -23 imp:p,e 1  $ radius of capsule; 0.035 to 0.045
3   1   -7.8   -10 20 -21 imp:p,e 1  $ distal cap of capsule
4   1   -7.8   -10 23 -24 imp:p,e 1  $ proximal cap of capsule
c air pocket distal end of source
5   5  -0.001205 -11 21 -22 imp:p,e 1 $ air pocket next to source
6   5  -0.001205 -11 12 22 -23 imp:p,e 1
c woven steel cable
7   4   -5.6   -10 24 -26 imp:p,e 1  $ woven steel cable with radius 0.045
c
c variable material cylindrical peg CURRENTLY WATER
8  3   -1.058    -27 116 118 120 122 124 126 128 130
              132 134 136 138 140 142 144 imp:p,e 1
c solid water material Acuros
9   3   -1.058   -26 27 112 114 146 148 150 #1 #4 #5 #6 #7 #8 #9 imp:p,e 1
c *******************
c air outside phantom
c *******************
10   5   -0.001205 -200 26 27 150 imp:p,e 1
c
c
c *******F6 Tally points*************
c Calc pts
14  3  -1.058  -112 imp:p,e 1
15  3  -1.058  -114 imp:p,e 1
17  3  -1.058  -116 imp:p,e 1
18  3  -1.058  -118 imp:p,e 1
19  3  -1.058  -120 imp:p,e 1
20  3  -1.058  -122 imp:p,e 1
21  3  -1.058  -124 imp:p,e 1
22  3  -1.058  -126 imp:p,e 1
23  3  -1.058  -128 imp:p,e 1
24  3  -1.058  -130 imp:p,e 1
25  3  -1.058  -132 imp:p,e 1
26  3  -1.058  -134 imp:p,e 1
27  3  -1.058  -136 imp:p,e 1
28  3  -1.058  -138 imp:p,e 1
29  3  -1.058  -140 imp:p,e 1
30  3  -1.058  -142 imp:p,e 1
31  3  -1.058  -144 imp:p,e 1
33  3  -1.058  -146 imp:p,e 1
34  3  -1.058  -148 imp:p,e 1
35  3  -1.058  -150 imp:p,e 1
c
c
c outside the problem
99   0    200      imp:p,e 0     $ outside of the problem
c
```

```
c End of Cell Cards

c Beginning of Surface Cards
c
c
c
10   cx   0.045     $ outside radius of steel capsule and steel cable
11   cx   0.035    $ inside radius of steel capsule
12   cx   0.030    $ max. radius of Ir-192
c
20   px  -0.242 $ plane at end of cap
21   px  -0.18  $ plane cutting for Ir-192 core cap
22   px  -0.17  $ plane cutting Ir-192 distal end
23   px   0.17  $ plane cutting Ir-192 proximal end
24   px   0.2
c
c
26   rpp  -2.5 2.5 -4.5 4.5 -4.5 4.5  $solid water rectangular volume
c
27   rcc -2.5 2.5 0  5 0 0  1.5 $ cylindrical plug
c
c
c *******F6 Tally points*************
112   sy  0.7 0.05
114   sy  0.9 0.05
116   sy  1.1 0.05
118   sy  1.3 0.05
120   sy  1.5 0.05
122   sy  1.7 0.05
124   sy  1.9 0.05
126   sy  2.1 0.05
128   sy  2.3 0.05
130   sy  2.5 0.05
132   sy  2.7 0.05
134   sy  2.9 0.05
136   sy  3.1 0.05
138   sy  3.3 0.05
140   sy  3.5 0.05
142   sy  3.7 0.05
144   sy  3.9 0.05
146   sy  4.1 0.05
148   sy  4.3 0.05
150   sy  4.5 0.05
c
c ****Boundary of Problem**************
200  so   50
c
c
c
c End of Surface Cards

c Beginning of Data Cards
mode P
c
nps 4e7
c
```

```
c Source Definition
c Ir192 Cylindrical volume source
sdef  par 2 pos=0 0 0 axs=1 0 0 rad=d1 ext=d2 erg=d3
si1 0.03
sp1 -21 1
si2 0.17
sp2 -21 0
c These energies (MeV) and probabilities are NNDC
c
si3 L 0.061486 0.063 0.065122 0.066831 0.071414 0.073363 0.075368 0.075749
     0.077831 0.11033 0.13639 0.17698 0.2013112 0.2057943 0.28027 0.2832668
     0.2959565 0.30845507 0.31650618 0.32909 0.3744852 0.4164688
     0.42051 0.46806885 0.4845751 0.48545 0.48906 0.588581
     0.59363 0.59941 0.60441105 0.61246215 0.70378 0.7658
     0.8845365 1.06149 1.08996 1.3785
c
sp3 D 0.0119 0.0202 0.0262 0.0444 0.0046 0.00161 0.00531 0.01021
     0.00364 0.000127 0.00199 0.000043 0.00471 0.0331 0.00008
     0.00266 0.2871 0.297 0.8286 0.000173 0.00727 0.0067 0.00069
     0.4784 0.0319 0.000047 0.00438 0.04522 0.00042 0.000039 0.08216
     0.0534 0.000053 0.000013 0.00292 0.000531 0.0000116 0.000014
c
c Tallies
c *****************************************************************
c F6 tallies for Energy Depositon (Mev/g) per source photon
c FM is Time (177.5s) X 1.602x10-6 ergs/Mev X 3.7x10 dis/s/Ci X 10Ci X 2.3 part/dis
c           X 1.13 (contained/apparent) X 1000 (g/kg)X 1e-7 (joule/erg) X (Gy*kg/joule)
c
c *****************************************************************
f6:p 14
FM6 27344
f16:p 15
FM16 27344
f36:p 17
FM36 27344
f46:p 18
FM46 27344
f56:p 19
FM56 27344
f66:p 20
FM66 27344
f76:p 21
FM76 27344
f86:p 22
FM86 27344
f96:p 23
FM96 27344
f106:p 24
FM106 27344
f116:p 25
FM116 27344
f126:p 26
FM126 27344
f136:p 27
FM136 27344
f146:p 28
```

```
FM146 27344
f156:p 29
FM156 27344
f166:p 30
FM166 27344
f176:p 31
FM176 27344
f196:p 33
FM196 27344
f206:p 34
FM206 27344
f216:p 35
FM216 27344
c
c Beginning of Material Data Cards
c AISI 316L Stainless Steel density of 7.8 g/cc
m1   6000  -0.0003
     7000  -0.001
     14000 -0.0075
     15000 -0.00045
     16000 -0.0003
     24000 -0.17
     25000 -0.02
     26000 -0.65545
     28000 -0.12
     42000 -0.025
c Ir-192 pure cylindrical source density of 22.42 g/cc
m2   077192 1
c Water density of 1.0 g/ccc
m3   1000 -0.111898
     8000 -0.888102
c
c AISI 304 Woven Steel Cable density of 5.6 g/cc
m4   6000  -0.0003
     7000  -0.001
     14000 -0.0075
     15000 -0.00045
     16000 -0.0003
     24000 -0.17
     25000 -0.02
     26000 -0.65545
     28000 -0.12
     42000 -0.025
c AIR (0.001205 g/cm3)
m5   1000 -0.00073
     6000 -0.00012
     7000 -0.75033
     8000 -0.23608
     18000 -0.01274
c ICRU-44 Cortical bone dens=1.92g/cc but using 1.69 from Gammex
m6   1000 -0.034
     6000 -0.155
     7000 -0.042
     8000 -0.435
     11000 -0.001
     12000 -0.002
```

```
     15000 -0.103
     16000 -0.003
     20000 -0.225
c ICRU-44 Lung Tissue density of 0.3 g/cc
m7   1000 -0.103
     6000 -0.105
     7000 -0.031
     8000 -0.749
     11000 -0.002
     15000 -0.002
     16000 -0.003
     17000 -0.003
     19000 -0.002
```

Appendix B: MCNP Xoft Spectrum Input Deck File

```
Xoft Brachytherapy source
c ***********************
c Beginning of Cell Cards
c ***********************
c
c variable material cylindrical peg  CURRENTLY Water
10 3 -1.0 -27 116 118 120 122 124 126 128 130 132
          134 136 138 140 142 144 imp:p,e 1
c
c solid water material
11  3  -1.0 -26 27 112 114 116 118 120 122 124 126 128 130 132 134
             136 138 140 142 144 146 148 150 imp:p,e 1
c
c air
13  5  -0.001205 -200 26 27 112 114 116 118 120 122 124 126 128 130 132 134
             136 138 140 142 144 146 148 150 imp:p,e 1
c
c Calc pts
14  3  -1.0  -112 imp:p,e 1   $calc at 0.7 cm
15  3  -1.0  -114 imp:p,e 1   $calc at 0.9 cm
17  3  -1.0  -116 imp:p,e 1   $calc at 1.1 cm
18  3  -1.0  -118 imp:p,e 1   $calc at 1.3 cm
19  3  -1.0  -120 imp:p,e 1   $calc at 1.5 cm
20  3  -1.0  -122 imp:p,e 1   $calc at 1.7 cm
21  3  -1.0  -124 imp:p,e 1   $calc at 1.9 cm
22  3  -1.0  -126 imp:p,e 1   $calc at 2.1 cm
23  3  -1.0  -128 imp:p,e 1   $calc at 2.3 cm
24  3  -1.0  -130 imp:p,e 1   $calc at 2.5 cm
25  3  -1.0  -132 imp:p,e 1   $calc at 2.7 cm
26  3  -1.0  -134 imp:p,e 1   $calc at 2.9 cm
27  3  -1.0  -136 imp:p,e 1   $calc at 3.1 cm
28  3  -1.0  -138 imp:p,e 1   $calc at 3.3 cm
29  3  -1.0  -140 imp:p,e 1   $calc at 3.5 cm
30  3  -1.0  -142 imp:p,e 1   $calc at 3.7 cm
31  3  -1.0  -144 imp:p,e 1   $calc at 3.9 cm
33  3  -1.0  -146 imp:p,e 1   $calc at 4.1 cm
34  3  -1.0  -148 imp:p,e 1   $calc at 4.3 cm
35  3  -1.0  -150 imp:p,e 1   $calc at 4.5 cm
c outside the problem
99   0    200      imp:p,e 0     $ outside of the problem
c
c End of Cell Cards

c Beginning of Surface Cards
c
c **********Solid Water Phantom***************
26   rpp  -4.5 4.5 -2.5 2.5 -4.5 4.5  $solid water rectangular volume
c **********Plug***********
27   rcc 2.5 -2.5 0  0 5 0  1.5 $ cylindrical plug
c
c ************Tally spheres****************
112   sx  0.7 0.05 $detector at different steps
114   sx  0.9 0.05 $detector at different steps
116   sx  1.1 0.05 $detector at different steps
```

```
118   sx  1.3 0.05 $detector at different steps
120   sx  1.5 0.05 $detector at different steps
122   sx  1.7 0.05 $detector at different steps
124   sx  1.9 0.05 $detector at different steps
126   sx  2.1 0.05 $detector at different steps
128   sx  2.3 0.05 $detector at different steps
130   sx  2.5 0.05 $detector at different steps
132   sx  2.7 0.05 $detector at different steps
134   sx  2.9 0.05 $detector at different steps
136   sx  3.1 0.05 $detector at different steps
138   sx  3.3 0.05 $detector at different steps
140   sx  3.5 0.05 $detector at different steps
142   sx  3.7 0.05 $detector at different steps
144   sx  3.9 0.05 $detector at different steps
146   sx  4.1 0.05 $detector at different steps
148   sx  4.3 0.05 $detector at different steps
150   sx  4.5 0.05 $detector at different steps
c
c *********Boundary**************
200   so   50         $ boundary of problem
c
c End of Surface Cards

c Beginning of Data Cards
mode P
c
nps 5e8
c
c ******************************
c Source Definition PolyEnergetic Xoft
c *******************************
sdef par 2 pos 0 0 0 erg=d1
SI1 A 0.006 0.0065 0.007 0.008 0.009 0.010 0.011 0.012 0.013 0.014 0.015 $ tabulated energies E1...
      0.016 0.017 0.018 0.019 0.020 0.021 0.022 0.023 0.024 0.025 0.026
      0.027 0.028 0.029 0.030 0.031 0.032 0.033 0.034 0.035 0.036 0.037
      0.038 0.039 0.040 0.041 0.042 0.043 0.044 0.045 0.046 0.047 0.048
      0.049 0.050
SP1   0.000 0.003 0.004 0.002 0.003 0.015 0.008 0.011 0.014 0.019 0.107 $ distribution values f(Ei)
      0.029 0.032 0.027 0.030 0.031 0.033 0.037 0.035 0.035 0.036 0.034
      0.035 0.034 0.033 0.031 0.030 0.030 0.028 0.026 0.025 0.024 0.021
      0.020 0.019 0.017 0.016 0.014 0.012 0.011 0.009 0.008 0.006 0.004
      0.002 0.00
c
c
c F6 tallies for Energy Deposition (MeV/g) per source photon
f6:p 14
f16:p 15
f36:p 17
f46:p 18
f56:p 19
f66:p 20
f76:p 21
f86:p 22
f96:p 23
f106:p 24
f116:p 25
```

```
f126:p 26
f136:p 27
f146:p 28
f156:p 29
f166:p 30
f176:p 31
f196:p 33
f206:p 34
f216:p 35
c
c Beginning of Material Data Cards
c
c Water density of 1.0 g/ccc
m3   1000 -0.111898
     8000 -0.888102
c
c AIR (0.001205 g/cm3)
m5   6000 -0.000124
     7000 -0.755268
     8000 -0.231781
     18000 -0.012827
c ICRU-44 Cortical bone density of 1.92g/cc but using 1.69 from Gammex
c m6   1000 -0.034 6000 -0.155 7000 -0.042 8000 -0.435  11000 -0.001
c      12000 -0.002 15000 -0.103 16000 -0.003 20000 -0.225
```

Appendix C: Two Hundred Patient Data

Number	TG43 MaxSkinDose	TG_MaxRibDose	TG_100%	TG_95%	TG_90%		Acu_MaxSkinDose	Acu_MaxRibDose	Acu_100%	Acu_95%	Acu_90%
1	135.2	123.1	84.7	90.9	95.5		131.4	120.2	79.1	86.2	92.1
2	119.9	42.4	82.1	88.4	93.2		115.3	39.2	77.7	84.3	89.8
3	133.7	23.8	77.7	84.8	90.8		129.5	21.7	72.2	80.6	87.3
4	123.4	55.1	75.7	83.7	90.8		115.7	52.8	69.9	76.8	84.7
5	136.5	7.1	72.4	80.4	87.2		129.1	0	66.5	74.6	81.5
6	118.5	155.4	72.7	79	85.2		113.2	151.5	66.4	73.4	80.2
7	111.4	104.7	77.4	82.7	87.6		106.3	100.7	73.4	79.1	84.5
8	162.7	133	83.4	89.9	96.1		154.5	127.6	77.5	84.3	90.9
9	144.3	136.2	78.4	84.7	90.7		136.1	133.2	72.7	79.2	85.3
10	116.8	48.7	79.7	85.8	90.7		110.1	47.2	74.1	81	86.7
11	135.1	110.2	76.3	83.5	90		128.2	107.1	70.2	77.2	84.5
12	131.2	61.7	85.2	92.3	97.4		125.8	59.1	78.5	86.6	94
13	135.5	165.5	84.4	90.8	96.1		129.4	160.1	78.5	85.5	92.3
14	143.4	98.5	91.3	95.1	97.1		140.5	94.5	86.5	92.5	95.9
15	148.4	153.7	85.9	90.6	94.6		141	146.6	79.2	85.2	90.9
16	129.5	111.9	84.4	91.9	97.8		124	105.8	78.1	85.1	93
17	144.2	25.8	86.8	94.1	98.7		138.8	23.6	79.2	87	94.2
18	123.9	133.7	87.6	93.4	96.9		118.4	128.2	83	89.2	94.2
19	113.5	78.1	81.4	89.5	95		107.6	75.9	76	83.7	90.4
20	136.7	32.6	87.1	93.6	97.8		130.5	30.6	81	88.8	94.6
21	124.5	38.8	94.5	97.9	99.7		114.3	36.2	90	94.6	98.2
22	118.5	133.7	73.8	82.2	90.4		111.7	129.6	67.6	75.4	84.1
23	114.6	120.9	93.3	98.1	99.9		111.1	117.5	88.7	94.9	98.8
24	120.5	100.1	92.7	97	99.2		115.4	94.6	87.6	93.6	97.6
25	112.1	131.7	93.4	98.2	100		105.7	128.5	87.1	94.4	98.9
26	121.1	77	86.4	94	98.5		114.9	73.1	80	88	95.2
27	159.2	150.5	65.8	72.8	80.2		154.4	145.1	60.8	67.5	74.5

28	153.7	101.6	84.8	89.7	93.8		145.2	99.4	80.2	85.5	90.4
29	119.7	136.1	80.3	86.9	92.3		115.2	131.7	74.3	81.6	88.4
30	140.7	101	71.6	79.2	86.3		135	94.6	64.5	72.2	79.8
31	133.7	72	67.4	75.2	82.8		129.6	69.9	63.8	71.6	79.5
32	145.2	135.8	78.2	85	90.8		137.3	130.5	71	78.6	85.7
33	122.5	29.8	81.5	89.3	94.6		115	27.6	73.4	81.9	89.9
34	127.9	65.8	74.2	82	89.7		122.2	62.3	68.7	76.2	83.9
35	124.2	49.9	82.8	90.8	96.4		117.5	47.7	77	85.5	93
36	159.1	63.8	65.8	74.4	83.8		151.5	61	59.5	68.1	77.1
37	132.1	161.5	87.2	92.5	96.7		122.3	157.1	80.2	86.3	91.5
38	132.2	23.8	80.6	88.1	93.8		123.2	22.1	75	82.9	89.6
39	129.2	159.6	65.5	71.6	78.3		123.1	154	60.8	66.8	73.2
40	142.7	26.8	76.4	85.6	90.7		136.9	24.9	72.8	80.2	86.7
41	129.1	46.2	79.4	87	93.9		122.4	44.4	73.8	81.3	89
42	104	88	62.2	67.1	72.2		101.5	85.3	60	64.8	69.8
43	118.5	95.5	36	43	51.8		114.3	92.2	28.9	36	44.2
44	154.9	79.4	74.9	81.2	86.5		152.9	76.7	70.6	76.9	82.6
45	143.4	136.5	84	90.8	95.7		134.4	131.6	78.5	85.4	91.6
46	143.6	173.2	79.6	85.4	91.2		137.9	171	73.5	79.6	85.5
47	147	139.8	81.2	86.2	90.8		140.5	135.8	76.2	81.7	86.9
48	144.3	102.8	81.2	87.9	94.2		138	99.7	75.5	82	88.8
49	136.1	35.7	69	76.3	83.7		129.9	33.6	64.2	71.2	78.7
50	135.4	118.9	80.3	86.2	92		128.3	113	74.8	81.2	87.2
51	138.1	158.7	75.7	81.6	87.4		130.4	154.1	70.4	76.5	82.9
52	139.8	132.9	91.2	93.5	95.2		133.3	128	87.8	91.4	93.8
53	127.7	103.9	75.4	83.8	91.3		121.1	100.4	68.2	77.2	85.8
54	138.4	72	89.4	94.4	98		131.4	68	84.3	90.2	95.3
55	121.2	110.6	76.3	83.9	91.2		114.9	106.1	71.8	79.2	86.8
56	150	73.8	52.4	58.7	64.8		145.4	70.4	48.5	54.1	60.3
57	134.8	64.3	74.8	82.3	89.5		127.1	59.6	67.8	75.3	82.8
58	137.3	123.7	87.5	92.6	96.9		129.5	117.6	81.8	87.8	93
59	142.8	18	74.8	82.8	90.9		134.4	16.3	68.8	76.9	85
60	44	63	93.7	98.9	100		42	62.3	90.3	97.9	100
61	124.3	40.1	86.7	93.2	97		117.6	37	80.6	88.4	94
62	143.6	176.9	76.7	83.2	89.9		135.9	165.9	70.8	77.3	83.8
63	123.8	110.2	89	95	98.6		116.6	106.8	83.3	90.2	95.9
64	135	120.4	67.4	74.6	81.8		128.4	116.1	62.5	69.3	76.4
65	119.3	145.3	73.8	80.5	86.5		112.3	140.8	69.1	76.3	82.7
66	121	65.1	80.3	87	93.3		114.6	62.3	74.8	81.8	88.4

67	121.9	140.6	69.3	75.8	82.4		113	135.6	63.4	70	76.7
68	142.9	175.1	80.6	86.7	91.5		136.1	169.9	75.2	81.7	87.6
69	135.2	147.3	77.3	85.1	92.2		131	142.6	69.8	77.4	85.3
70	129.7	103.6	89.7	95.9	99.3		123	99.2	83.2	90.4	96.2
71	154.8	192.4	96	98.8	100		147.1	187.1	90.3	95.3	98.6
72	129.7	53.1	88.7	94.6	98.4		123	49.6	82.7	89.5	95.3
73	130	92.7	88	93.3	97		125.1	88	83.8	89.4	94
74	142.9	177.2	90.8	96.4	99		135.6	168.9	85.5	91.9	96.9
75	158.4	138.5	50.9	58.1	65.9		153.8	131.4	43.5	50.2	57.3
76	134.5	104.5	94.5	98	100		126.9	100.5	89.5	94.7	98.1
77	153.7	110.7	92.5	96.8	99.5		146.2	106.2	87.1	92.9	97.4
78	144.5	165.1	90	94.5	97.6		138.9	158.5	85.6	90.7	95
79	122.7	130.8	78.8	86.5	93.3		116.1	126.4	72.4	80.3	87.8
80	130.9	80.3	79.1	87	94.4		124	79.1	73.1	81	88.8
81	125.6	188.1	70.9	77.4	83.4		120.7	185.2	66.8	72.8	78.8
82	141.4	135.4	76.7	83.8	90.6		135	128.5	70.7	77.7	85.2
83	147.8	70.5	86.6	93	97.2		138.2	66.5	80	87	93.2
84	137	117	91.8	95.9	98.8		129	112.7	86.9	91.7	95.9
85	131.7	28.8	82.4	88.3	93.4		122.3	27	77.2	83.5	89.2
86	124.9	85.2	82.6	90.1	96		116	80.5	74.9	83.3	90.8
87	131.7	103.2	77.6	84.7	90		131.3	98.5	72.3	78.7	84.9
88	132.4	66.8	88.6	95.9	99		125.7	63.8	81.8	90.3	96.4
89	120.3	98.9	88.9	93.5	97.1		113.9	95.3	84.6	89.8	94.3
90	134.3	95.2	80.9	88	93.6		126.5	92.7	74.8	82.3	89.1
91	136.7	67.9	96.4	99.2	100		131.8	64.4	91.5	97	99.3
92	120.4	74	74.2	82.8	90.9		115	69.5	67.3	75.8	84.5
93	121	72.7	77.4	86	93.8		115.8	69.4	70.5	79.6	88.4
94	122.9	104.6	93.6	97.7	100		115.2	103.2	89	94.3	98
95	137.1	142.4	80.6	87.7	94.5		131.1	138.8	75	82.2	89.4
96	139.1	177.6	78.1	85.2	91.8		131.5	166.3	70.5	78.2	85.5
97	144.6	116.2	91.4	95.6	98		138.2	110.9	87.2	92.3	96.1
98	144.4	46.5	92.4	97	100		138.3	44.4	88.8	94.4	98.5
99	132.9	23.8	88.6	94.3	97.7		126.1	21.8	83.1	89.9	94.7
100	128.8	155	90.7	96.4	98.6		120.4	149.6	85.2	92.1	97.1
101	131.5	56.9	91.6	96.8	99		126.8	53.8	87.8	93.9	97.8
102	122.9	132.3	93.8	97.8	99		115.8	127	87.7	94.7	98.2
103	125.6	182	92.7	98.4	99.6		119.9	177.7	85.6	94	98.5
104	119.8	201.7	85.3	91.5	96.3		113.2	194.5	77.8	85.3	91.8
105	146.4	30	95	99.4	100		140.6	28	89.6	96.8	100

106	122.1	98.5	80	87	93.7		118	95.6	75	82.9	90.1
107	149.5	100.1	93.8	97.2	99.1		143.5	96	90.1	95	97.7
108	142.9	193	87.9	92.6	96.5		137.2	186	83.2	88.5	93.1
109	115	101.4	87.2	91.8	95.5		107.3	97.8	82	88	92.6
110	130.7	115.7	86.1	92.9	97.7		124.3	110.7	80.8	87.6	93.7
111	128	257.1	88.5	93	95.8		123.1	251	82.7	88.5	93.2
112	121	99.5	76.4	83.2	89.3		115.7	95.6	71.6	78.7	85.3
113	121.1	125.4	92.7	97	99.4		114.9	121	86.7	93.2	97.3
114	138.7	163	84.4	91.4	96.5		132.6	158.4	75.7	83.9	91.3
115	112.8	113.5	95.5	98.9	100		107.4	108.9	89.8	96.2	99
116	117.8	120.1	81.2	87.5	93.1		113	116.4	75.8	83.3	89.7
117	134.9	94.9	83.9	90.2	95.5		127.1	90.9	77.4	84	90.4
118	138.5	22.1	89.35	95	98		132.6	19.7	84	90.3	95.3
119	113	160.1	80.5	86.8	92.1		105.6	154.6	75.5	82.2	88.1
120	114.1	46	84.2	90.2	95.3		109.8	43.9	79.2	86	92
121	130.8	78.5	84.6	93	98.5		124.4	75	76.3	85.6	94.1
122	140.2	99.6	89.1	92.8	95.7		135.1	96.3	86.3	90.4	93.9
123	137.8	158.4	83.9	89	94		131.5	148.9	78.9	84.1	89.1
124	138.5	155.1	91.3	96	99.1		130	152	86	91.7	96.1
125	124.1	101.6	80.6	89.5	96.3		115.4	98.2	71.9	81	89.9
126	120	126.3	91	96	99.2		113.8	121.7	86.9	93	97.6
127	147.5	117.7	98	100	100		137.4	112.6	90.9	97.8	100
128	149.9	158	85.8	91.5	96.3		140	151.1	80.3	86.4	91.9
129	120.6	175.2	86.5	92.8	97.1		113.3	172.4	80.3	87.2	93.5
130	138.7	198.3	91.3	96.9	99.4		131.2	194.4	86.1	92.7	97.6
131	122.4	140.2	85.2	91.6	96.4		114.6	137.7	79.7	86.4	92.3
132	115.1	94.6	78.1	84.6	91.2		108.9	91.2	72.7	79.7	86.6
133	121.2	138.6	85	91.6	97.1		115.9	135.5	78.8	86.4	92.8
134	122.8	150.5	90.6	95.4	97.7		117	147.1	84	91	95.6
135	107.9	135.3	96	98.6	99.8		101.5	129.7	91.6	96	98.5
136	116.6	132.8	80.4	87.4	93.6		108.7	128.5	73.7	81.5	88.7
137	107.1	130.3	92.5	98.5	100		100	127.7	85.4	93.6	98.7
138	114.2	112.9	79.7	85.4	90.8		107	113.4	73.8	80	85.8
139	144.9	136.5	96	98.3	100		136	132.2	92.7	96.1	98.4
140	118.5	39.3	81.8	88.6	94		113.5	37.9	76.5	84.1	90.7
141	116.4	99.1	90.8	94.6	97.2		108.4	99.1	86.5	91	94.7
142	121.4	106.6	72.8	81.5	89.7		114.5	103.8	66.5	74.6	83.1
143	121.4	113.6	78.4	86.9	94.3		115.7	106.2	72.7	81.1	89.6
144	119.2	38	68.6	75.7	82.7		114.1	36.1	64	70.8	78.3

145	108.3	145.7	81.2	86.6	91.5		103.4	141.8	74.7	80.8	86.7
146	102.6	75.4	73	81.6	90		97.1	72.8	67.3	75.6	84.3
147	119	115.4	80.6	86.6	92.2		113.4	108.4	74.5	80.8	87.1
148	126	21.4	92.6	96.9	99.1		121	20.2	87.8	94	97.4
149	111.8	87	83.7	90.8	96.1		106.5	83.5	77.3	84.9	91.6
150	148.8	99.4	96	98.9	100		141.5	95.9	91.1	96.5	99.1
151	119.3	46	86.3	91.4	95.5		113	43	81.5	87.4	92.2
152	141.5	32.5	86.4	92.7	96.9		134	29.2	80.6	87.7	93.5
153	130.2	33.7	86	92.1	95.9		122.9	31.7	80.1	87.2	92.7
154	139.2	91.2	96.7	99	100		133.2	85.9	95.6	98.1	99.4
155	74.5	118.2	94.5	97.2	98.7		71	122.8	94.2	96.7	98.4
156	103.1	24.5	96.6	98.8	99.5		98.3	23.1	94.7	97.6	99.1
157	139.2	122.6	92.4	95.8	97.7		139.5	119.7	90.9	94.5	97
158	132	34	90.8	95.2	97.3		130.4	31.6	88.6	93.5	96.7
159	122.4	214.1	91.2	94.2	96.5		120	213.4	89.2	92.3	95
160	112.9	111.5	89.5	93.3	96.1		109.7	108.2	87	91.1	94.8
161	73.4	138	91.3	94.2	96.4		73.2	132.4	89.5	92.8	95.4
162	75.4	115.2	86	91.1	95.2		73.4	115.8	84.2	90	94.3
163	98.9	119.4	89.5	92.4	94.8		95.9	116.6	87.4	91	93.7
164	130.6	99.4	81.4	87.1	91.3		125.9	97.6	80	85.6	90
165	113.1	101	78.9	84.8	89.7		110.8	99.9	77.5	83.8	89
166	97.3	96.6	72.4	78	83.3		94	93.9	69.1	74.9	80.2
167	80.7	150.1	57.3	62.6	68		76.3	150	54.6	60.3	65.8
168	87.8	29.8	87.1	91.8	95.3		83.4	28.3	83.2	88.8	93.1
169	110.8	62.2	83.9	90.1	94.7		106.1	60	81.9	87.7	92.8
170	107	87	84	89.6	93.5		100.1	84.4	82.4	88	92.2
171	144	190.4	86.8	92.8	97.7		141.8	190.2	84.6	87.8	90.8
172	94.2	86.6	79.8	86.3	92.3		88.8	84.1	75.7	82.4	88.9
173	102	81	83.6	88.3	92		99.5	78.4	81.1	86.1	90.3
174	103.8	122.9	80	85.3	89.8		96	117.6	73.2	79.3	84.5
175	70	104.2	78.7	84	89		65.7	101.9	76.3	81.8	87
176	130.6	49.7	85.7	87.2	86.6		128.2	47.3	85.1	86.8	88.3
177	98.3	106.6	79.7	84	87.8		95.6	103.6	76.6	81.6	85.8
178	163.4	89.6	80.8	84.5	87.7		172.9	89.2	80	83.2	86.7
179	93.6	89.8	77.3	83	87.9		92.2	89	76	81.6	86.5
180	164.6	22.6	76.7	80.5	84.1		164.4	20.4	74.6	78.7	82.4
181	110.3	101.6	75.1	79.3	82.8		108.5	104.2	72.7	77.2	81
182	131.9	159.1	69.7	73.7	78		128.7	156.5	67.6	71.4	75.7
183	109.9	146.9	66	71.3	76.6		102.6	150.7	63.5	68.4	73.9

184	130.5	350.4	66	69	71.8		127	332.8	64.9	67.7	70.6
185	97.5	125.5	85.4	91.9	96		92.7	120.7	79.7	86.5	93
186	97.5	125.5	85.1	91.7	96		92.7	120.7	79.4	86.9	93
187	136.4	106.3	78.4	83.4	88.7		127.5	100.9	73.3	79.5	84.8
188	134.3	23.8	65	72.4	80.6		127.1	22.3	60.3	67.7	75.4
189	111.9	115.1	87.5	94.3	98.3		105.3	111.5	80.4	88.7	94.8
190	131	120.4	81.5	87	92.1		122.6	115.6	76	82	87.8
191	69.3	30.1	86.6	94.5	98.8		65.2	27.7	82.1	90	97
192	103	55.4	79.4	87.8	94.1		96.9	52	72	81.4	89.4
193	125.8	115	76.1	83.6	88.8		120.6	112.4	70.4	78.3	85.4
194	149.4	146.1	66.7	71.9	76.5		141.9	144.3	64	68.5	73.6
195	134.1	123.6	79.2	83.7	87.7		126.7	119.5	76.9	80.8	85.2
196	63.3	111.4	94.5	98.5	99.8		58.7	107.2	89.8	96.3	99.4
197	60.7	93.6	90.2	96.6	99.7		57.3	87.9	84.1	92.2	98
198	127.3	81.5	67	75	83.7		122.8	77.7	61.3	69.8	78.5
199	108.2	155.1	86	91.7	96.1		104.2	147.8	81.1	87.5	93
200	125.5	87	82.2	88.6	93.7		119.5	84.4	77.5	84.1	89.6